UNIVERSITY OF CALIFORNIA, MERCED

X-ray Luminescence Computed Tomography for Small Animal Imaging

A dissertation submitted in partial satisfaction of the requirements for the degree
Doctor of Philosophy

in

Bioengineering

by

Michael Cam Lun

Committee in charge:

Professor Changqing Li, Chair
Professor Wei-Chun Chin
Professor Kara E. McCloskey
Professor Chih-Wen Ni

2020

The dissertation of Michael Cam Lun is approved, and it is acceptable in quality and form for publication on microfilm or electronically:

Professor Wei-Chun Chin

Professor Kara E. McCloskey

Professor Chih-Wen Ni

Professor Changqing Li, Chair

University of California, Merced

2020

This dissertation is dedicated to my parents.

TABLE OF CONTENTS

LIST OF SYMBOLS

∇	Gradient operator
$\mu_a(\lambda, \vec{r})$	Wavelength and position dependent absorption coefficient
$\mu'_s(\lambda, \vec{r})$	Wavelength and position dependent reduced scattering coefficient
$\vec{r}$	Position vector
$D(\lambda, \vec{r})$	Wavelength and position dependent diffusion coefficient
$\vec{n}$	Normal vector at boundary under consideration
C_{robin}	Robin boundary coefficient
Ω	Domain under consideration
$S_k(\vec{r})$	Source term representing the k-th x-ray beam illumination pattern
η	Light yield of contrast agent
$T_k(\vec{r})$	X-ray beam intensity distribution
T_0	Initial x-ray beam intensity
$x(\vec{r})$	Contrast agent concentration
$\mu_x(\vec{r})$	X-ray attenuation coefficient at position $\vec{r}$
L	Distance from x-ray's origin position to current position $\vec{r}$
$\vec{\mathrm{A}}_{n_d \times I \times J, m}$	System matrix
$\vec{b}_{n_d \times I \times J, 1}$	Measurements from XLCT scan
$\vec{\Gamma}_j$	Mask prior constraint vector
n_d	Number of detector nodes in finite element mesh
m	Number of finite element nodes
I	Number of angular projections in the XLCT scan
J	Number of linear scan steps for each angular projection in XLCT scan
L^{P}	The L^{P}-norm where ($\mathrm{P} \geq 0$)

LIST OF FIGURES

LIST OF TABLES

ACKNOWLEDGEMENTS

First, and foremost, I would like to thank my advisor, Dr. Changqing Li for allowing me the opportunity to work on this research project. He has been very supportive and encouraging throughout my entire graduate studies and his enthusiasm has kept me motivated. He also has always provided me with any resources and opportunities that I needed to succeed, which I really appreciate. I have learned a great deal from his broad knowledge and have developed many useful skills that will certainly be helpful for my future pursuits.

Next, I would like to acknowledge the help and support of my committee members, Dr. Wei-Chun Chin, Dr. Kara McCloskey, and Dr. Chih-Wen Ni who provided great advice and suggestions during our meetings and I highly appreciate the time and effort they have contributed to serving as my committee members.

Throughout my graduate studies, I have had the pleasure to meet and work with many great people. Dr. Dianwen Zhu developed the XLCT reconstruction algorithms and numerical simulations, which I use for most of my research. Dr. Wei Zhang, who I had the opportunity to work with very closely, taught me a great deal of knowledge about XLCT imaging and showed me how to perform experiments as well as build imaging systems. I also really appreciate all our discussions and enjoyed the meals you bought me after long days of research. Dr. Reheman Baikejiang and Dr. Yue Zhao who were my senior lab students when I joined the lab. They provided me lots of great advice and support for my work and helped my transition into graduate studies much easier. I am glad I was present to see all your successes and completion of the graduate program. I would like to also thank my current and former colleagues and biomedical imaging lab members as well for all their help and support throughout my journey: Yiping Guo, Ignacio Romero, Yile Fang, Kavita Kumar, Kun Zhang, Alex Nguyen, Kurtis Brent, Jarrod Cortez, and Steven Soe. The biomedical imaging lab has been a great cohort of people to work with and am grateful for all their support and hope I have also been helpful to them as well. I thoroughly enjoyed all the time we have spent together and couldn't have asked for a better group to work with.

I would also like to thank all my collaborators. Dr. Simon Cherry at UCD provided many critical tools for our lab, such as the microCT scanner, which helped our relatively new lab at the time get a great start at UC Merced. Dr. Zhongxing Zhou for his collaboration, which resulted in one of my published papers. I would also like to thank our collaborators from Dr. Jeffrey Anker's lab at Clemson University and Dr. Ge Wang's lab at RPI for our most recent collaborations regarding the FXLT scanner.

Many works included in this dissertation have been published in peer-reviewed journals. The permissions to use copyrighted materials have been granted by the Society

of Photo-Optical Instrumentation Engineers (SPIE), IOS Press, and the Optical Society of America (OSA).

My research has also been funded by various grants and funds. First, I would like to thank UC Merced for their start-up fund for Dr. Li to start our lab. My Bioengineering graduate program (and former Biological Engineering and Small-scale Technologies program) for providing my Summer fellowships as well as the some of the travel funds for my conferences. Our lab (Dr. Li as PI) has also received several grants from the National Institutes of Health (NIH) which supported my work significantly [R21 EB013828, R03 EB022305, and R01 EB026646].

Finally, I would like to thank my family for all their support. My parents provided me a tremendous amount of support and motivation not just throughout graduate school, but my entire life. I am truly thankful for you always being there for me, though I may not always show it. My sisters Jamie, Jennifer, and Kristeena who have always been there for me as well. I am also thankful for my brothers-in-law: Anthony, Gene, and especially Melanio Puzon, who helped tremendously with my application for graduate studies. I also would like to thank all my nieces and nephews: Dylan, Sophia, Nino, Melanio, and Avery. All your love has helped keep me going throughout this difficult but fulfilling journey.

CURRICULUM VITAE

Education

- University of California, Merced. Merced, CA, USA. (2015-2020).
  Ph.D. in Bioengineering.

- University of California, Merced. Merced, CA, USA. (2009-2014).
  B.Sc. in Bioengineering.

Publications

Peer-Reviewed

6. Yueming Zhang*, **Michael C. Lun***, Changqing Li, and Zhongxing Zhou, "Method for improving the spatial resolution of narrow x-ray beam-based x-ray luminescence computed tomography imaging," J. Biomed. Opt. **24** (8), 086002 (2019); DOI: 10.1117/1.JBO.24.8.086002. ***Equal Contribution Authors**

5. **Michael C. Lun** and Changqing Li, "Background luminescence in x-ray luminescence computed tomography," Appl. Opt. **58** (4), pp. 1084-1092 (2019); DOI: 10.1364/ao.58.001084.

4. Wei Zhang, **Michael Lun**, Alex Nguyen, and Changqing Li, "A focused x-ray beam based x-ray luminescence computed tomography," J. of Biomed. Opt., **22** (11), 116004 (2018); DOI: 10.1117/1.jbo.22.11.116004.

3. Wei Zhang, Dianwen Zhu, **Michael Lun**, and Changqing Li, "Collimated superfine x-ray beam based x-ray luminescence computed tomography," J. of X-ray Sci. and Tech., **25** (6), pp. 945-957 (2017); DOI: 10.3233/XST-17265.

2. **Michael C. Lun**, Wei Zhang, and Changqing Li, "Sensitivity study of x-ray luminescence computed tomography," Appl. Opt., **56** (11), pp. 3010-3019 (2017); DOI: 10.1364/ao.56.003010.

1. Wei Zhang, Dianwen Zhu, **Michael Lun**, and Changqing Li, "Multiple pinhole collimator based X-ray luminescence computed tomography," Biomed. Opt. Expr. **7** (7), pp. 2506-2523 (2016); DOI: 10.1364/boe.7.002506.

Conference Proceedings

8. **Michael C. Lun** and Changqing Li, "High-resolution focused x-ray luminescence computed tomography," Proc. of SPIE 11317, Medical Imaging 2020: Biomedical

Applications in Molecular, Structural, and Functional Imaging; 113171D (2020) https://doi.org/10.1117/12.2544493.

7. **Michael C. Lun**, Wenxiang Cong, Md Arifuzzaman, Meenakshi Ranasinghe, Sriparna Bhattacharya, Jeffrey Anker, Ge Wang, Changqing Li, "X-ray luminescence imaging for small animals," Proc. of SPIE Proc. of SPIE 11224, Optics and Ionizing Radiation; 112240F (2020) https://doi.org/10.1117/12.2544601.

6. **Michael C. Lun** and Changqing Li, "Focused x-ray luminescence computed tomography," Proc. of SPIE 11113, Developments in X-ray Technology XII (2019); https://doi.org/10.1117/12.2532096.

5. **Michael C. Lun**, Wei Zhang, and Changqing Li, "Focused X-ray Luminescence Computed Tomography: experimental studies," Proc. of SPIE, Vol. 10871, Multimodal Biomedical Imaging XIV (2019); https://doi.org/10.1117/12.2506927.

4. **Michael C. Lun** and Changqing Li, "X-ray luminescence imaging of air, water, and tissue phantoms," Proc. of SPIE, Vol. 10487, Multimodal Biomedical Imaging XIII (2018); https://doi.org/10.1117/12.2287023.

3. Yiping Guo, Shi Sheng, Wei Zhang, **Michael Lun**, Shih-ming Tsai, Wei-chun Chin, Roy Hoglund, and Changqing Li, "High energy photons excited photodynamic cancer therapy in vitro," Proc. of SPIE, Vol. 10476, Optical Methods for Tumor Treatment and Detection: Mechanisms and Techniques in Photodynamic Therapy XXVII (2018); https://doi.org/10.1117/12.2291252.

2. **Michael C. Lun**, Wei Zhang, and Changqing Li, "X-ray luminescence computed tomography: a sensitivity study," Proc. of SPIE, Vol. 10137, Medical Imaging 2017: Biomedical Applications in Molecular, Structural, and Functional Imaging (2017); https://doi.org/10.1117/12.2254682.

1. Wei Zhang, **Michael Lun**, and Changqing Li, "Fiber based fast sparse sampling x-ray luminescence computed tomography," Proc. of SPIE, Vol. 10057, Multimodal Biomedical Imaging XI (2017); https://doi.org/10.1117/12.2252996.

Other selected work

1. **Michael C. Lun**, Wei Zhang, Yue Zhao, Jeffrey Anker, Wenxiang Cong, Ge Wang, and Changqing Li, "Development of a focused-X-ray luminescence tomography (FXLT) system," arXiv:1709.10186 [physics.med-ph] (Sept. 2017); https://arxiv.org/abs/1709.10186.

ABSTRACT

X-ray Luminescence Computed Tomography for Small Animal Imaging
Ph.D. Dissertation by **Michael Cam Lun**
University of California, Merced, 2020
Bioengineering
Ph.D. Advisor: **Professor Changqing Li**

High-resolution imaging modalities play a critical role for advancing biomedical sciences. Within the last decade, x-ray induced luminescence imaging has emerged and demonstrated great potentials for the molecular imaging of small animals by combining the high-spatial resolution of conventional x-ray imaging and the high measurement sensitivity of optical imaging. Specifically, x-ray luminescence computed tomography (XLCT) imaging has been introduced as a powerful new hybrid molecular imaging modality capable of the high-resolution imaging of deeply embedded x-ray excitable contrast agents in three-dimensions (3D). In principle for XLCT, x-ray photons are used to penetrate samples deeply, with negligible scattering, and contrast agents within the path of the excitation beam will absorb the x-ray energy and generate many optical photons, some of which pass through tissue and escape from the skin. Then by using highly sensitive optical detectors, the emitted optical photons can be measured for XLCT image reconstruction.

We have developed several prototype XLCT imaging scanners. First, we developed a collimated superfine x-ray beam based XLCT imaging and validated the system using both numerical simulations and physical experiments. We also systematically investigated the effects of the scanning x-ray beam size and number of angular projections on the spatial resolution of XLCT imaging. We found that the obtainable spatial resolution had a high dependency on the scanning x-ray beam size and that more angular projections improved the imaging quality. Particularly, the obtainable spatial resolution was found to be double the scanning x-ray beam diameter. To address the long data acquisition time with this method, we then proposed a multiple x-ray beam scanning strategy and were able to reduce the scan time dramatically. Then, due to the low x-ray photon utilization efficiency of the collimated based XLCT imaging system, we developed a focused x-ray beam based XLCT imaging system by using a polycapillary lens to focus the x-ray photons to a fine spot. In addition, we improved the measurement sensitivity by using an optical fiber and photomultiplier tube set-up instead of the conventional electron-multiplying charged coupled device (EMCCD) camera measurement set-up. This new set-up was validated systematically using both numerical simulations and phantom experiments. Due to the increased x-ray photon flux as well as higher-sensitivity set-up, the imaging time was further reduced. We have also measured the radiation dose in both the collimated and focused x-ray beam-based set-ups and found that the radiation dose was within the range of a typical CT scan.

To improve upon the spatial resolution of XLCT imaging, we then proposed a new scanning scheme for XLCT imaging which was accomplished by simply reducing the x-ray beam scanning step size. We found that the spatial resolution limit could be further improved and with a four-times reduction in the step size, we could improve the spatial resolution by 1.6 times. We then validated the high-resolution capabilities of our focused x-ray beam based XLCT imaging system by performing high-resolution phantom studies and demonstrated that cylindrical targets with edge-to-edge distances of 150 μm could be successfully imaged in our scanner.

We also have validated the feasibility of our imaging system for small animal imaging with a euthanized mouse study. We embedded a single capillary tube target filled with phosphor particles and were successfully able to reconstruct the distribution of the particles with high precision and accuracy. Finally, based on our previous work, we have proposed and are currently building the next generation XLCT scanner, dedicated for small animal molecular imaging. The proposed focused x-ray luminescence tomography (FXLT) scanner incorporates both a microCT and XLCT scanner in a single imaging system for easy registration of the anatomical and optical imaging. We first designed the scanner with computer-aided design (CAD), then the parts were purchased or fabricated according to our model. We also performed numerical simulations to verify the feasibility of the scanner. We anticipate the completed scanner will become a powerful tool for the molecular imaging community.

CHAPTER 1

INTRODUCTION TO BIOMEDICAL IMAGING AND X-RAY LUMINESCENCE COMPUTED TOMOGRAPHY (XLCT)

1.1. Introduction

As defined by the National Institutes of Health (NIH), biomedical imaging is the branch of medicine concerned with the development and use of imaging devices and techniques to obtain internal anatomical images and to provide a biochemical and physiological analysis of tissues and organs. Arguably, one of the greatest contributions to medical imaging is the discovery of x-rays by German physicist Wilhelm Roentgen in 1895 [1]. Since the discovery, the field of medical imaging has flourished with many new techniques and instruments. In this chapter, several popular imaging modalities will be discussed. Then, an overview of x-ray luminescence computed tomography (XLCT) will be given, starting from its inception in 2010 to the current state of research in 2020.

1.2. Overview of Biomedical Imaging Modalities

In this section, several popular imaging modalities will be discussed. First, starting with x-rays and some of their applications in medical imaging. Followed by other popular and well-known imaging modalities such as magnetic resonance imaging (MRI), nuclear imaging methods, and optical imaging methods. Finally, multiple-modality (multi-modality or multimodal) and hybrid imaging methods will be discussed.

Very shortly after Roentgen's discovery of x-rays, they were put into clinical and diagnostic use. X-rays are a form of electromagnetic (EM) radiation (like visible light) and can be treated as either an EM wave or as individual photons (quanta). For a majority of x-ray imaging methods, the premise is that as the x-rays travel and penetrate the body (or imaging specimen), there is modest scattering which allows for the precise localization of objects in tissue, and the resulting image contrast is formed due to the differential attenuations of the x-rays. The first implementation of x-rays for medical imaging led to the development of the field of radiography (two-dimensional (2D) projection imaging). Since then, several other x-ray imaging methods have been developed such as x-ray fluoroscopy, which allows for real-time visualization of x-ray projection images and x-ray angiography which utilizes x-ray contrast agents, typically iodine-based, for visualization of blood vessels [2]. To date, the most popular x-ray modality is x-ray computed tomography (CT), developed in 1971 by Sir Godfrey N. Hounsfield and Allan M. Cormack due to advancements in computer technology as well as application of the well-known Radon transform [3]. This revolutionary work would allow the two to receive the 1979

Nobel Prize in Physiology or Medicine for their contributions towards the development of CT. Currently, there are over 70,000,000 CT exams that are performed annually in the US alone [4]. Primary advantages of CT imaging are to provide high-spatial resolution images of the anatomy in three-dimensions (3D) and its use has been indispensable for both pre-clinical and clinical studies. However, since the mechanism of contrast is attenuation-based, which occurs in all tissue, there is a relatively low sensitivity for differentiating between different soft-tissues and for probing molecular features. In addition, typical x-ray contrast agents are highly concentrated aqueous solutions (commonly iodine-based) and thus cannot be employed for molecular imaging due to their high viscosity as well as limits on osmolality [5].

Magnetic resonance imaging (MRI) is another popular imaging modality which had its first clinical implementation in 1977, about 6 years after the first human CT images were published [6]. MRI has an advantage of being able to provide good soft-tissue contrast (higher than CT) and provide functional information by exploiting proton density, perfusion, diffusion, and biochemical contrasts which allows for co-registration of molecular information with anatomical information in a single imaging modality [7]. MRI can provide high-spatial resolution (less than 1 mm) and a good depth penetration (greater than 10 cm) but has the disadvantage of an inherently low sensitivity for the detection of targeted contrast agents compared with other imaging modalities. In addition, the negative contrast also limits the sensitivity of MRI [8]. Lastly, the MRI scanner is quite costly and is large.

Nuclear imaging methods include modalities such as positron emission tomography (PET) and single photon emission computed tomography (SPECT) and uses radioactive tracers (radiotracers) for non-invasive molecular imaging. Nuclear imaging methods have advantages of a high intrinsic sensitivity, good depth penetration, and a broad range of clinically available and tested molecular imaging agents [7]. PET typically utilizes tracers such as ^{18}fluorodeoxyglucose for sensing specific molecular processes and is a suitable imaging tool that can provide excellent sensitivity and moderate spatial resolution; however, it can only be used for imaging a single molecular target at a time, which is an issue for correlative studies involving multiple targets. In addition, imaging must occur within in a limited time window, following radiotracer synthesis which also must occur on site or at a nearby facility [9]. Also, the highest reported spatial resolution is about 0.7 mm, which is near the intrinsic limit of this modality [10]. SPECT is another popular nuclear imaging modality which is quite popular for heart and brain imaging and uses single photon emitters such as ^{99m}Technetium. Compared with PET, SPECT imaging suffers from a lower detection sensitivity (especially with the use of pinhole collimators) as well lower spatial and temporal resolution. For the pinhole SPECT, the best reported spatial resolution is in the 1-2 mm range [11]. Some advantages of SPECT are that the detectors (gamma cameras) are quite widely available and the radiotracers typically have a higher half-life ($T_{1/2}$) than those use in PET and are more easily produced.

Optical imaging methods are based on the detection of optical photons after their interaction within tissue and is widely used for functional or molecular imaging. Some popular optical imaging methods that are currently used for pre-clinical imaging include

fluorescence imaging or bioluminescence imaging. Fluorescence imaging is very attractive in the interventional setting, as the images can be acquired in real-time with a compact imaging system. In addition, for superficial targets, the spatial resolution can be quite good [7, 9]. For targets or structures located deeper than 2 mm however, the spatial resolution becomes degraded due to the scattering of the fluorescent optical photons and gets worse with imaging depth which is true of most optical imaging methods. This effect can be mitigated by utilizing near-infrared (NIR) photons (650-1000 nm) due to the increased tissue penetrating abilities of photons in this range which can allow for imaging of up to 10 cm [12]. There is also the problem of tissue autofluorescence which can further degrade the spatial resolution of fluorescence imaging and add a background signal that will limit the sensitivity [7, 9].

Recently, multi-modality (multimodal) imaging has become increasingly popular and utilized for biomedical research due to the capability of integrating lower resolution molecular information with higher resolution anatomical details from modalities such as CT [7]. Examples of some popular multimodal imaging techniques are PET/CT and SPECT/CT. Another form of multimodal imaging are hybrid imaging methods in which multiple modalities interact with each other to produce images that cannot be produces by any of the modalities alone. A typical example of a hybrid imaging modality is photoacoustic tomography (PAT) in which short-pulsed lasers are used to excite optical absorbers for generating ultrasonic signals and then optical functional parameters can be imaged at a resolution similar to conventional ultrasound imaging [13]. Another example of a hybrid imaging modality is the focus of this dissertation: x-ray luminescence computed tomography (XLCT) imaging to be discussed in detail in Section 1.3.

1.3. Overview of X-ray Luminescence Computed Tomography (XLCT)

In this section, the process of x-ray luminescence is first reviewed. Then applications of this process for imaging purposes, primarily for x-ray induced luminescence imaging is discussed with a focus on XLCT imaging. We then review works regarding the fabrication of x-ray excitable contrast agents for use in imaging. Lastly, the XLCT imaging model and image reconstruction algorithm is reviewed.

1.3.1. X-ray luminescence phenomena

The process of x-ray luminescence is a form of radioluminescence (also referred to as scintillation), where the x-ray photons' energy is utilized to stimulate the emission of visible optical photons from certain target materials. In short, for these types of materials, the incident x-ray transfers energy to the scintillating material, causing a shower of ionized low-energy electrons. For non-scintillating materials, the excess energy of the secondary electrons is normally just deposited as heat, but for scintillating materials, the secondary electrons migrate to the luminescent center (containing the cation) that creates a temporary excited electronic state which will eventually decay causing an emission of optical photons [14]. This process has been used for some time, as it is the basis for many types of radiation detectors such as the x-ray detector by use of bulk scintillating materials. In particular, for x-ray detectors, gadolinium oxysulfide (GOS) doped with either europium (Eu) or terbium

(Tb) is generally the material of choice due to its high-cross section for x-rays in the diagnostic x-ray energy levels as well as their excellent light yield [15]. Typically, the amount of light generated is dependent upon the concentration or amount of scintillating material, the absorbed radiation dose, and incident ionization energy.

1.3.2. X-ray luminescence computed tomography

The principle of x-ray luminescence for imaging purposes was first demonstrated as a 2D imaging modality by Chen *et al.* through *in vitro* thin tissue experiments [16, 17] using both Eu^{3+} and Tb doped GOS particles (GOS:Eu^{3+} and GOS:Tb). Then, by applications of optical tomography (such as in fluorescence molecular tomography (FMT) or bioluminescence optical tomography (BOT)), this idea was extended to be able to reconstruct the 3D distributions of the luminescent particles in a method called x-ray luminescence computed tomography or XLCT imaging. As a hybrid molecular imaging modality, XLCT has the potentials to combine the merits of both x-ray imaging (high spatial resolution) and optical imaging (high sensitivity). Figure 1.1 shows a simple depiction of a typical XLCT imaging system. In principle, XLCT exploits the fact that x-ray photons can penetrate tissue with very little scattering. During imaging, a sample is irradiated by a sequence of narrow x-ray beams, positioned at predefined (spatially selective) locations or patterns, while highly sensitive photodetectors like an electron multiplying charge-coupled device (EMCCD) camera or photomultiplier tube (PMT) can measure the x-ray luminescence signal on the object surface. At the same time, an x-ray detector can be used to detect the traversed x-ray beam to simultaneously obtain anatomical information which makes XLCT a dual-modality method. For conventional optical imaging, each photon carries very little information about its original emission location due to the strong scattering in optical tissue. However, for the case of XLCT imaging, the emission location is known to be along the narrow path of the x-ray beam regardless of where the photon is detected. Thus, the spatial information is obtained from a precise x-ray spatial encoding, as *a priori* information, which is fundamental for obtaining high resolution images, even at depth [9] and helps to overcome the optical scattering problem encountered for conventional deep tissue optical imaging. In addition, thousands of optical photons can be generated per absorbed high-energy x-ray [18], which makes this method highly sensitive. Another benefit of XLCT over other modalities, particularly fluorescence imaging, is that there is no tissue autofluorescence to limit the sensitivity.

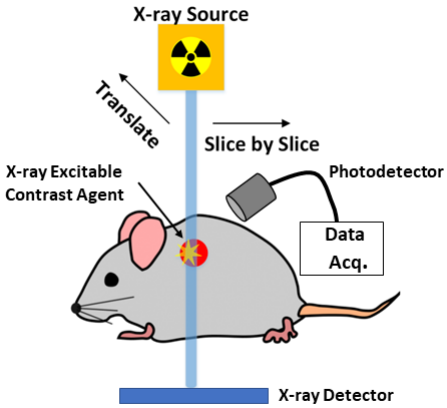

Figure 1.1. Simple depiction of a typical XLCT imaging system.

The pioneering work for XLCT imaging was performed in 2010 by Pratx *et al.* [18, 19] in which the feasibility of XLCT was demonstrated using a selective excitation-based imaging set-up. They demonstrated through simulations that XLCT imaging with a 1 mm narrow (pencil) x-ray beam, a spatial resolution of 1 mm was achievable. In addition, for superficial imaging, a subpicomolar molecular sensitivity was also demonstrated using 1 cGy of x-ray dose [19]. They also were the first to implement the selective-excitation based XLCT experimentally [18] and showed that the cross-sectional distributions of x-ray excitable nanoparticles (GOS:Eu^{3+}) could be imaged. Soon after, Li *et al.* used a collimated x-ray beam based XLCT imaging system and demonstrated with phantom experiments that the reconstructed target size varies by less than 10% for x-ray beam scanning depths up to 7.7 mm and also showed that two orthogonal projections were enough to reconstruct the distribution of embedded phosphor contrast agents [20]. Multiplexed imaging with XLCT was also demonstrated by Carpenter *et al.* where they successfully performed *in vivo* imaging of a mouse embedded with two different nanophosphors ($BaYF_2$:Eu and $BaYF_2$:Tb), demonstrating advantages of XLCT imaging for high-specificity molecular imaging [21].

The selective-excitation narrow x-ray beam based XLCT imaging (NB-XLCT) can obtain a high spatial resolution but has disadvantages of an inherently long measurement time, due to the small excitation region and the time required to scan across the entire sample for each angular projection (similar to the first-generation CT scanners). To help overcome the long scan times of the narrow x-ray beam approach, other x-ray beam geometries have been proposed and utilized for XLCT imaging. Chen *et al.* first proposed and demonstrated the feasibility of a conical x-ray beam based XLCT imaging system (CB-XLCT) [22]. This method can excite the entire sample volume at a single time, thus greatly reducing the measurement time but comes at a cost of a degraded spatial resolution, especially for deep targets, since the x-ray beam can no longer be used as structural guidance in the reconstruction algorithm. There have been some attempts to mitigate some of the *ill-posedness* of the CB-XLCT imaging reconstruction. Zhang *et al.* applied a Bayesian method and used a Gaussian Markov random field model and showed improved reconstruction accuracy compared with traditional methods [23]. Compressed sensing (CS)

was applied by Liu *et al.* who demonstrated a location error of less than 1.5 mm using single-view data for *in vivo* mice imaging [24]. Then, coded-aperture CS was utilized and applied by Tzoumas *et al.* and demonstrated good spatial resolution from few measurements compared with Tikhonov regularization [25]. Wavelet-based single view approach was also studied by Liu *et al.* and was shown to obtain a location error of about 0.8 mm [26].

Another possible x-ray beam geometry is the fan [27, 28] or sheet-beam based XLCT imaging (FB-XLCT) [29]. Cong *et al.* proposed and demonstrated the fan-beam x-ray geometry for XLCT imaging through numerical simulation studies and showed the method could have a fast measurement time, compared with the narrow-beam method, and does not suffer as much loss in spatial-resolution compared with the CB-XLCT [27]. Chen *et al.* proposed a reconstruction algorithm based on an x-ray distribution model and adaptively split Bregman method [28] for FB-XLCT, which was demonstrated experimentally to obtain a location error of about 1.1 mm. Then Quigley *et al.* proposed a selective-plane sheet-beam XLCT imaging method, using a slit collimator, which could resolve two targets separated by 1 cm up to a depth of 1.75 cm in a turbid media phantom [29]. Despite much efforts with both CB-XLCT and FB-XLCT, the selective excitation strategy of the narrow-beam approach still gives it the advantage in terms of obtainable spatial-resolution. The work in this dissertation will focus on improvements in NB-XLCT imaging which will be discussed in detail in the following chapters.

1.3.3. X-ray excitable contrast agents

Rare-earth nanophosphors are promising XLCT contrast agents for non-invasive bioimaging, such as for detecting tumors *in vivo.* For such applications, the nanophosphors should be small, colloidally stable, chemically functionable, and capable of generating bright radioluminescence signals with tissue penetrating red or NIR light. There are many microphosphors commercially available, such as GOS:Eu^{3+} (UKL63/UF-R1, Phosphor Technologies Ltd.), that have been primarily developed for lighting, display, and x-ray imaging. Recently, there has been much research in synthesizing and characterizing nanoscale x-ray excitable contrast agents such as GOS:Eu^{3+} or GOS:Tb [30-35] and other lanthanide-doped compounds. GOS:Eu^{3+} is a common imaging probe for XLCT imaging as it has been well studied and can emit bright and penetrating radioluminescence upon x-ray excitation. Figure 1.2 shows the x-ray luminescence spectra for GOS:Eu^{3+} from which we can see that the emitted light is primarily in the 600-750 nm range, which is excellent for deep tissue penetration. These nanophosphors can also be made more biocompatible and stable, for example with a poly(ethylene glycol) (PEG) coating [36] or a plasmonic gold shell [37] and could be functionalized to target antibody-based proteins like prostate-specific antigen [38] for example. Other bright and biocompatible nanophosphors have been developed as well such as $NaGdF_4$:Eu [37, 39] which was demonstrated to exhibit brighter radioluminescence than GOS:Eu^{3+} [37]. Through an energy-transfer sensitization process, PEG-$NaGd(WO_4)_2$:Eu was demonstrated to be even brighter than $NaGdF_4$:Eu and also exhibited a good CT and MRI contrast as well [40]. Another interesting contrast agent are Cu-Cy (copper cysteamine) complexes as they not only exhibit strong radioluminescent properties, but also the ability to generate singlet-oxygen which has great potentials for

both imaging and radiotherapy [41, 42]. Recently, Dai *et al.* demonstrated shortwave infrared (SWIR) XLCT imaging with Ho-doped $NaYbF_4$ core surrounded by a $NaYF_4$ shell which emits photons at approximately 1180 nm [43]. There are other imaging probes that can be used for XLCT besides the rare-earth nanophosphors. One example are biomolecule-directed metal clusters which have been developed for hard x-ray excited optical luminescence [44]. Quantum dots have also been studied as possible XLCT imaging probes, specifically CdTe quantum dots [45] which has been demonstrated to generate NIR emission upon x-ray excitation.

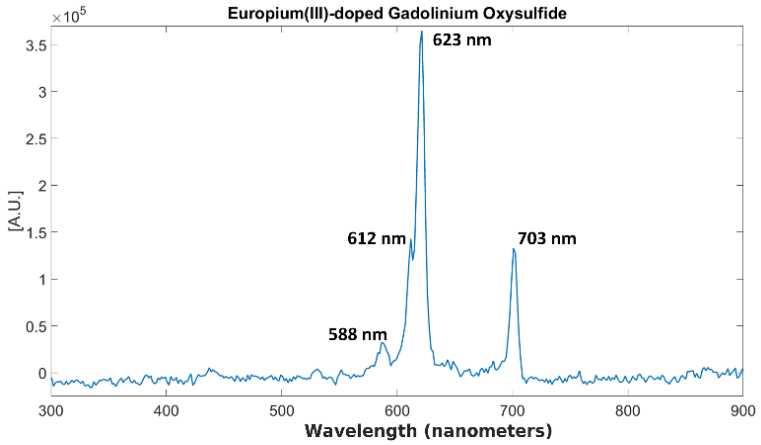

Figure 1.2. X-ray induced luminescence spectrum for GOS:Eu^{3+}.

1.3.4. Forward model and reconstruction algorithm of XLCT imaging

In XLCT, we use high energy x-ray photons to excite the x-ray excitable contrast agents which emit optical photons to be measured for XLCT reconstruction. Thus, we need to model the propagation of both the low energy optical photons and the high energy x-ray photons inside tissues. The propagation of the optical photons in turbid media such as tissues can be modeled by the diffusion equation in the continuous wave (CW) domain as in [46]:

$$\begin{cases} -\nabla \cdot \left(D(\lambda,\vec{r})\nabla\Phi(\vec{r})\right) + \mu_a(\lambda,\vec{r})\Phi\,(\vec{r}) = S_k(\vec{r}) \\ \quad \vec{n} \cdot \left(D(\lambda,\vec{r})\nabla\Phi\,(\vec{r})\right) + C_{robin}\Phi\,(\vec{r}) = 0 \end{cases} \quad \vec{r} \in \Omega \tag{1.1}$$

where $\mu_a(\lambda,\vec{r})$ is the wavelength (λ) dependent absorption coefficient at the position vector $\vec{r}$, $D(\lambda,\vec{r}) = [3\left(\mu'_s(\lambda,\vec{r}) + \mu_a(\lambda,\vec{r})\right)]^{-1}$ is the wavelength dependent diffusion coefficient, $\mu'_s(\lambda,\vec{r})$ is the reduced scattering coefficient, $\Phi\,(\vec{r})$ is the photon fluence at $\vec{r}$, $\vec{n}$ is the normal vector on the boundary under consideration, C_{robin} is the Robin boundary coefficient, and Ω is the domain under consideration.

$S_k(\vec{r})$ is a source term denoting the k-th x-ray beam illumination pattern and is described as:

$$S_k = \eta T_k(\vec{r}) x(\vec{r}) \tag{1.2}$$

where η is the light yield of the contrast agent, $T_k(\vec{r})$ is the x-ray beam intensity distribution, and $x(\vec{r})$ is the contrast agent concentration to be reconstructed.

As the x-ray beam scans along the object in a line, the x-ray beam's intensity distribution will follow the Beer-Lambert law in a uniform x-ray attenuating medium which can be expressed as:

$$T_k(\vec{r}) = T_0 \exp\left(-\mu_x(\vec{r}) \times L\right) \tag{1.3}$$

where T_0 is the initial x-ray beam intensity, $\mu_x(\vec{r})$ is the x-ray attenuation coefficient at $\vec{r}$, and L is the distance from the original x-ray source position to current position $\vec{r}$.

Based on the finite element method (FEM), the forward model of XLCT can be expressed as a simple linear equation:

$$\vec{\mathrm{A}}_{n_d \times I \times J, m} \vec{x}_{m,1} = \vec{b}_{n_d \times I \times J, 1} \tag{1.4}$$

where $\vec{b}_{n_d \times I \times J, 1}$ is our measurement, n_d is the number of detector nodes in the finite element mesh, I is the total number of angular projections, J is the number of linear scan steps for each angular projection, and m is the number of finite element nodes. The system matrix $\vec{\mathrm{A}}$ is expressed as:

$$\vec{\mathrm{A}}_{n_d \times I \times J, m} = \begin{bmatrix} \begin{bmatrix} \vec{\Phi}_1 \\ \vdots \\ \vec{\Phi}_{n_d} \end{bmatrix} \otimes \vec{\Gamma}_1 \otimes \vec{\mathrm{T}}_1 \\ \vdots \\ \begin{bmatrix} \vec{\Phi}_1 \\ \vdots \\ \vec{\Phi}_{n_d} \end{bmatrix} \otimes \vec{\Gamma}_{I \times J} \otimes \vec{\mathrm{T}}_{I \times J} \end{bmatrix} \tag{1.5}$$

where $\otimes$ is the elementwise product of Φ_i, $\vec{\Gamma}_j$, and $\vec{\mathrm{T}}_j$, where i ranges from 1 to n_d and j ranges from 1 to $I \times J$. $\left[\vec{\Phi}_1, \ldots, \vec{\Phi}_{n_d}\right]^T$ is the photon fluence vector obtained by solving Eq. 1.1. $\vec{\Gamma}_j$ is the mask prior constraint vector obtained from the known x-ray beam size and locations and is expressed as:

$$\vec{\Gamma}_j(s) = \begin{cases} 1 & \text{if node s is within the x-ray beam} \\ 0 & \text{otherwise} \end{cases} \tag{1.6}$$

The solution to Eq. 1.4 could be recovered by inverting the system matrix $\vec{\mathrm{A}}$, however the inverse problem suffers from *ill-posedness* due to the scattering of light in turbid media and limited number of measurements which becomes worse with depth. Therefore, we obtain the solution by minimizing the following regularized least-squared measurement misfit using a non-negativity constraint:

$$\vec{\mathrm{x}} = \mathrm{argmin}_{\mathrm{x} \geq 0} \mathcal{F}(\vec{\mathrm{x}}) \coloneqq \frac{1}{2} \left\| \vec{\mathrm{b}} - \vec{\mathrm{A}}\vec{\mathrm{x}} \right\|_2^2 + \alpha \|\vec{\mathrm{x}}\|_p^p \tag{1.7}$$

where α is a regularization parameter and $\|\vec{x}\|_p^p$ (p≥0) is the L^p norm. In the following works, we utilize the Majorization-Minimization (MM) algorithm which was previously developed for FMT but adapted to solve the XLCT inverse problem. Details of the MM algorithm can be found in [47-49]. The forward model and reconstruction algorithm were programmed with MATLAB (Mathworks) and ran on a calculation server with 128 GB memory and a 40-core CPU (each core frequency: 1200 MHz).

1.3.5. Quality evaluation metrics of XLCT images

In this section, several image quality evaluation metrics that are used in the following works are described.

Target size error (TSE): This criterion is defined as the target diameter error ratio between the reconstructed target size and true targets:

$$\mathrm{TSE} = \frac{|D_r - D_t|}{D_t} \times 100\% \tag{1.8}$$

where D_r and D_t are the diameters of the reconstructed and true targets, respectively. D_r is calculated using a cross-target line profile plot using the full width at ten percent maximum (FWTM).

Center-to-center distance error (CDE): For multiple targets, the CDE is defined as the distance error ratio between the reconstructed and true targets:

$$\mathrm{CDE} = \frac{|Dist_r - Dist_t|}{Dist_t} \times 100\% \tag{1.9}$$

where $Dist_r$ and $Dist_t$ is the center-to-center (CtCD) between the reconstructed targets and true targets respectively. $Dist_r$ is calculated from the target profile plot using the FWTM.

Dice similarity coefficient (DICE): DICE is used for quantifying the shape and location accuracy between the reconstructed and true target regions and is obtained as:

$$\mathrm{DICE} = \frac{2 \times |ROI_r \cap ROI_r|}{|ROI_r| + |ROI_t|} \times 100\% \tag{1.10}$$

where ROI_r is the reconstructed region of interest (ROI) defined as the pixels whose intensities are greater than 10% of the maximum of the normalized reconstructed intensity and ROI_t is the true ROI. The closer DICE is to 100%, the better.

Spatial profile index (SPI): SPI is used to evaluate the performance in resolving two adjacent targets and is defined as:

$$\mathrm{SPI} = \frac{{\rho^l}_{max} - {\rho^l}_{valley}}{{\rho^l}_{max} - {\rho^l}_{min}} \tag{1.11}$$

where ρ^l denotes the value of the profile along a given line in the reconstructed cross-section. ${\rho^l}_{max}$, ${\rho^l}_{valley}$, and ${\rho^l}_{min}$ are the maximal, valley, and minimum values between two peak values. The closer the SPI is to 1, the better the ability in resolving two adjacent targets.

Normalized mean square error (NMSE): NMSE is applied to evaluate the relative error between the reconstructed and true targets, defined as:

$$\mathrm{NMSE} = \frac{\|\hat{y}-y\|_2^2}{\|y\|_2^2} \tag{1.12}$$

where $\hat{y}$ and y are the reconstructed and actual nanophosphor distributions, respectively.

1.4. Dissertation Outline

In the following chapters, I detail advancements made towards NB-XLCT imaging we have made in my lab.

Chapter 2 discusses works made towards investigating and improving the spatial resolution in NB-XLCT. First, we developed and built a collimated x-ray beam based XLCT imaging system using a pinhole collimator to generate a superfine x-ray beam and performed both numerical simulations and phantom experiments to validate the system. We also performed simulation studies to investigate the effects of the x-ray beam size and number of angular projections on the spatial resolution in NB-XLCT imaging [50]. We then described and developed a multiple pinhole collimator based XLCT imaging system to decrease the long measurement time [51]. We also measured the radiation dose in this system. Lastly, we described and built a focused x-ray beam based XLCT imaging system and demonstrate the advantages of this set-up. We also showed advantages of using an optical fiber and PMT based measurement set-up over the typical electron-multiplying charged-coupled device (EMCCD) camera. The radiation dose was also measured in this new set-up and compared with the collimated x-ray beam-based system [52, 53].

In Chapter 3, the sensitivity of XLCT imaging was investigated for deep target imaging using various concentrations of GOS:Eu^{3+}. The sensitivity was also compared with a microCT scanner [54, 55]. We also investigated the presence of background x-ray luminescence signals that attributed background noise in XLCT imaging [56, 57].

In Chapter 4, we demonstrated a method for improving the obtainable spatial resolution for NB-XLCT imaging by reducing the linear step size, validated by numerical simulations and phantom experiments [58]. We then performed high-resolution XLCT imaging using phosphor targets of 200 μm diameters and less to demonstrate the high-resolution capabilities of the NB-XLCT imaging [59].

In Chapter 5, we validated the focused beam based XLCT imaging system for small-animal imaging by performing an *ex-vivo* mouse study [60]. We then proposed and are developing a small animal dedicated focused x-ray luminescence tomography (FXLT) imaging system [61, 62]. Numerical simulations are also performed to validate the feasibility and performance of the proposed FXLT imaging system.

Finally, Chapter 6 concludes the dissertation and discusses future work of NB-XLCT imaging.

CHAPTER 2

SPATIAL RESOLUTION IN XLCT IMAGING

2.1. Collimated Superfine X-ray Beam Based XLCT Imaging

As discussed in Section 1.3.2, the NB-XLCT imaging has advantages of a higher obtainable spatial resolution compared with the other x-ray beam geometries for XLCT imaging. In order to take advantage of the high spatial resolution capabilities, we continue to pursue our previous approach based on collimated x-ray pencil beams whose size and position are included as structural priors in the XLCT reconstruction [20, 46]. There are two approaches to generate a superfine x-ray beam. The first is by use of x-ray optics, where a conical x-ray beam is focused by an x-ray optics lens. This method has been used previously in x-ray fluorescence (XRF) analysis where mono- or poly-capillary lenses are uses to focus the beam into a fine focal spot. We will investigate this approach, applied to XLCT imaging, later in this chapter (Section 2.3). Another method to generate a fine x-ray beam is by collimation. If the collimator aperture is small, superfine x-ray beams can be generated. Pinhole collimators have been previously used in XRF microanalysis [63]. Advantages of this approach is that it is straightforward to implement at a low-cost. Disadvantages are the low-photon utilization efficiency since most of the x-ray photons are absorbed by the collimator, which may not be a problem in XLCT imaging if a high-flux x-ray beam or highly sensitive optical detectors are used.

The objective of this study is to investigate whether we can achieve high spatial resolution in deep turbid media. For this purpose, we propose to reduce the x-ray collimator's aperture diameter to 100 μm to generate superfine x-ray beams to scan deeply embedded phosphor targets. In this work, we have validated our method with both numerical simulations and phantom experiments.

2.1.1. Numerical simulation set-up

To investigate how the x-ray beam size affects the XLCT reconstruction, we have performed numerical simulations of XLCT with different collimated beam diameters to scan a cylindrical phantom embedded with 6 targets with different target diameters. A 10 mm long numerical cylindrical phantom with a 12.8 mm diameter was used to mimic a mouse-sized object. The numerical phantom had an absorption coefficient (μ_a) of 0.0072 mm^{-1} and a reduced scattering coefficient ($\mu`_s$) of 0.72 mm^{-1} at the wavelength of 703 nm, the longest wavelength peak in the emission spectrum of GOS:Eu^{3+}. The x-ray attenuation coefficient (μ_x) was set to 0.0214 mm^{-1}. We placed 6 targets inside the phantom as seen in Fig. 2.1. We simulated four different cases with target diameters of 1.0, 0.5, 0.2, and 0.1

mm. For all the numerical simulations, the edge-to-edge (EtE) distance is equal to the target diameter and the phosphor concentration was set to be 1.0 mg/mL. The background of the phantom contained no phosphor particles. For the simulation, we used a single x-ray beam to scan the phantom at a depth of 5 mm under the phantom top surface. The x-ray beam diameter was set to be 1.0, 0.5, 0.2, and 0.1 mm for different simulation cases. For all simulations we acquired measurements from 6 angular projections with an angular step size of 30º. To scan the entire phantom, for each angular projection, we used 13, 26, 64, and 128 linear scan steps for the beam diameters of 1.0, 0.5, 0.2, and 0.1 mm, respectively. Numerical measurements were generated with our forward model (Section 1.3.4). In the simulations, the beam size diameters remained static (beam size changes over distances are not considered), however the x-ray attenuation was included in the simulations. For simplicity, the x-ray initial intensity (T_0) in Eq. 1.3 was set to 1.

We also investigated how the number of angular projections affects the XLCT reconstruction. For this simulation, we used the same phantom geometry as seen in Fig. 2.1 with target diameters and EtE distances of 0.1 mm and simulated XLCT imaging using angular projections of 3, 6, 12, 24, and 36 with angular step sizes of 60, 30, 15, 7.5, and 5 degrees, respectively. In this study, we used a straight x-ray beam with a diameter of 0.1 mm, the same as the target diameter.

In all simulation cases, numerical measurements were generated from the forward model in which the phantom was discretized by a finite element mesh with 26,638 nodes, 153,053 tetrahedral elements, and 11,456 face elements. We also included 50% Gaussian noise in the simulations. Though XLCT is a 3D modality, we only reconstructed the scanned transverse section of the phantom. To minimize the effects of grid size on the XLCT image quality, the scanned transverse section was discretized with a 2D grid with a pixel size of 25 μm^2. We follow the method for including the actual beam size and position in the XLCT reconstruction algorithm as detailed in Section 1.3.4 where we applied the MM algorithm to minimize the L^1 regularized mismatch between the measured and modeled photon intensity and to update the XLCT images iteratively.

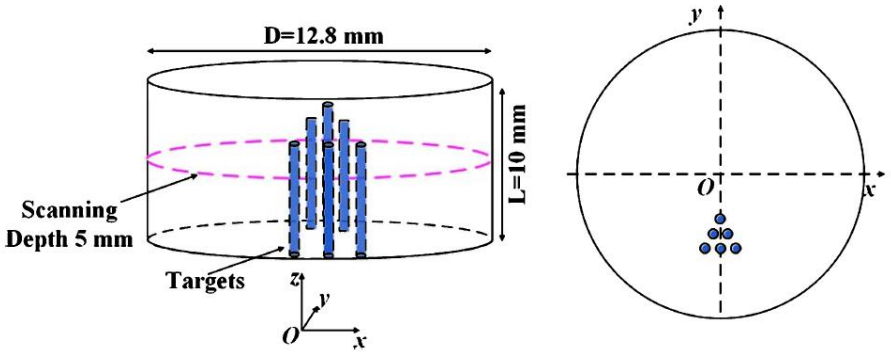

Figure 2.1. The phantom geometry for numerical simulations embedded with six targets. The target diameter and edge-to-edge distances are 1.0, 0.5, 0.2, and 0.1 mm for the different simulation cases.

2.1.2. Phantom experimental set-up

The XLCT system design is shown in Fig. 2.2(a). An x-ray tube (Neptune 5200, Oxford Instruments) generated x-ray photons with an energy up to 50 kVp and tube current of 2.0 mA. The generated x-ray photons were collimated by a 5.08 cm long and 25.4 mm diameter steel rod collimator with a central through-hole of 1.0 mm diameter. At the end of the steel rod, we embedded a 1 mm thick tungsten disk collimator with a 0.1 mm pinhole, which was used to generate the superfine x-ray beam. The collimator design is shown in Fig. 2.2(b). The phantom was placed on top of a motorized rotary stage (B4872TS-ZR, Velmex Inc.) that is mounted to a motorized linear stage (MB2509Q1J, Velmex Inc.). The object center was placed 10 mm away from the collimator. The position and size of the x-ray beam were measured by an x-ray detector (Shad-o-Box 1024, Rad-icon Imaging Corp.) with a detection area of 49.2 mm^2 with 1024 × 1024 pixels (48 μm^2 pixel size). The distance from the x-ray tube to detector was 150 mm. The emitted optical photons from the phantom top-surface were reflected by a flat mirror and acquired by a water cooled EMCCD camera (C9100-13, Hamamatsu) with a focus lens (50 mm, f/1.4 ZE planar T* manual focus, Zeiss). A 5 mm thick lead plate was placed between the x-ray tube and EMCCD camera to protect the camera from high-energy x-ray photons. As shown in Fig. 2.2(a), the imaging system was mounted on an optical table and placed inside of an x-ray shielding and light-tight cabinet. The system was controlled by a lab-made macro program written in C++ in Visual Studios development environment.

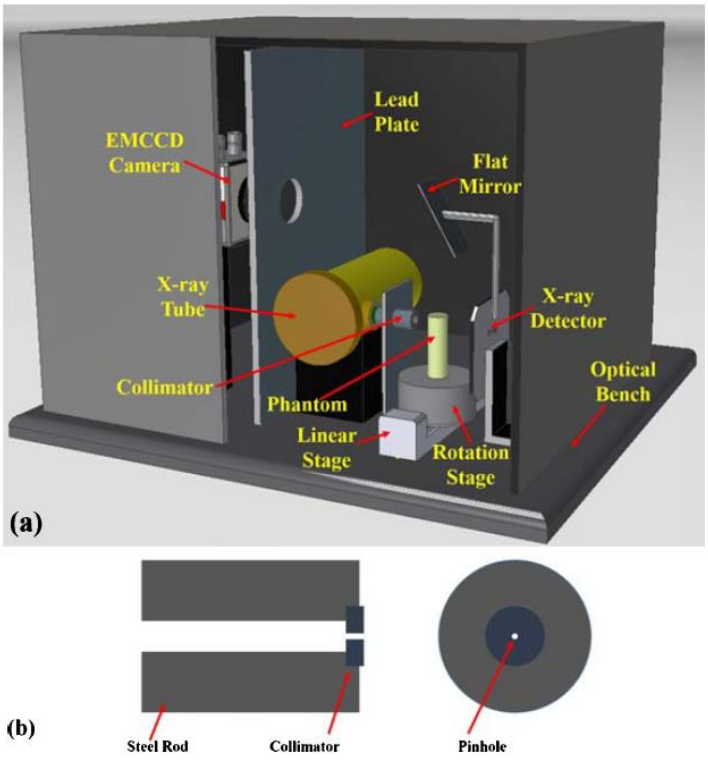

Figure 2.2. (a) 3D design of the superfine x-ray beam based XLCT imaging system; (b) Side and top views of the collimator design used in the phantom experiment.

We performed a phantom experiment with four targets to validate the feasibility of the high-resolution XLCT imaging system. We used a 40 mm long and 12.7 mm diameter turbid media phantom composed of 1% intralipid, 2% agar, and water. The target solution was the same as the background and was mixed with 10 mg/mL of GOS:Eu^{3+} (UKL63/UF-R1, Phosphor Techn. Ltd.). The target solution was then filled into capillary tubes and were embedded side by side as shown in Fig. 2.3. The capillary tubes had an inner diameter of 0.4 mm and wall thickness of 0.2 mm. The experimental system shown in Fig. 2.2(a) with an x-ray beam size of 0.1 mm was used to validate the feasibility of the system. The x-ray detector was used to determine the phantom boundary during the measurements by examining the x-ray beam intensity changes. During the experiment, the phantom was scanned with the x-ray beam at a depth of 5 mm below the top surface as seen in Fig. 2.3(c). To cover the entire scanning plane, we used 65 linear scan steps of 0.2 mm step size. During measurements, the EMCCD camera was cooled to a temperature of -92ºC and operated at the maximum electron multiplying gain (EM Gain) of 255 and analog gain of 5 and acquired measurements using an exposure time of 20s for each linear scan position. The x-ray tube was set to operate at 50 kV and 2.0 mA.

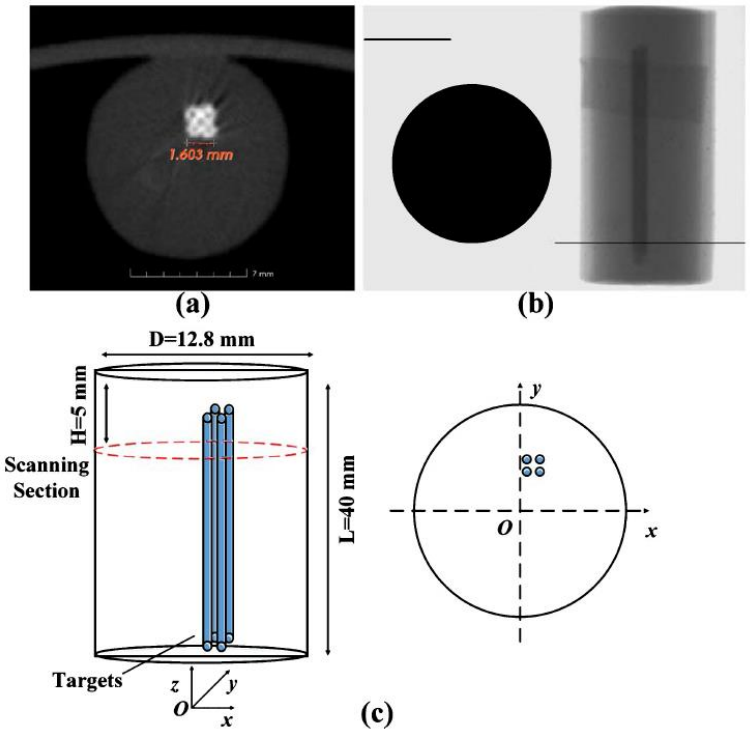

Figure 2.3. (a) A microCT image of the phantom embedded with four targets; (b) A side view projection image of the phantom (right) and a penny (left) for reference; (c) Phantom geometry for the phantom experiment.

2.1.3. Results of the numerical simulations

Using the MM algorithm, we reconstructed the XLCT images from the numerical simulations using measurements for the different beam sizes. The reconstructed images are plotted in Fig. 2.4 for the target diameters of 1.0, 0.5, 0.2, and 0.1 mm in the 1st, 2nd, 3rd,

and 4th row, respectively. In the same figure, the 1st, 2nd, 3rd, and 4th columns, from left to right, represent the XLCT images acquired with the beam sizes of 1.0, 0.5, 0.2, and 0.1 mm, respectively. Fig. 2.5 plots the zoomed-in pictures of the corresponding target regions in Fig. 2.4. In Figs. 2.4 and 2.5, the green circles represent the true target size and position for each case. From the figures, it can be seen that scanning with a smaller beam size achieves a better XLCT image quality. From Fig. 2.5, as indicated by the images in the 1st row in 1st column, 2nd row in 2nd column, 3rd row and 3rd column, and 4th row in 4th column, we can see that the 6 targets can be successfully reconstructed when the x-ray beam size is equal to the EtE distance. The image quality degrades when larger x-ray beams are used and indicates that the targets cannot be well separated when the objects are scanned with an x-ray beam size that is larger than the EtE distance.

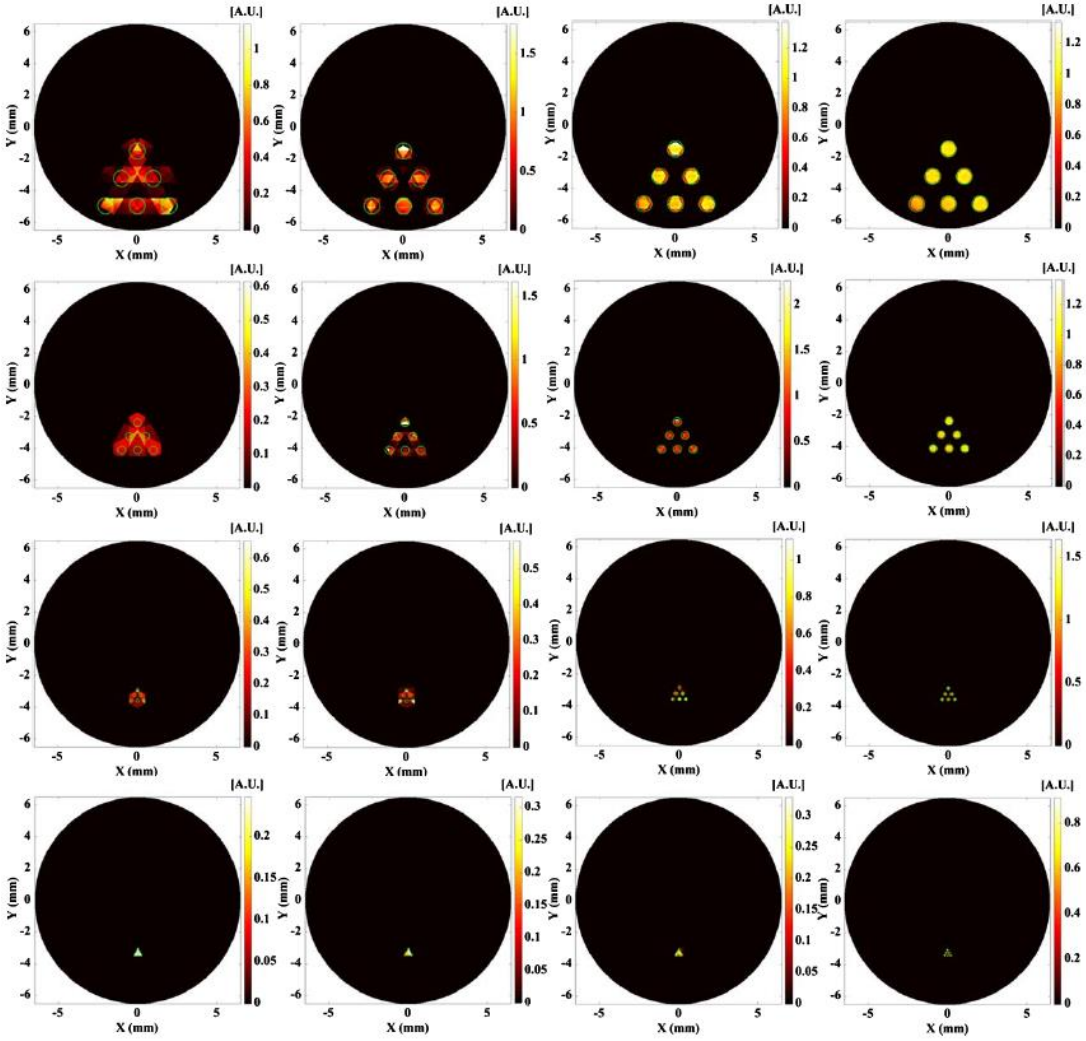

Figure 2.4. Reconstructed XLCT images for the numerical simulations for different target diameters of 1.0, 0.5, 0.2, and 0.1 mm in the 1st, 2nd, 3rd, and 4th row, respectively, and scanned with an x-ray beam diameter of 1.0, 0.5, 0.2, and 0.1 mm in the 1st, 2nd, 3rd, and 4th column from left to right.

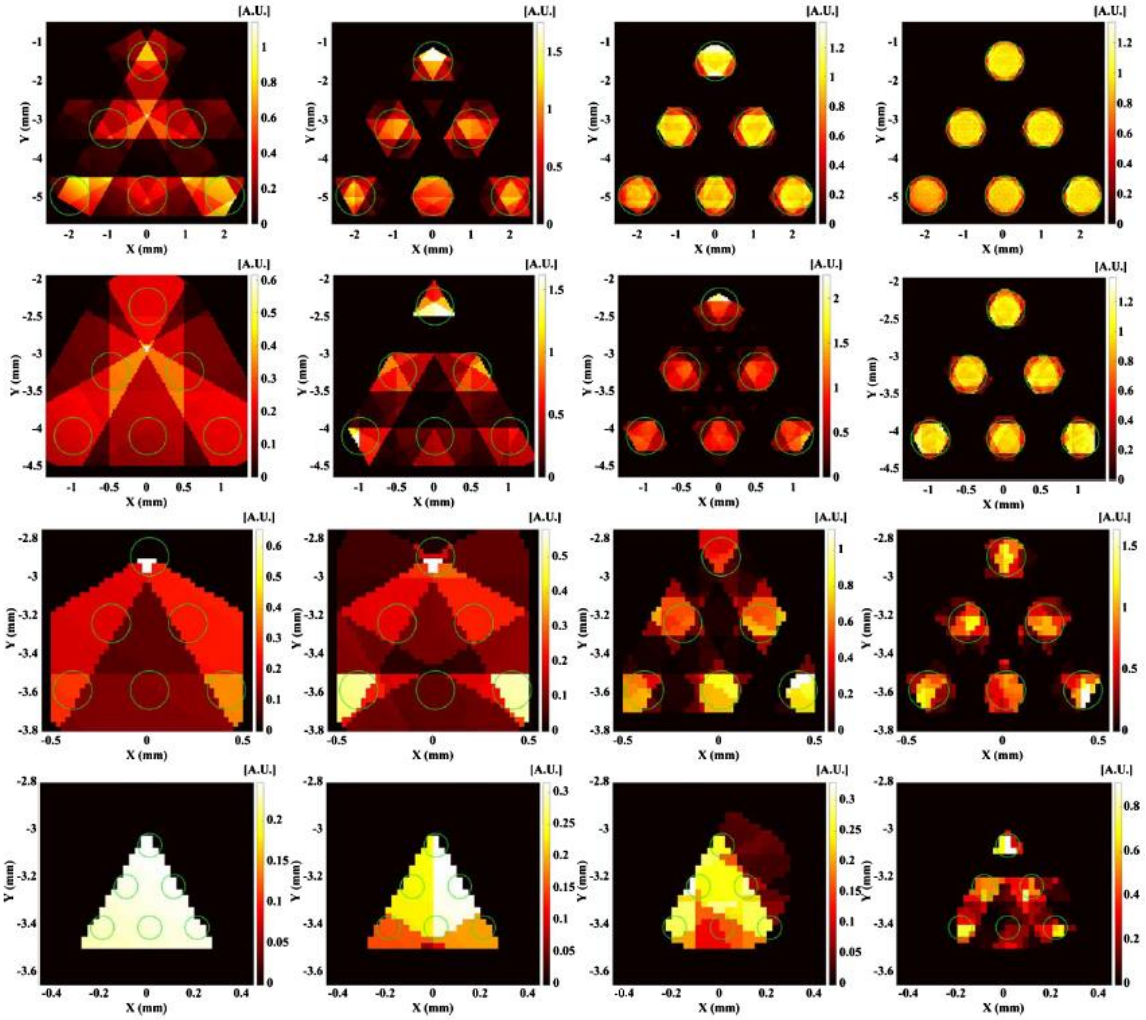

Figure 2.5. The zoomed-in target region corresponding to the simulation results shown in Fig. 2.4. Each row and column represent the same cases as before.

Fig. 2.6 plots the numerical simulation results of the 6-target phantom with target diameters and EtE distances of 0.1 mm, scanned by a superfine beam of 0.1 mm for different angular projections of 3, 6, 12, 24, and 36, respectively. It can be seen in Fig. 2.6 that with more angular projections, the reconstructed image quality improves substantially. For simplicity, only the line profile across the middle targets is plotted. The quantitative image quality metrics were calculated from these profile plots and is listed in Table 2.1. The results from the reconstruction with 36 angular projections had the lowest TSE and CDE while having the closest DICE to 100%, which further validates that more projections can lead to a better XLCT image quality. From these results, we can see that we can obtain a spatial resolution of 200 μm if an x-ray beam size of 100 μm is used.

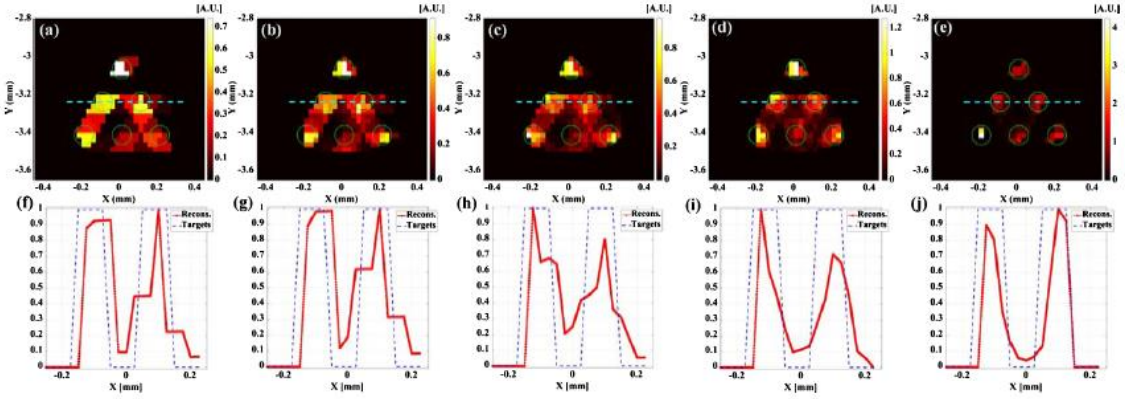

Figure 2.6. Reconstructed XLCT and corresponding line-profile plots for the numerical simulations with angular projections of 3 (a, f), 6 (b, g), 12 (c, h), 24 (d, i), and 36 (e, j). The dotted blue line indicates the horizontal line-profile position.

Table 2.1. Quantitative image quality metrics for the numerical simulations of different angular projections

Number of Angular Projections	Diameter (mm)/TSE	CtCD (mm)/CDE	DICE
3	0.154/58.3%	0.183/8.38%	60.9%
6	0.174/72.5%	0.173/13.8%	56.8%
12	0.169/69.3%	0.169/15.4%	56.0%
24	0.158/57.8%	0.165/17.4%	62.7%
36	0.110/9.8%	0.184/7.9%	78.4%

2.1.4. Results of phantom experiment

Again, we used the MM algorithm to reconstruct the XLCT images from the phantom experiments, as in the numerical simulations. For the XLCT reconstruction, we used the same finite element mesh as the numerical simulations. The reconstructed transverse section was also discretized with a 2D grid of 100 μm^2 pixel size and the measured x-ray beam size models were applied in the reconstruction. We previously measured the x-ray beam diameter and average intensity (intensity per pixel) which indicated that the collimated x-ray beams had a conical shape and the beam size changes linearly with distance. For the 0.1 mm collimator, the beam size changed from 160 to 190 μm in the phantom region with a size of 175 μm in the phantom center. Intensity curves showed that the x-ray intensity attenuates exponentially along a straight line. The measured beam size and intensity were fitted with models that were applied in the XLCT reconstruction following the phantom experiment.

Fig. 2.7(a) plots a single transverse section of the microCT image corresponding to the scanned section in the XLCT imaging. Fig. 2.7(b) shows the results of the XLCT reconstruction with a zoom-in of the target region in Fig. 2.7(c). We plotted two line profile plots (horizontal and vertical) as indicated by the blue and magenta lines in Fig. 2.7(c) in Fig. 2.7(d) and Fig. 2.7(e), respectively. We can see that all four targets have been separated and reconstructed successfully at the correct locations in the reconstructed image as shown

in Fig. 2.7 (b, c). We calculated the reconstructed image quality metrics as listed in Table 2.2. The reconstructed CtCD is 0.9036 at the FWTM with a CDE of 24.8% for vertical targets. The DICE of the reconstruction was calculated to be 39.3%. Based on the reconstructed image as the evaluated image quality metrics, multiple deeply embedded targets can be reconstructed successfully using a superfine x-ray beam.

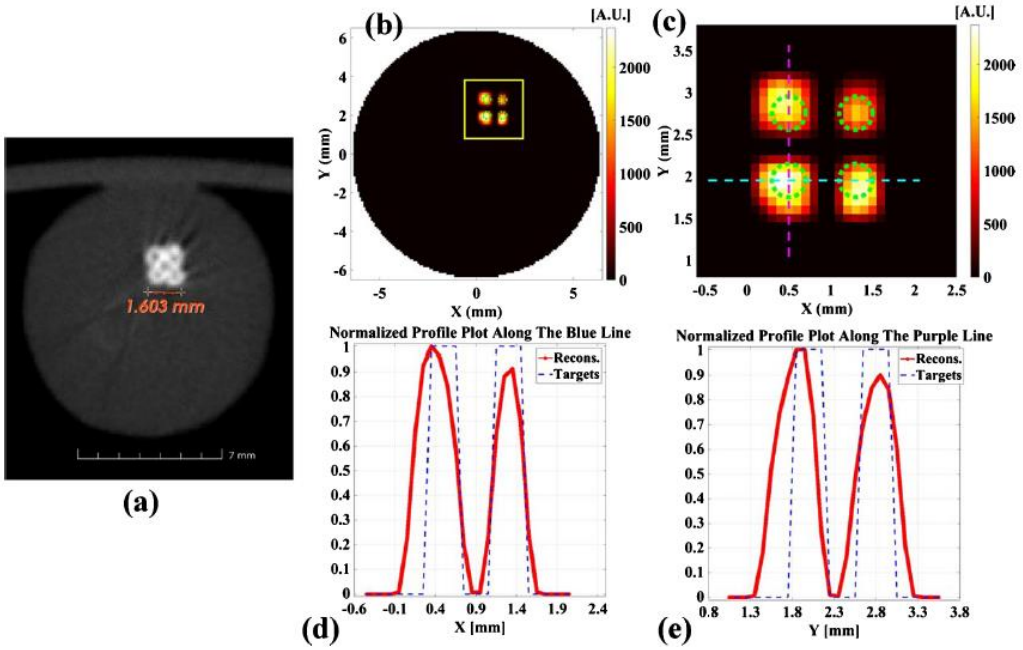

Figure 2.7. Reconstructed XLCT results for the phantom experiment with four targets. (a) A transverse section from the reconstructed microCT image; (b) The reconstructed XLCT image; (c) Zoomed-in target region; (d) The horizontal profile plot (blue line in (c)); (e) The vertical line profile plot (magenta line in (c)).

Table 2.2. Quantitative image quality metrics for phantom experiment

	Diameter (mm)/TSE	CtCD (mm)/CDE	DICE
Horizontal Targets	0.715/78.7%	0.904/13.0%	39.3%
Vertical Targets	0.803/100.6%	0.999/24.8%	

2.1.5. Discussion and conclusions

From the experimental results described in Section 2.1.4, we can see that XLCT can image and separate deeply embedded targets with an EtE distance as small as 0.4 mm using measurements from six angular projections with a superfine x-ray beam of 0.175 mm diameter. Our numerical simulation results (Section 2.1.3) demonstrated that XLCT can achieve a spatial resolution of about two times the scanning x-ray beam diameter. Thus, for our experimental system, we expect to achieve a spatial resolution of 0.35 mm using a superfine beam of 0.175 mm. At this time, we could not verify this experimentally as we could not make targets of such size at that time. We will need to investigate ways to fabricate smaller targets in future works.

To compare our experimental results with numerical simulations directly, we performed an additional numerical simulation with the same phantom geometry and scanning scheme as in the phantom experiment. The numerical measurements were generated using our forward model with 50% Gaussian noise. We also included the real x-ray beam size in the forward model for this simulation and the results are shown in Fig. 2.8. The DICE for the simulation was calculated to be 58.5% which is greater than the 39.3% for the experimental case. Comparing our results from Figs. 2.7 and 2.8, we can see that in both cases, the four targets are reconstructed successfully. However, the numerical simulation has slightly better results, which is reasonable as there are many factors in the experiment that can deteriorate our results, for example the target fabrication and implantation.

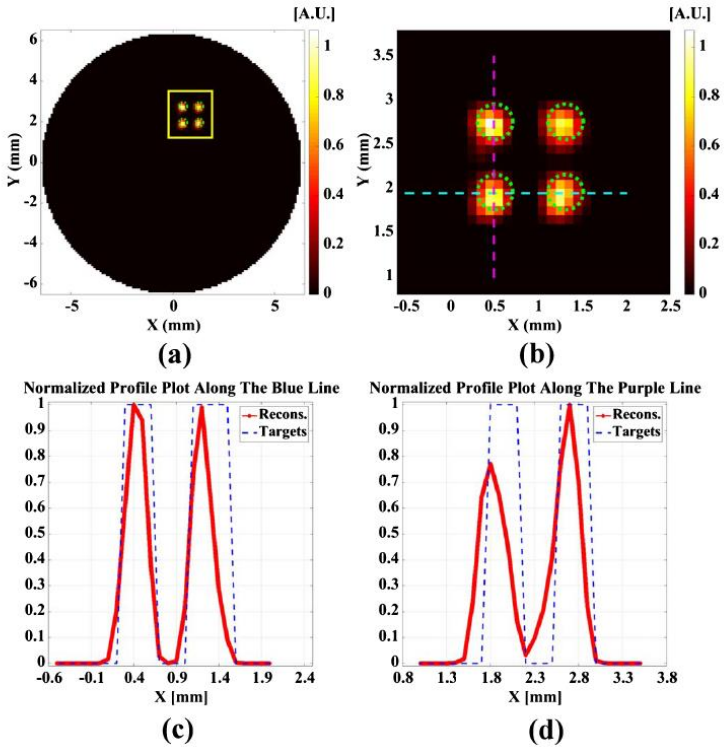

Figure 2.8. Numerical simulation results for the same set-up as the phantom experiment. (a) Reconstructed XLCT image; (b) Zoomed-in target region; (c) Horizontal line profile plot (blue line in (b)); (d) Vertical line profile plot (magenta line in (b)).

The numerical simulation and phantom experiments indicate that the x-ray beam size is a key factor for achieving high-spatial resolution in XLCT imaging. We demonstrated that it is currently impossible to separate two targets when the x-ray beam size is larger than the target EtE distance, as seen in Figs. 2.4 and 2.5. When the x-ray beam size is close to the EtE distance, it is possible to separate the targets. We have also performed numerical simulations with measurements at different angular projections which indicate that more angular projections can result in a better image quality, especially for cases when the x-ray beam diameter is close to the EtE distance.

There are many factors in quantifying the reconstructed values since XLCT is a quantitative imaging modality. Each factor will need careful calibrations, which is beyond the scope of this work. Our goal was to show that XLCT can achieve a high-spatial resolution with a superfine x-ray beam and demonstrate how the x-ray beam size and number of angular projections can affect the spatial resolution.

With the current set-up, it took a long time to acquire our measurements at six projections. Currently, the measurement time is 6×65×20 seconds or 130 minutes. We will work to pursue new scanning schemes in order to acquire our measurements in a shorter time which will be discussed in the following sections. Using a collimator with a small pinhole, we shown that we can generate x-ray beams of 0.175 mm diameter. However, this method is rather inefficient as most of the x-ray photons are absorbed by the collimator, resulting in a low x-ray photon utilization efficiency, which contributes to the long measurement time. Using a focused x-ray beam would be a better choice for future XLCT imaging systems and will be discussed in Section 2.3.

In conclusion, we have built a prototype XLCT imaging system with a collimated superfine x-ray beam. With numerical simulations and phantom experiments, we have demonstrated the spatial resolution of XLCT depends on the scanning x-ray beam size and that a spatial resolution of about double the x-ray beam diameter can be achieved for imaging deeply embedded phosphor targets.

2.2. Multiple Pinhole Collimator Based XLCT Imaging

For the traditional NB-XLCT design, the long data acquisition time is a concern because only a single x-ray beam is collimated to sequentially scan an object (single-beam scanning strategy). One can reduce the data acquisition time by using a higher flux x-ray beam (larger tube current and x-ray photon energy for shorter exposure times), however the increase in radiation dose is not desired. We could also increase the diameter of the x-ray beam, but as seen in Section 2.1.3, this comes at the cost of a compromised spatial resolution. Hence, in this work to further reduce the data acquisition time, we proposed a multiple pinhole collimator based XLCT system, where multiple x-ray beams were generated to scan the object simultaneously. We also measured the radiation dose in XLCT imaging in this study.

2.2.1. Scanning scheme in multiple-beam XLCT imaging

In both scanning schemes of a single narrow and a single pencil beam XLCT, the object is scanned by a sequence of single x-ray beams moving at predefined directions and positions, which is similar to the first generation computed tomography (CT) scanning mode, so that it usually takes a long time to acquire data. For each angular projection, the linear scan step size is usually set to be same as the collimated x-ray beam diameter, which is also a critical factor in improving the spatial resolution of XLCT. Although a powerful x-ray source can be used to reduce the camera exposure time for each linear scanning, the

x-ray dose will be increased, which, as mentioned before, is not desired. To reduce the data acquisition time, we propose a multiple-beam scanning strategy using multiple pinhole collimators.

As shown in Fig. 2.9(a), in the single-beam scanning strategy, for each angular projection, the number of linear scanning steps (N_L) is determined by the diameter of the entire scanning region (D_{reg}) and the beam diameter (D_{beam}) as $N_L = D_{reg} / D_{beam}$. Accordingly, in the multiple x-ray beam scanning strategy (Fig. 2.9(b)), parallel x-ray beams are distributed evenly and scan the object at multiple positions simultaneously. For each angular projection, the number of linear scan steps is calculated by the width of the interval region between the x-ray beams (W_{int}) and D_{beam}, so $N_L = W_{int} / D_{beam} = (D_{reg} / N_{beam}) / D_{beam}$, where N_{beam} is the number of parallel x-ray beams. The scanning region for each beam is reduced by using the multiple-beam scanning method, which means that we can speed up the data acquisition time by N_{beam} times.

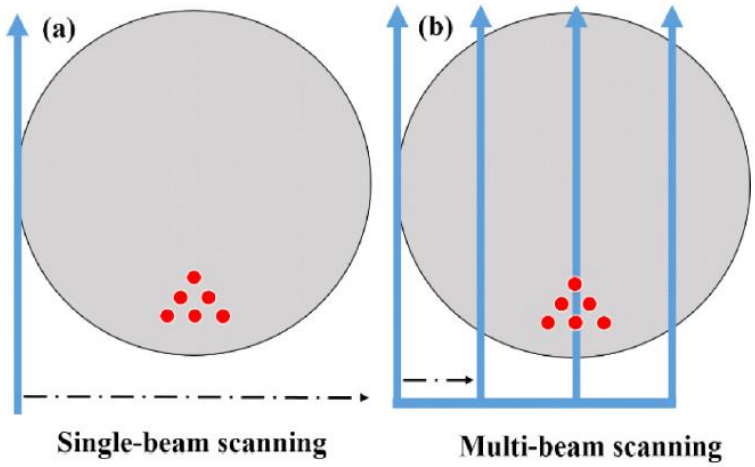

Figure 2.9. Schematic of linear scan set-up for one typical angular projection. (a) Single beam scanning strategy; (b) Multiple beam scanning strategy. Red dots represent targets and blue arrows represent the x-ray beams.

2.2.2. Pinhole design and measurement of the collimated x-ray beam size and intensity

In the experimental study with multiple x-ray beams, we designed a two-pinhole collimator as seen in Fig. 2.10. The collimator was made from a 5 mm thick steel disk as shown in Fig. 2.10(c). Two small pinholes were drilled through the disk with a diameter of 0.5 mm each. The distance from the disk center to each pinhole is 2.4 mm (L_1 in Fig. 2.10(c)). The multiple-pinhole collimator was used in the XLCT experimental system described in Section 2.1.2. To validate our design, we placed an x-ray detector at the phantom position to measure the collimated x-ray beam sizes. As shown in Fig. 2.10(d) and Fig. 2.10(e), the collimated x-ray beam spot size was measured as 0.5 mm with center-to-center distance of 6 mm. The beam size and intensity at different distances from the pinhole were measured as described in the following paragraph.

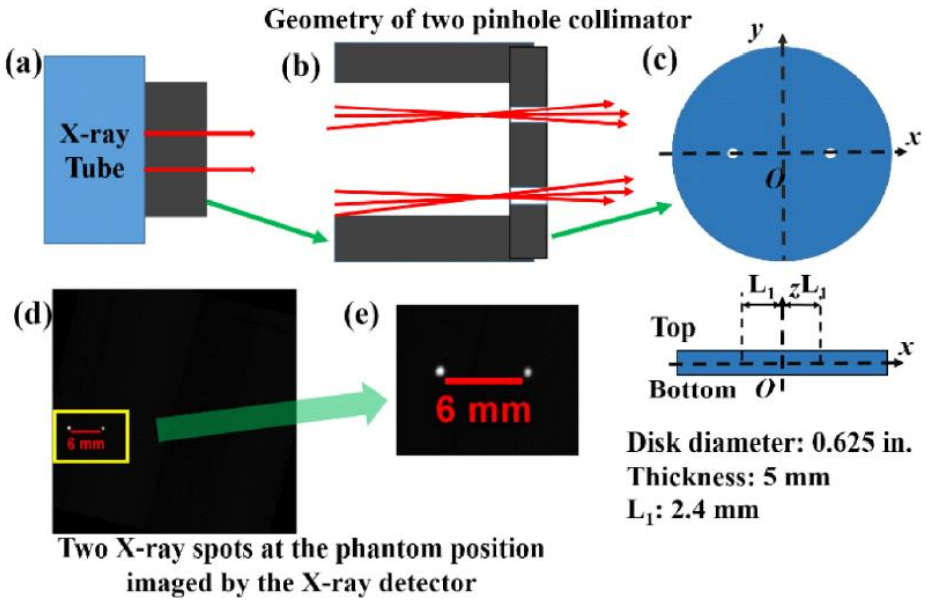

Figure 2.10. Pinhole design for the experimental study. (a) X-ray tube with a designed collimator; (b) Zoomed-in image of the pinhole design where the red arrows represent the x-ray beams; (c) The schematic drawing of the disk mounted at the end of the cylindrical steel rod; (d) An x-ray detector image of the two generated x-ray beams; (e) Zoomed-in image of the x-ray beams from (d).

Before validating the design with a phantom experiment to be described in Section 2.2.4, we mounted the x-ray detector on top of a linear stage to measure the collimated x-ray beam size and intensity at different distances from the pinhole, as shown in Fig. 2.11. The x-ray tube was operated at 15.3 kVp and 0.2 mA to avoid saturation of the x-ray detector. The step size of the linear stage was 5 mm with 13 steps. At each step, we took an image with the x-ray detector using an exposure time of 370 ms. Using the acquired images, we calculated the center coordinates and equivalent diameter of the multiple collimated x-ray beams.

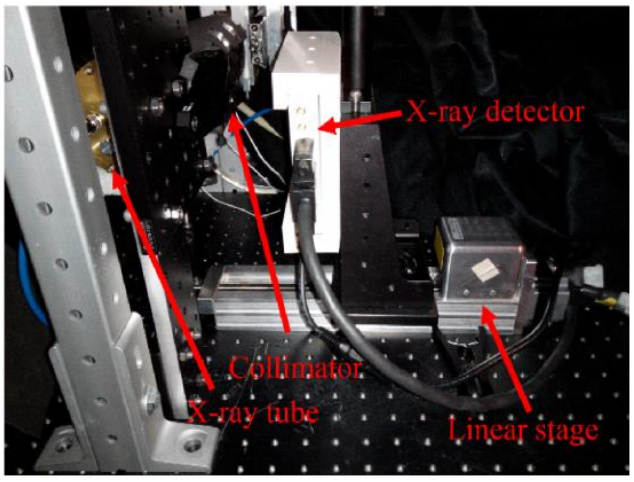

Figure 2.11. A photograph of the experimental set-up for measuring the x-ray beam size and intensity along the x-ray beam at different distances from the collimator.

Fig. 2.12 and Fig. 2.13 show the beam diameter, the profile plots across the x-ray spot, maximum intensity and average intensity (intensity per pixel) for the two x-ray beams, respectively. The measured beam diameter and profile plots demonstrate that the x-ray beams are conical and the beam diameter changes linearly as the distance increases, as shown in Figs. 2.12(a), 2.12(b) and 2.13(a), 2.13(b). The intensity curves in Figs. 2.12(c), 2.12(d) and 2.13(c), 2.13(d) show that the x-ray photon intensity attenuates exponentially along a straight line in the air, following the relationship expressed in Eq. (1.3). Figure 2.14 plots the interval of the two x-ray beams at different distances. From the plot, we see that the interval increases linearly as the distance increases.

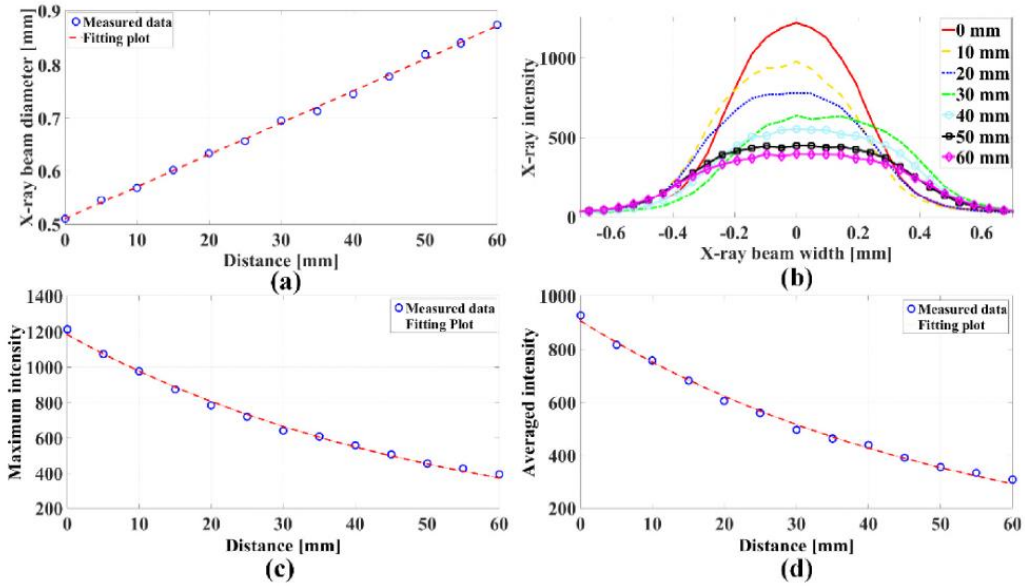

Figure 2.12. Measurement and fitting of one collimated x-ray beam diameter and intensity. (a) X-ray beam diameter at different distances from the collimator; (b) Profile plot across the x-ray beam at varying distances; (c) Maximum intensity at different distances; (d) Mean x-ray beam intensity at different distances.

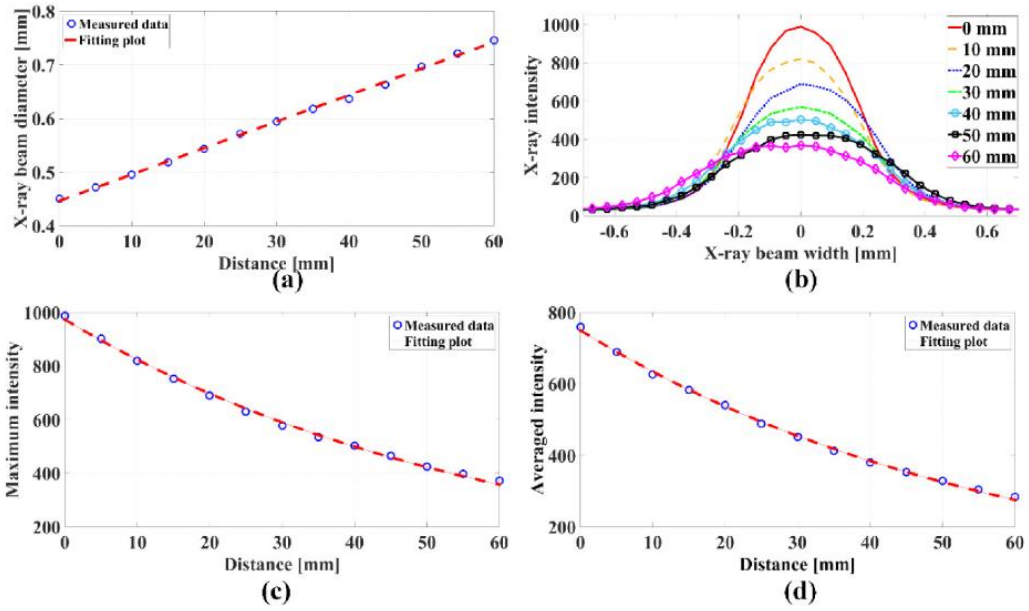

Figure 2.13. Measurement and fitting of the second collimated x-ray beam diameter and intensity. (a) X-ray beam diameter at different distances from the collimator; (b) Profile plot across the x-ray beam at varying distances; (c) Maximum intensity at different distances; (d) Mean x-ray beam intensity at different distances.

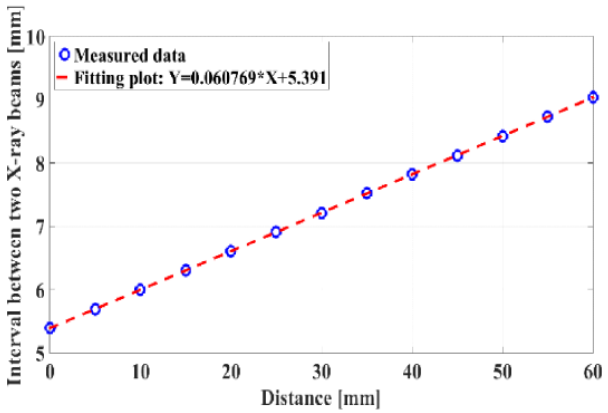

Figure 2.14. Measured interval between the two x-ray beams at different distances. A fitting plot is also included.

2.2.3. Numerical simulations of multiple-beam XLCT imaging

To validate our proposed multiple-beam scanning strategy for XLCT imaging, we performed two numerical simulations with a two target case and a six target case. For all simulation studies, we generated a 10 mm long cylindrical phantom with a diameter of 12.8 mm. The optical properties of the phantom were set to be μ_a of 0.0072 mm^{-1} and $\mu`_s$ of 0.72 mm^{-1} at the wavelength of 703 nm. The x-ray attenuation coefficient was set to be μ_x = 0.0214 mm^{-1}. There were no phosphor particles in the background phantom. For the two target case, we had two cylindrical targets with a diameter of 0.5 mm and a height of 6 mm embedded inside the phantom with center positions coordinates of (−0.5 mm, −3.2 mm)

and (0.5 mm, −3.2 mm), as shown in Fig. 5(a). For the six target case, multiple targets with a diameter of 0.2 mm and a height of 6 mm were embedded in the phantom. The positions of the six targets are shown in Fig. 5(b), from which we see that the target center-to-center distance was 0.4 mm. For both numerical simulation studies, we set the phosphor particle concentration to be 1.0 mg/mL in targets and 0 in the background.

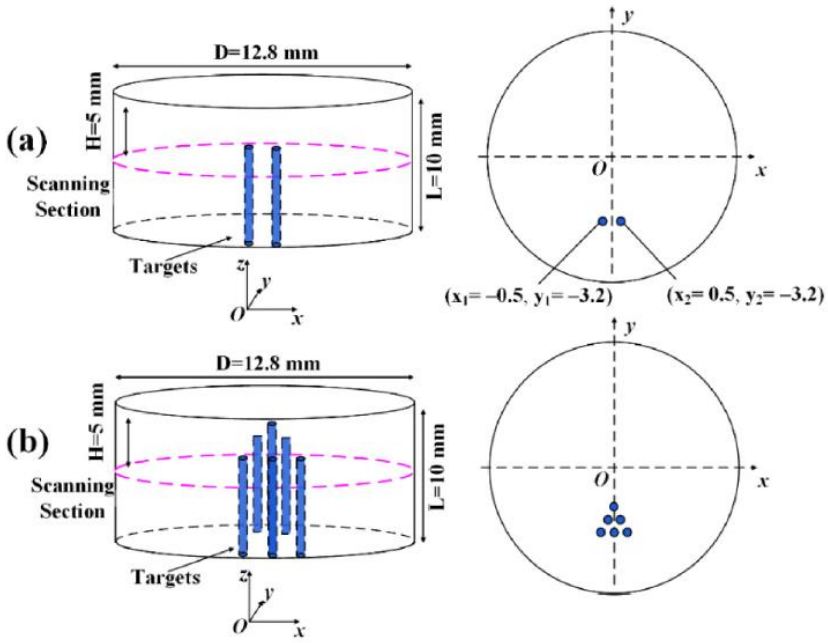

Figure 2.15. The phantom geometry used for numerical simulations with two targets (a) and six targets (b).

For both simulation cases, we used four x-ray beams to scan the phantom at a depth of 5 mm under the phantom top surface. The x-ray beam diameter and the linear scan step size were set to be 0.1 mm. The interval was 3.2 mm so that 32 linear steps will be enough to scan the whole section of the phantom. For both numerical simulations, we used 6 angular projections with the angular step size of 30 degrees. For each angular projection, there were 32 linear scan steps. The numerical measurements were generated from the forward modeling in which the phantom was discretized by a finite element mesh with 26,638 nodes, 153,053 tetrahedral elements and 11,456 face elements. Finally, 50% Gaussian noise was added to the numerical measurements.

In XLCT, the propagation of collimated x-ray beams is usually treated as parallel straight lines. Chen *et al*. incorporated the real shape of the collimated narrow x-ray beams in the model and collected the measurement data from two perpendicular directions to speed up the scanning time [28]. Here, we have also taken the real beam shape into consideration. As described in the Section 2.2.2, we measured the collimated x-ray beam size and intensity and found that the collimated pencil x-ray beams were conical. The beam diameter changes linearly as the distance from the collimator increases and the beam intensity attenuates exponentially as described in Eq. (1.3). At the collimator position, we

set the x-ray beam diameter d_0 = 0.1 mm and the slope k was set to be 0.004. The beam diameter at position $\vec{r}$ can then be expressed as:

$$d(\vec{r}) = k \times L(\vec{r}) + d_0 \tag{2.1}$$

where $L \in [0, 12.8]$ is the distance in mm from the collimator to position $\vec{r}$. Therefore, the range of the beam diameter is [0.1, 0.1512]. In the simulations, the original x-ray beam intensity was set as $T_0 = 1$ with $\mu_x = 0.0214$ mm^{-1}.

For both simulation cases, we have included conical x-ray beams in the forward model. To evaluate the effects of the beam divergence in the XLCT reconstruction, we compared image quality metrics in the reconstructed XLCT images using both the conical beams (beam divergence included) and straight parallel beams (no divergence). We also compared image quality metrics between the single-beam scanning strategy and the proposed multiple-beam scanning strategy. Then, to investigate how the number of x-ray beams affects the XLCT imaging quality, we repeated the two numerical simulation cases using 8 and 16 evenly distributed parallel x-ray beams. We used numerical measurements at 6 angular projections for both bases. The linear scan step size is 0.1 mm for both cases with a linear scan step number of 16 for the 8 beam case and 8 for the 16 beam case.

The scanned transverse section was discretized with a 2D grid with a pixel size of 25 μm^2. The system matric generated with the finite element mesh was interpolated onto the fine 2D grid. During the XLCT reconstruction we applied L^2 regularization in the MM framework. Fig. 2.16 and Fig. 2.17 shows the reconstructed XLCT images for the numerical simulations of the two target case and six target case, respectively.

For the two-target case, Figs. 2.16(a, c) show the reconstruction results of the parallel x-ray beam model with one and four x-rays beams, respectively. Fig. 2.16(b, d) shows the cone shaped x-ray beam model with one and four x-rays beams, respectively. The image quality metrics for both cases are listed in Table 2.3. Based on Fig. 16 and Table 2.3, we can see that the two targets have been reconstructed successfully with good shapes at the correct locations and with a clean background. For the parallel beam model, we had slightly lower DICE of 81.7%, compared with the conical beam model where the DICE was 91.7% in the four beam case. There are negligible error increases when we compare the single and multiple beam cases, which validates our proposed multiple-beam scanning strategy for XLCT imaging. The same trend can be seen in the six target cases shown in Fig. 2.17 and the image quality metrics listed in Table 2.4. Comparing the results from the parallel and conical beam models, we can see that the conical beam model can improve the reconstruction results and obtain smaller errors, especially with the CDE and DICE.

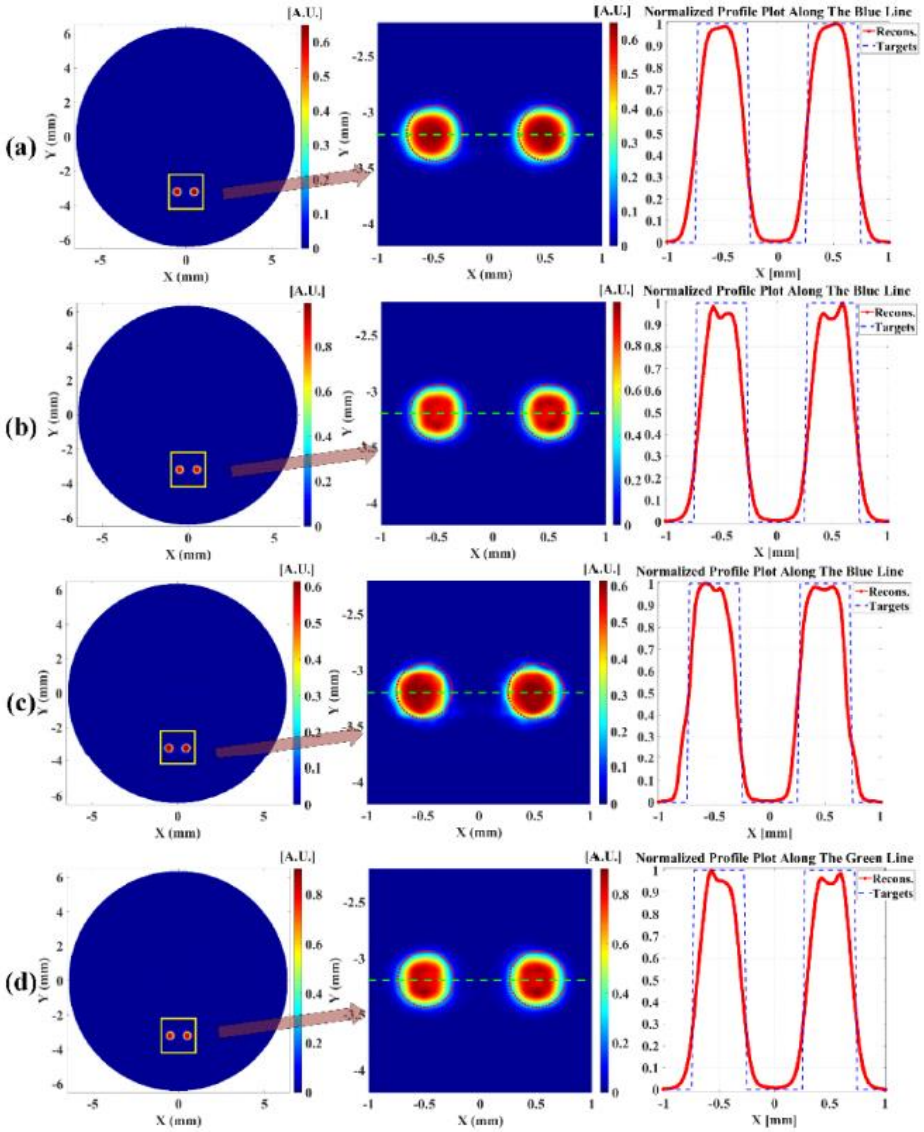

Figure 2.16. Reconstructed XLCT images (left column), zoomed in regions (middle column) and normalized profile plots (right column) for numerical simulation with two targets. (a) Reconstructed XLCT image with single parallel x-ray beam scan; (b) Reconstructed XLCT image with single conical x-ray beam scan; (c) Reconstructed XLCT image with four parallel x-ray beam scan; (d) Reconstructed XLCT image with four conical x-ray beam scan. The dotted green line indicates the profile position.

Table 2.3. Quantitative image quality metrics for numerical simulations with two targets for single and four x-ray beams.

	Diameter (mm)/TSE	**CtCD (mm)/CDE**	**DICE**
Single parallel beam	0.608/21.6%	1.0235/2.35%	84.6%
Single conical beam	0.5417/8.35%	1.0023/0.23%	93.7%
Four parallel beams	0.6115/22.3%	1.022/2.2%	81.7%
Four conical beams	0/555/11.0%	1/0045/0.45%	91.3%

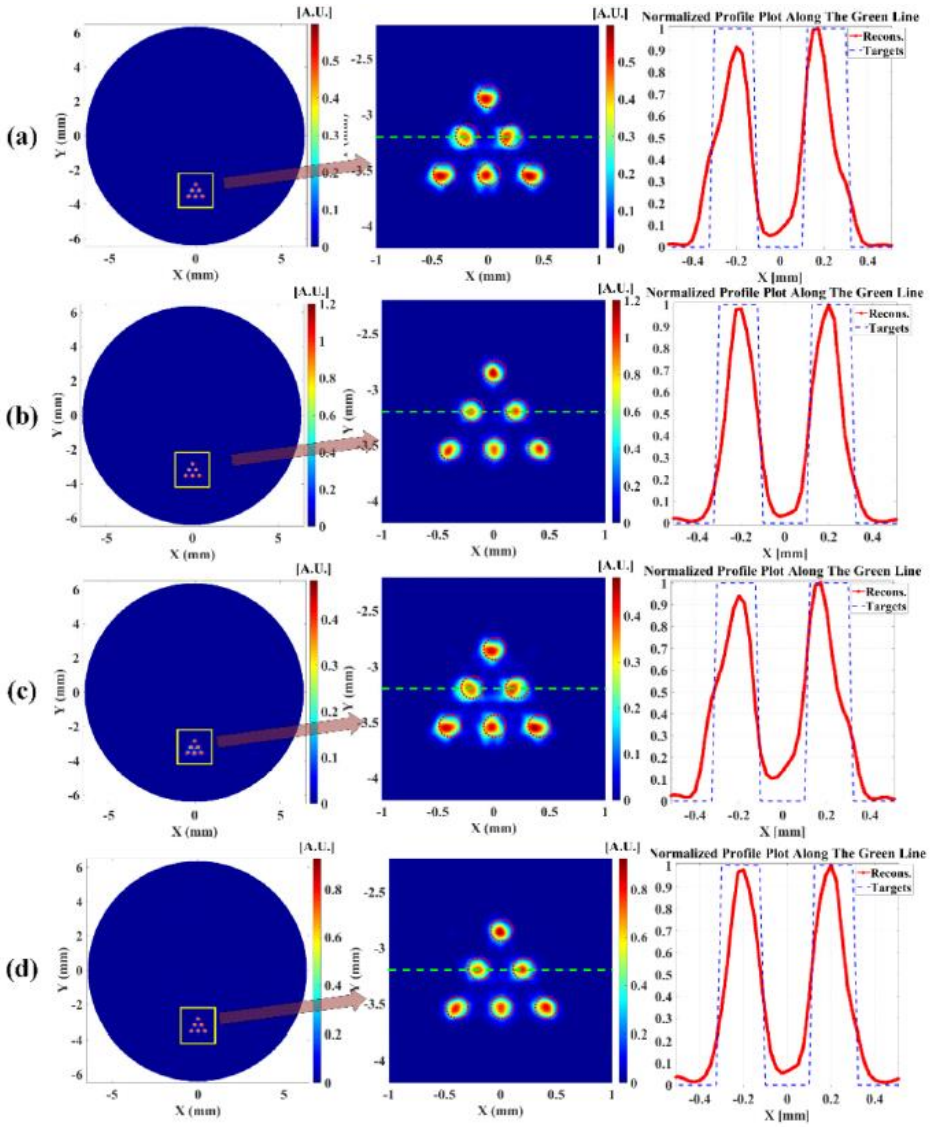

Figure 2.17. Reconstructed XLCT images (left column), zoomed in regions (middle column) and normalized profile plots (right column) for numerical simulation with six targets. (a) Reconstructed XLCT image with single parallel x-ray beam scan; (b) Reconstructed XLCT image with single conical x-ray beam scan; (c) Reconstructed XLCT image with four parallel x-ray beam scan; (d) Reconstructed XLCT image with four conical x-ray beam scan. The dotted green line indicates the profile position.

Table 2.4. Quantitative image quality metrics for numerical simulations with six targets for single and four x-ray beams.

	Diameter (mm)/TSE	CtCD (mm)/CDE	DICE
Single parallel beam	0.3112/55.62%	0.4177/4.44%	58.0%
Single conical beam	0.2663/33.14%	0.4032/0.81%	71.6%
Four parallel beams	0.372/86%	0.372/7.0%	52.0%
Four conical beams	0.3165/58.25%	0.3755/6.13%	65.3%

We plot the results showing the effects of the number of parallel x-ray beams used in the multiple beam scanning strategy for 8 and 16 x-rays beams in Fig. 2.18. We found that the image quality degraded substantially but could recover the targets using 8 x-ray beams. The reconstructed XLCT images could not reconstruct all six of the targets when 16 beams were used. This is likely due to the mutual effects of the simultaneously emitted optical photons at multiple beam locations with short distances when the multiple beams were applied simultaneously. With sparser x-ray beams, such as with two or four beams, the emission locations are resolved better with our XLCT reconstruction algorithm.

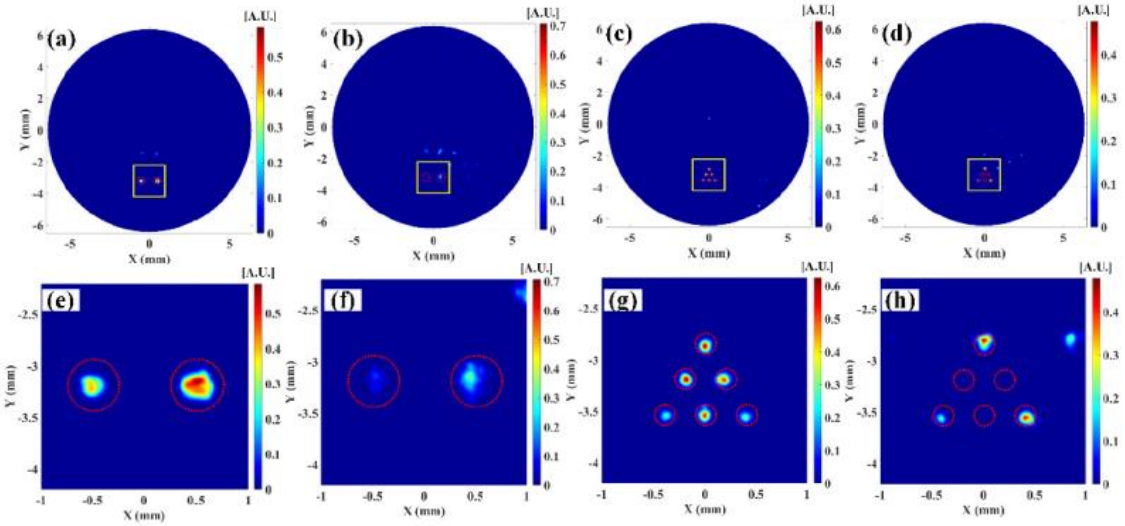

Figure 2.18. Reconstructed XLCT images (top row) and zoomed regions (bottom row) for numerical simulation with two and six targets: reconstructed images for two target case with 8 parallel x-ray beam scan (a) and 16 parallel x-ray beam scan (b); reconstructed images for six targets with 8 parallel x-ray beam scan (c) and 16 parallel x-ray beam scan (d). The images in bottom row (e-h) are the zoomed images of their corresponding images of the same column in the top row.

2.2.4. Phantom experiment with multiple-beam XLCT imaging

To validate our multiple-beam XLCT imaging system, we performed a phantom experiment with two capillary tube targets. The geometry of the experimental phantom with two targets is shown in Fig. 2.19(a). The cylindrical phantom (40 mm long, 25 mm in diameter) was made of 1% Intralipid and 2% Agar to mimic the optical properties of a small animal. The target was composed of 1% intralipid, 2% agar and GOS:Eu^{3+} particles at the concentration of 10 mg/ml, and filled in two capillary tubes. The capillary tubes had an inner diameter of 1.0 mm and an outer diameter of 1.6 mm. The scanning section was 5 mm under the top surface. According to the x-ray projection pictures shown in Fig. 6(c), the capillary tubes were placed side by side and the target center-to-center distance was 1.6 mm.

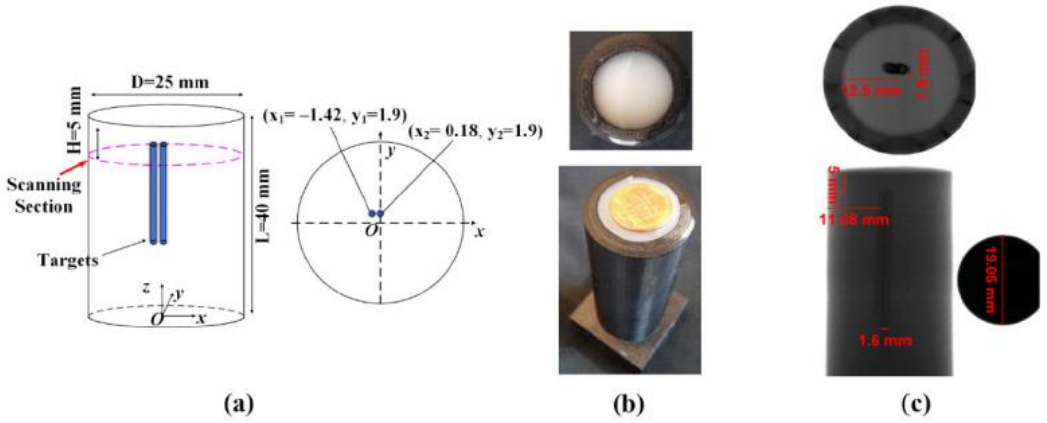

Figure 2.19. Geometry of the phantom used in experimental study; (b) The white light photos of the physical phantom (white) inside its plastic mold (black) with a penny (golden) as reference; (c) The x-ray projection pictures of the phantom inside its plastic mold from top and side views, and the reference penny (the rightmost picture).

For all XLCT measurements, the EMCCD camera was operated at -92ºC with the maximum EM Gain of 255 and analog gain of 5. The x-ray tube current was 1.2 mA at a tube voltage of 30 kVp. Based on the x-ray spot size and beam interval of the two pinhole collimator (Fig. 2.10), 24 linear scan steps with a step size of 0.5 mm for each angular projection was sufficient to scan the transverse section of the phantom. We took measurements at 6 angular projections with an angular step of 30 degrees. For each linear scan, the EMCCD camera exposure time was 10 seconds and the linear stage moving time was 2 seconds. The total measurement time was 29.8 minutes. Compared with the single-beam scanning method, one half of scanning time was saved by using multiple-beam scanning strategy in this experiment. After XLCT imaging, we have scanned the phantom with our lab-made microCT imaging system, in which the x-ray tube had a current of 0.5 mA and a tube voltage of 50 kVp. A filtered back-projection algorithm was used to reconstruct the microCT image with a Shepp-Logan filter.

For the XLCT reconstruction, the phantom was discretized by a finite element mesh with 26,638 nodes, 153,053 tetrahedral elements and 11,456 face elements. The reconstructed section was discretized with a 2D grid with a pixel size of 100 μm^2. The sensitivity matrix of the 2D grid was interpolated from a sensitivity matrix based on the finite element mesh. The L^2 regularized MM algorithm was applied here to reconstruct the XLCT image, as shown in Fig. 2.20. We have applied the x-ray beam diameter changes and the x-ray attenuation models in the XLCT reconstruction (the conical x-ray beam case) with the reconstructed XLCT image plotted in Fig. 2.20(e). For comparison, we have also used the parallel x-ray beam model (the unchanged beam diameter and intensity) in the XLCT reconstruction and plotted the image in Fig. 20(b). Figure 2.20(a) plots the microCT image of the phantom with two targets. From Figs. 2.20(a), 20(b) and 20(e), we see that two targets have been reconstructed successfully at the correct location. To analyze the reconstructed XLCT image quantitatively, we have calculated the image quality metrics as

shown in Table 2.5. The TSE, CDE and DICE are 10%, 16.74 and 85.8% for the parallel beam case and 8.2%, 2.84 and 85.1% for the conical beam case. All these quantitative image quality metrics indicate that multiple deeply embedded targets can be reconstructed successfully by using multiple beam scanning method and the conical beam model performs slightly better than the parallel beam model, which is consistent with our findings in the numerical simulations.

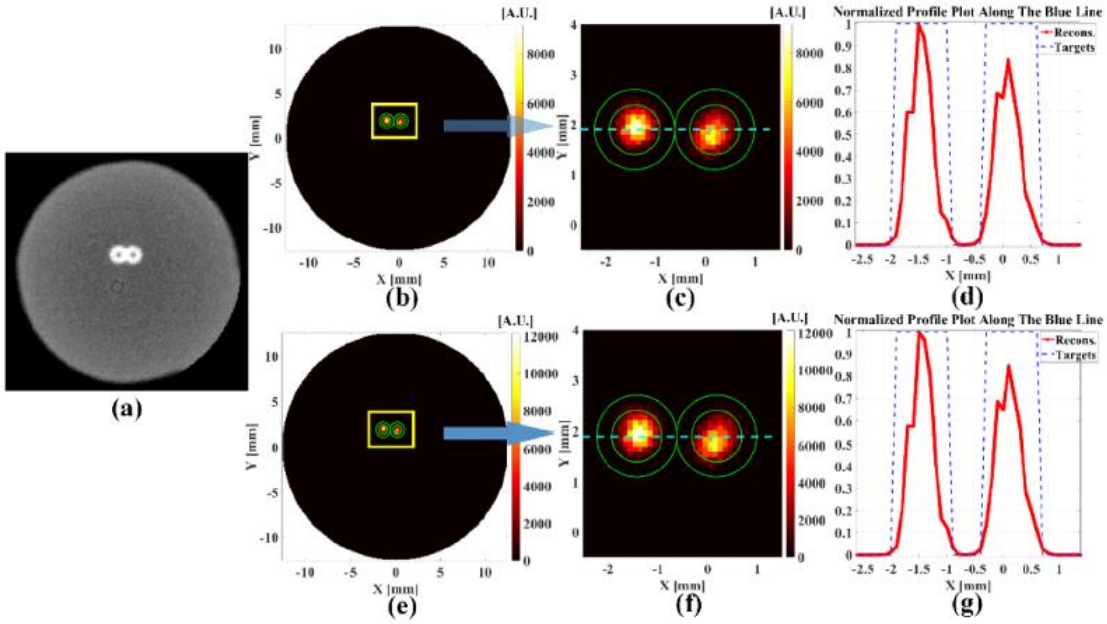

Figure 2.20. A transverse section from the reconstructed microCT image of the phantom with two targets; (b) The reconstructed XCLT image with two parallel x-ray beams; (c) The zoomed in region in (b); (d) The normalized profile plot across the targets in (c); (e) The reconstructed XLCT image with two conical x-ray beams; (f) The zoomed region in (c); (g) The normalized profile plot across the targets in (f). The green circles are the inner and outer walls of the plastic tubes. The dotted line indicates the profile position.

Table 2.5. Quantitative image quality metrics for the phantom experiment

	Diameter (mm)/TSE	CtCD (mm)/CDE	DICE
Two parallel beams	0.9/10%	1.332/16.74%	85.8%
Two conical beams	0.9179/8.2%	1.555/2.84%	85.1%

2.2.5. Measurement of the radiation dose in XLCT imaging

In order to determine the accumulated x-ray dose in the object when scanned by the two beam XLCT system, we performed a dose measurement experiment as shown in Fig. 7. The x-ray radiation dose was measured using an Accu-Dose system (Radcal, Monrovia, CA) with a general purpose in-beam ion chamber (10X6-6, Radcal). The active component of the ion chamber head has a diameter of 25 mm. The phantom, white color in Fig. 7 (right), was 44 mm in diameter and contained a central hole to fit the ion chamber head and was composed of 1% intralipid and 2% agar as in our prior experiment. The phantom was placed on the rotary stage mounted on the linear stage. The ion chamber was fit into

the phantom center. We then performed a scan using the same experimental set-up as before. We used 24 linear scan steps with step size of 0.5 mm and 6 angular projections with an angular step size of 30° and an exposure time of 10 seconds per linear scan step.

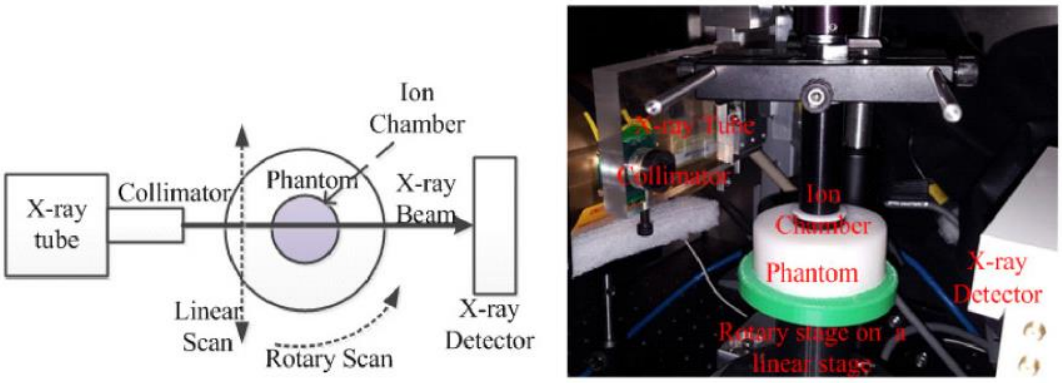

Figure 2.21. The schematic design (left) and a photograph (right) of the x-ray radiation dose measurement set-up.

The total accumulated exposure from the dose measurement was 156.9 mR. Using an *f-factor* (conversion of exposure in air to absorbed dose in muscle at the diagnostic x-ray energy of 70 keV) [64], of 0.94 rad/R (cGy/R), we calculate that the absorbed radiation dose is 0.1475 cGy or 1.475 mSv, which is within the range of a typical CT scan.

2.2.6. Discussion and conclusions

The multiple pinhole collimator based XLCT is an upgraded version of the traditional single x-ray narrow/pencil beam XLCT design, in which the data acquisition time and reconstructed image quality are primarily determined by the collimated x-ray beam size and the number of angular projections. In this work, we have used four x-ray beams in our numerical simulation study and two x-ray beams in our experimental study. We believe these are enough to demonstrate our approach of multiple x-ray beam scanning in XLCT. In the future, if needed, we can further reduce the data acquisition time by using more x-ray beams. Certainly, there is an upper bound of the number of x-ray beams before we see the reconstructed XLCT image quality becomes compromised as shown in Fig. 2.18. For the numerical simulation cases with two and six targets, we have performed simulation studies with 8 and 16 x-ray beams as shown in Fig. 2.18. We believe there is a trade-off between the number of x-ray beams and the XLCT image quality, which deserves further investigations.

Although the measurement time of XLCT imaging is long, the x-ray beam size is small thus the accumulated x-ray dose in the object should be small, which was validated by our dose measurement experiment. Since the size of our ion chamber was large, we required a larger phantom in order to embed the chamber inside the phantom. In future studies, we plan to use a small ion chamber for more accurate measurement of the radiation dose in XLCT. Another point is that we could not find the *f-factor* to convert ion chamber

measurement to the dose measurement in tissues for the energy of 30 keV. We used the *f-factor* for the energy of 70 keV, which may cause slight errors. Considering above factors, we believe our dose measurement in XLCT, the first reported dose measurement, is qualitative and is in the range of a typical CT scan.

To reduce the measurement time of XLCT and the radiation dose, it is better to take measurements in less angular projections. As reported in [20], we can reconstruct XLCT image very well with measurements at two projections for sparse targets. We have validated this conclusion in our simulation of two target case. However, for complicated target case such as the six target case, two projections are not enough. We must use measurements from six projections to reconstruct good quality XLCT images.

As demonstrated in our numerical simulations and phantom experiment, the consideration of x-ray beam size and intensity changes in the XLCT reconstruction improves the image quality. And, as shown in Figs. 2.12 and 2.13, the two x-ray beam sizes were not the same. In the future, we must measure all the x-ray beam sizes for multiple-beam XLCT imaging.

In our numerical simulations, we used an x-ray beam with a diameter of 0.1 mm, which can be achieved in two ways. One is to use a superfine pinhole collimator as described in Section 2.1 where we achieved an x-ray beam with a diameter of 0.192 mm. Another way is to use an x-ray tube with a polycapillary focusing lens which will be described in the following section (Section 2.3). Our numerical simulations from Section 2.1.3 indicate that XLCT can have better spatial resolution with smaller x-ray beam size.

In summary, we proposed a multiple pinhole collimator based XLCT system design and introduced a multiple-beam scanning strategy which reduced the data acquisition time significantly. The feasibility of the multiple-beam scanning method has been validated by numerical simulations and phantom experiments. In the numerical simulation studies, the multiple deep targets have been reconstructed successfully at the correct locations with good shapes. In the phantom experiments, by using a two-pinhole collimator, compared with the traditional XLCT imaging, the total acquisition time was reduced by 50% without sacrificing the image quality. Two deeply embedded tiny targets have been reconstructed with very good accuracy in size and center-to-center distance. We have also measured the collimated x-ray beam size at different distance away from the collimator and included the changed beam size in the forward modeling and the reconstruction algorithms. We have measured the x-ray radiation dose during XLCT imaging and demonstrated that the dose is in the range of a typical CT scan.

2.3. XLCT Imaging Using a Focused X-ray Beam

One of the primary reasons that XLCT has not yet been adopted for use by the molecular imaging community is the long scanning time. CB-XLCT can reduce the imaging time, but at the cost of a degraded spatial resolution since the x-ray beam's size

and position can no longer be used as structural guidance in the XLCT reconstruction algorithm. There are several approaches for improving the scan time in NB-XLCT such as use of a higher flux x-ray tube, brighter contrast agents, simultaneous use of multiple x-ray beams (Section 2.2) and use of more sensitive optical detectors.

By using a higher flux x-ray tube for the collimated x-ray beam based XLCT imaging we can improve the scan time, but this method is still not efficient as most of the x-ay photons are absorbed by the collimator. Recently, x-ray optics have been studied to focus the x-ray beam to a fine focal spot and has been successfully used for XRF imaging [65]. Cong *et al.* first proposed a focused x-ray beam based XLCT imaging, where a 50-fold increase in photon intensity was obtained by delivering a focused x-ray beam with a focal diameter of 50 μm and demonstrated the feasibility of the concept with numerical simulations [66].

In this work, we report the first experimental demonstration of a polycapillary lens based XLCT imaging system and verified its feasibility with numerical and phantom experiments. To investigate the approach further, we performed a systematic study of the focused x-ray beam based XLCT. We present an experimental XLCT imaging system that uses a polycapillary lens to focus the x-ray beam, a single optical fiber bundle to collect the emitted optical photons, and a highly sensitive photomultiplier tube (PMT) to measure the optical signal, readout by a high-speed oscilloscope. The feasibility of the designed system was demonstrated through both numerical simulations and phantom experiments. To investigate effects of the x-ray lens on the x-ray energy, we measured the x-ray energy spectrum for the x-ray tube with and without the x-ray lens. In addition, we measured the radiation dose of this system, similar to our previous work in Section 2.2.5.

Previously, all currently reported XLCT systems have been equipped with EMCCD cameras to measure the emitted optical photons. With much higher sensitivity than the EMCCD camera, PMTs are preferred, especially for the detection of weak optical signals as in XLCT imaging. As a high gain device, PMTs have been widely used in traditional optical imaging. In this work, a PMT was used as the optical detector to achieve faster data acquisition.

2.3.1. Focused x-ray beam based XLCT imaging system design

The schematic of the proposed focused x-ray beam based XLCT imaging system is shown in Fig. 2.22. An x-ray tube (X-Beam Powerflux, XOS; Target metal: Molybdenum (Mo)) was used as the x-ray source to generate x-ray photons with a maximum energy of 50 kVp and a tube current of 1.0 mA. The output x-ray beam was focused by a 79.2 mm long polycapillary lens with an output focal distance of 45 mm, achieving a focal spot size of about 100 μm. The imaged object (e.g. phantom) was placed at the output focal distance (45 mm) and sat on an imaging stage mounted to manual lab jack (LJ750/M, Thorlabs) to adjust the x-ray beam scanning depth. This was mounted to a motorized rotation stage (B4872TS-ZR, Velmex, Inc.), which was mounted on a motorized linear stage

(MB2509Q1J-S3, Velmex, Inc.). The passed x-ray beam was detected by an x-ray detector (Shad-o-Box 1024, GOS scintillator screen, Rad-icon Imaging Corp.) and was used to measure the intensity of the focused x-ray beam and to detect the object boundary. Emitted optical photons were collected from the phantom side surface using a 2-meter-long optical fiber bundle with an aperture diameter of 3 mm. The fiber bundle head was position 2 mm from the phantom surface. The fiber bundle was fixed using a custom 3D printed holder that rotated with the phantom during measurements. A fan-cooled PMT (H7422P-50, Hamamatsu, Japan) driven by a high voltage source (C8137-02, Hamamatsu, Japan) measured the optical photons from the fiber bundle. The electronic signal from the PMT was further amplified by a broadband amplifier (SR445A, Stanford Research Systems, California) with a gain of 25. Then, a lowpass filter (BLP-10.7+, cutoff frequency 11 MHz, mini-circuits) was used to reduce the high-frequency noise. The amplified and filtered signal was finally acquired and displayed by a high-speed oscilloscope (MDO-3104, Tektronix, Oregon). The whole system except the PMT, the amplifier, and the oscilloscope was fixed on an optical bench and placed in an x-ray shielding and light-tight cabinet. All the devices were controlled by a lab-made program written with C++ in the Visual Studios development environment.

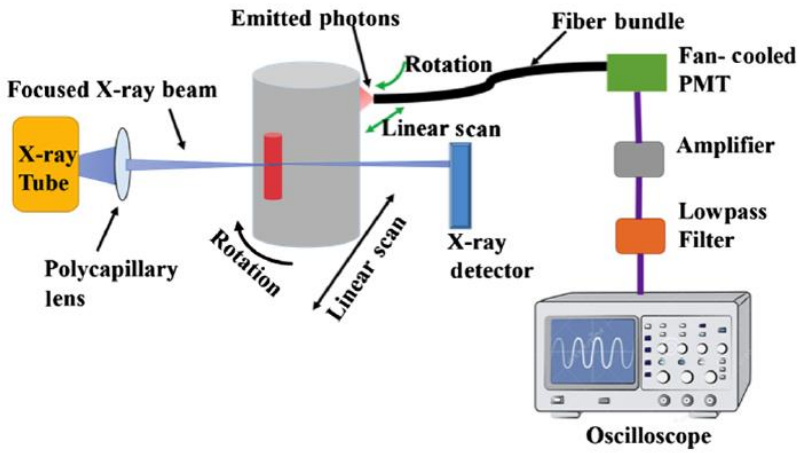

Figure 2.22. Schematic of the focused x-ray beam based XLCT imaging system.

2.3.2. Comparison of x-ray flux between a focused x-ray beam and collimated x-ray beam

In order to evaluate the improvement of x-ray flux obtained by using the polycapillary lens, we designed a comparison test between a focused x-ray beam and a collimated x-ray beam. We evaluate the x-ray flux by measuring the intensity of the emitted optical photons acquired by an EMCCD camera (C9100-3, Hamamatsu) from the top surface of a phantom embedded with a phosphor target while the x-ray beam excited the target. The schematic set-ups for this experiment are shown in Fig. 2.23. In this first set-up shown in Fig. 2.23(a), we used the X-Beam Powerflux x-ray tube, where a polycapillary lens was used to focus the x-ray beam to a spot of approximately 100 μm which excited

the target. The x-ray tube was set to operate at 50 kVp and 1 mA. In the second set-up shown in Fig. 2.23(b), we used the Neptune 5200 x-ray tube (Oxford Instruments, Target metal: Tungsten (W)). This tube was operated at 50 kVp and 2.0 mA. For both set-ups we used the same cylindrical phantom which was embedded with a 4.6 mm diameter cylindrical phosphor target (GOS:Eu^{3+}) at a concentration of 1 mg/mL. The EMCCD camera exposure time for the focused beam and collimated beam set-ups was 0.1s and 2s, respectively.

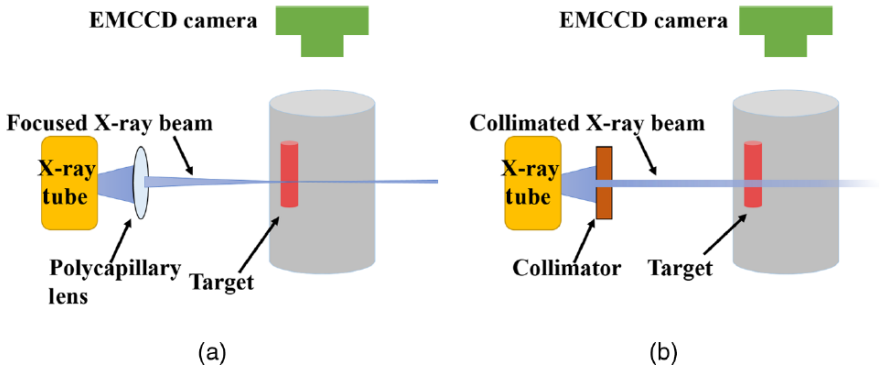

Figure 2.23. Schematic set-ups of the x-ray photon flux comparison between a focused x-ray beam (a) and a collimated x-ray beam (b)).

Since the polycapillary lens was permanently fixed to the X-Beam x-ray tube, we could not use the same tube in the comparison studies. Thus, to compensate for the different settings, we normalized the measurements obtained by the x-ray tube power, the x-ray beam diameter, and the EMCCD camera exposure time. After acquiring the top surface phantom images from the EMCCD camera, we subtracted a baseline background signal from the images, then the images were normalized as:

$$\begin{cases} N_{f_i} = f_i/(0.1\text{s})/(1\text{ mA} \times 50\text{ kVp})/(\pi \times 0.1 \times 0.1\text{ mm}^2) \\ N_{c_i} = c_i/(2\text{s})/(2\text{ mA} \times 50\text{ kVp})/(\pi \times 0.1 \times 1\text{ mm}^2) \end{cases} \text{for i} = 1, 2, \ldots, \text{M} \qquad (2.2)$$

where f_i and c_i are the measurements at the i'th pixel in the EMCCD camera images for the focused x-ray beam case and the collimated x-ray beam case, respectively. N_{f_i} and N_{c_i} represent the normalized pixel values of the corresponding images and M is the number of image pixels.

The ratio between the total intensity of the focused x-ray beam and total intensity of the collimated x-ray beam was calculated as:

$$\text{Ratio} = \sum_{i=1}^{M} N_{f_i} \div \sum_{i=1}^{M} N_{c_i} \qquad (2.3)$$

Figure 2.24(a) and Fig. 2.24(b) show the normalized images for the focused x-ray beam and collimated x-ray beam cases, respectively. The line profile plots along the green lines are plotted in Fig. 2.24(c). From Fig 2.24(a, b), we have found that the ratio of the maximum photon intensities between the focused beam and collimated beam cases were

as large as 2013. We also calculated the sum of the entire top surface for each image and found that the total intensity of the focused x-ray beam case was about 1200 times larger than that of the collimated beam case. Therefore, we can conclude that the focused x-ray beam can deliver 1200 times more x-ray photon density (x-ray photons per beam volume) than the collimated x-ray beam.

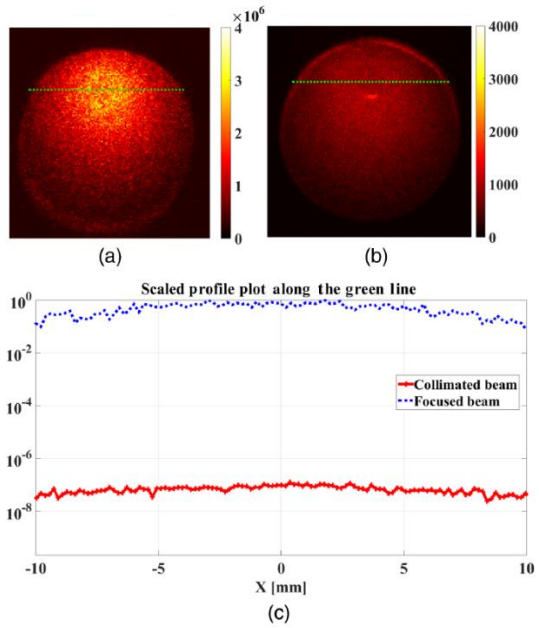

Figure 2.24. Normalized phantom top surface images acquired by the EMCCD camera (a) with the 0.1-mm focused x-ray beam and (b) with the 1-mm collimated x-ray beam. (c) Profile plots along the green lines in (a) and (b).

2.3.3. Energy spectra and beam size of the focused x-ray beam

To investigate how the x-ray lens affects the x-ray energy spectrum, we have measured the x-ray energy spectrum for the x-ray tube with the lens using a thermoelectrically cooled cadmium telluride (CdTe) detector (X-123 CdTe, Amptek Inc.) for the tube voltages of 30, 40, and 50 kVp, respectively. The x-ray detector module includes a preamplifier with pile-up rejection, a digital pulse processor, and a multichannel analyzer (PX4, Amptek Inc., Bedford, Massachusetts). The x-ray tube vendor (XOS, New York) measured the x-ray energy spectrum for the x-ray tube without the x-ray lens using a silicon drift detector (XR-100SDD, Amptek Inc.) for the tube voltages of 30, 40, and 50 kVp, respectively. For the energy spectrum measurement without the x-ray lens, the x-ray tube current was 0.3 mA and the exposure time was 100 s. Additionally, the detector used a pinhole of 0.5 mm and was 487 mm away from the x-ray tube. For the energy spectrum measurement with the x-ray lens, we also took measurements at the tube current of 0.3 mA and used 100 s of exposure time. The x-ray spectrometer (X-123 CdTe) used a 0.1-mm pinhole and was positioned 200 mm away from the lens.

Gafchromic EBT3 films were mounted on a linear stage to measure the size and intensity of the focused x-ray beam at different distances. The step size of the linear stage

was 3 mm with eight steps. We measured the x-ray beam size and intensity at a tube current of 0.25 mA and with varying tube voltages (20, 30, 40, and 50 kVp, respectively). The exposure time of the film for each linear step was 10 s. After being exposed, all the films were scanned by a high-resolution scanner (Epson Expression 11000XL). The intensity and the diameter of the focused x-ray beams were calculated from the pictures captured by the scanner by analyzing the exposed spot size and intensity.

The measured x-ray energy spectra for different tube voltages (30, 40, and 50 kVp) are plotted in Fig. 2.25(a) for the x-ray tube without the lens and Fig. 2.25(b) for the x-ray tube with the lens. The vertical axis indicates the photon count number recorded by the x-ray photon detectors. From both plots, we see there are two energy peaks at 17.5 and 19.5 keV corresponding to the characteristic x-ray photons of Mo. We also observed higher photon number ratio in the low-energy range when we used the x-ray lens, which is reasonable because low-energy x-ray photons are easier to be focused. To quantify the analysis, we have calculated the x-ray photon count ratio of the x-ray photons with energies less than the peak of 17.5 keV to all x-ray photon number for the 50 kVp case. The ratios were 58.7% and 70.2% for the x-ray tube without and with the lens, respectively. We found that the lens increased the low-energy x-ray photon ratio about 11.5%.

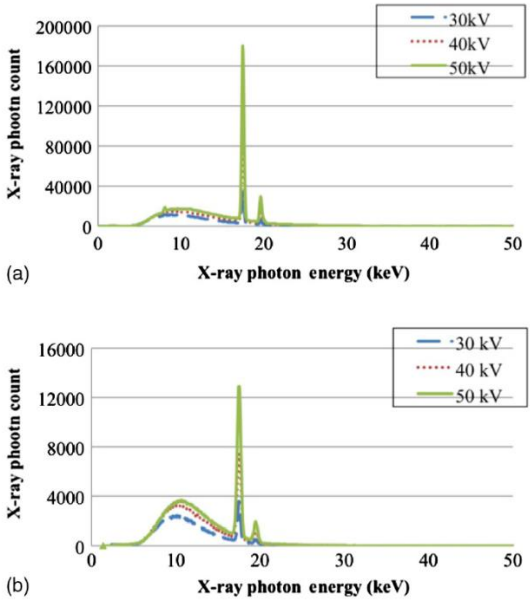

Figure 2.25. Measured x-ray photon energy spectra of the x-ray tube (a) without the lens and (b) with the lens for the x-ray tube voltages of 30, 40, and 50 kVp, respectively.

We measured the diameter and the intensity of the focused x-ray beam at different settings (x-ray tube voltage: 20, 30, 40, and 50 kVp; x-ray tube current: 0.25 mA). For simplicity, we only plotted the result measured when the x-ray tube voltage was 30 kVp, which is the same voltage to be used in the following experimental study. Figure 2.26 shows the raw film images [Fig. 2.26(a)], the measured x-ray beam diameter [Fig. 2.26(b)], the profile plots across the x-ray beam [Fig. 2.26(c)], the maximum x-ray intensity [Fig.

2.26(d)], and the averaged intensity [Fig. 2.26(e)] for the focused x-ray beam. The measured x-ray beam diameter demonstrates that the focused x-ray beams are dual-conical in shape and the beam diameter changes with distance. As seen in Fig. 2.26(b), the smallest x-ray beam diameter is 98 μm, slightly <100 μm, at the focal spot of 45 mm from the polycapillary lens. The intensity curves show that beyond the focal spot, the x-ray beam intensity attenuates exponentially. We observed that as the x-ray tube voltage increases, the x-ray beam diameter also increases. From Fig. 2.26, we see that the scanned object should be 45 mm away from the lens to have the smallest x-ray beam diameter.

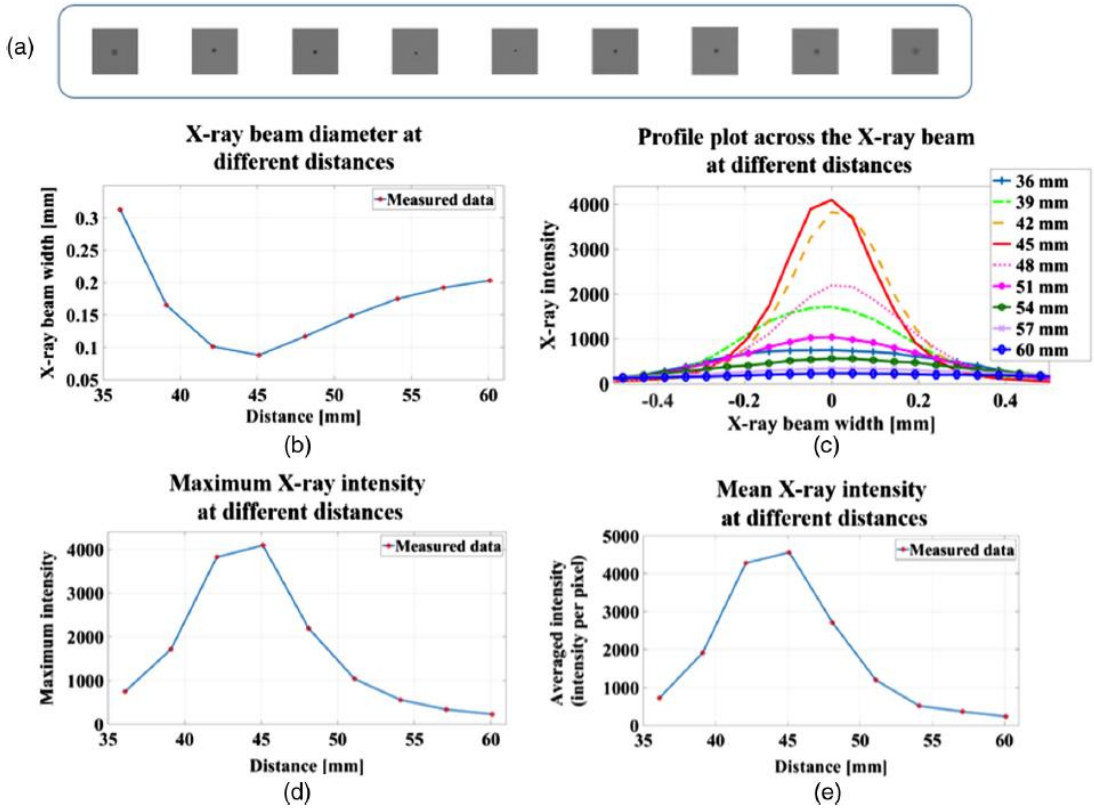

Figure 2.26. Measurement of focused x-ray beam diameter and intensity: (a) original film images obtained at different distances. (b) X-ray beam diameter at different distances from the polycapillary lens. (c) Profile plot across the x-ray beam at different distances. (d) Maximum x-ray intensity at different distances. (e) Mean x-ray intensity at different distances.

2.3.4. Measurement of radiation dose in focused x-ray beam based XLCT

We measured the radiation dose, using the same procedure as in Section 2.2.5. The set-up of the measurement is shown in Fig. 2.27. The x-ray dose was measured using an Accu-Dose system (Radcal, Monrovia, California) with a general purpose in-beam on chamber (10X6-6, Radcal). The active component of the ion chamber head has a diameter of 25 mm. The phantom was 44 mm in diameter and contained a central hole to fit the ion

chamber head and was composed of 1% Intralipid and 2% Agar. The phantom was placed on the rotary stage mounted on the linear stage. The ion chamber was fit into the phantom center. We then performed a scan that was the same as the scan in the following phantom experiment. We used 125 linear scan steps with a step size of 0.2 mm, six angular projections with an angular step size of 30 deg, and a measurement time of 1 s per linear scan step.

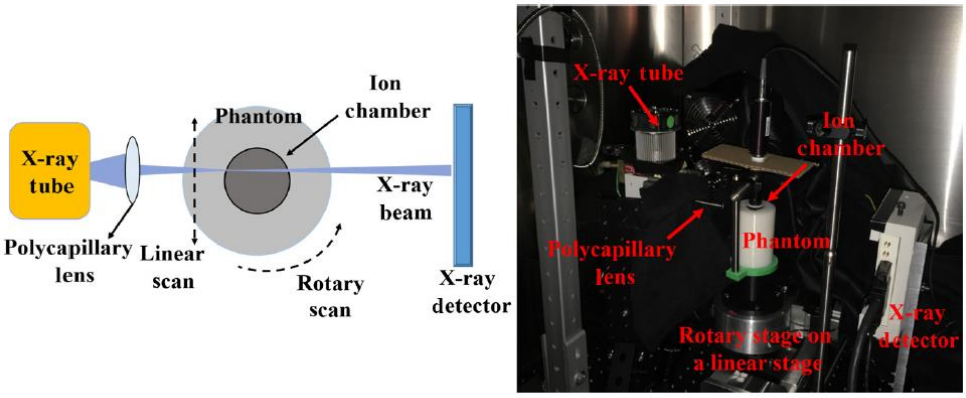

Figure 2.27. The schematic design and (b) a photo of the x-ray radiation dose measurement setup.

For the focused x-ray beam based XLCT imaging set-up, the total accumulated ionized x-ray radiation was 7.38 R. Using an *f-factor* of 0.93 rad/R (cGy/R), we calculated that the absorbed dose was 68.634 mSv or 6.8634 cGy.

2.3.5. Numerical simulations of focused x-ray beam based XLCT imaging

To validate our proposed focused x-ray beam-based XLCT design with measurements by optical fiber bundles, we have performed two numerical simulation cases both using a six-target phantom while taking measurements using one and six optical fiber bundles, respectively. For both simulation studies, we used a 10-mm long cylindrical phantom with a diameter of 12.8 mm. The optical properties of the phantom were set as μ_a = 0.0072 mm^{-1} and $\mu`_s$ = 0.72 mm^{-1}. X-ray attenuation coefficient was set as μ_x = 0.0214 mm^{-1}. We embedded the six targets with diameters of 0.2 mm and height of 6 mm inside the phantom as shown in Fig. 2.28 and the center-to-center distance was 0.4 mm. For both numerical simulations, the phosphor particle concentration was set to be 1 mg/mL with no phosphors in the background.

The optical fiber bundles were positioned 3 mm under the phantom top surface and the relative positions were fixed. During the simulation, the fiber bundles and phantom translated and rotated together. In the six fiber bundle case, the bundles were distributed evenly with an angular spacing of 30 degrees as shown in Fig. 2.28. For the case using a single fiber bundle, only fiber bundle #4 was used to collect the emitted optical photons. For both cases, the focused x-ray beam scanned the phantom at a depth of 5 mm. The

focused x-ray beam was set to have a focal spot of 100 μm and a linear scan step size was set to 100 μm as well. We acquired measurements from six angular projections using an angular step size of 30 degrees. The numerical measurements were generated from the forward model, in which the phantom was discretized by a finite-element mesh with 26,638 nodes, 153,053 tetrahedral elements, and 11,456 face elements. Finally, 10% Gaussian noise was added to the numerical measurements.

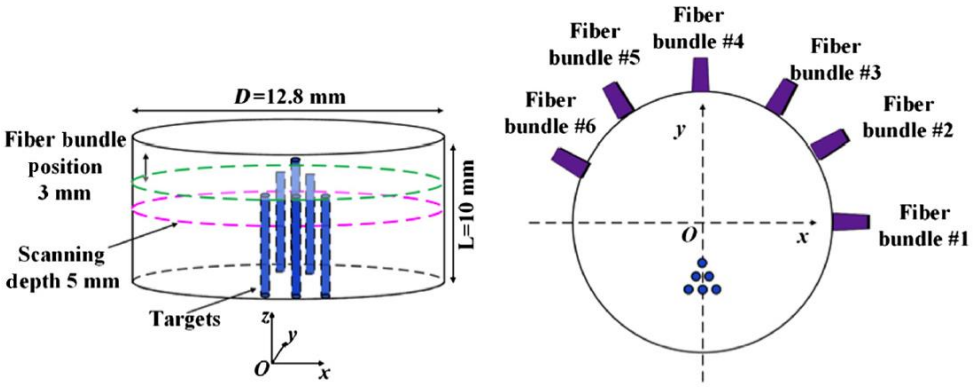

Figure 2.28. The phantom geometry and fiber bundle positions used for the numerical simulations.

In the focused x-ray beam XLCT, the shape of the focused x-ray beam was dual-conical. In this paper, we took the true beam shape into consideration. As described in the above section, we measured the focused x-ray beam size and intensity and found that the focused x-ray beam was dual-conical. The beam diameter changed linearly, and the beam intensity attenuated exponentially as the distance from the collimator increased. We set the focal distance of the x-ray lens to be 4.5 mm. The beam diameter at position $\vec{r}$ can be expressed as:

$$d(\vec{r}) = \begin{cases} 0.2 - \frac{L(\vec{r})}{45}, & L(\vec{r}) \leq 4.5 \\ \frac{L(\vec{r})}{45}, & L(\vec{r}) > 4.5 \end{cases} \tag{2.4}$$

where $L \in [0, 12.8]$ is the distance from one side of the phantom to other. We also adopted a normalized x-ray beam intensity, so the x-ray initial intensity at the entry to the phantom was set as $T_0 = 1$ which was used with Eq. 1.3.

The scanned transverse section was discretized onto a 2D grid with a pixel size of 25 μm^2 and the system matrix generated with the finite element mesh was interpolated onto the grid. For the reconstruction, we applied the L^1 regularized MM algorithm reconstruction framework to solve the optimization problem. Fig. 2.29 shows the reconstructed XLCT images for both cases. We can see that in both reconstructions, all six targets have been reconstructed successfully at the correct positions with acceptable shapes. We drew a normalized profile plot across the middle row targets and calculated the image quality metrics in Table 2.6. In terms of the TSE and CDE, the six fiber bundle case

performed better than the single fiber case. With a single fiber bundle, the image quality degraded only slightly, which shows that one fiber bundle may be sufficient for reconstructing a good XLCT image, though more fiber bundles will improve the overall reconstruction quality.

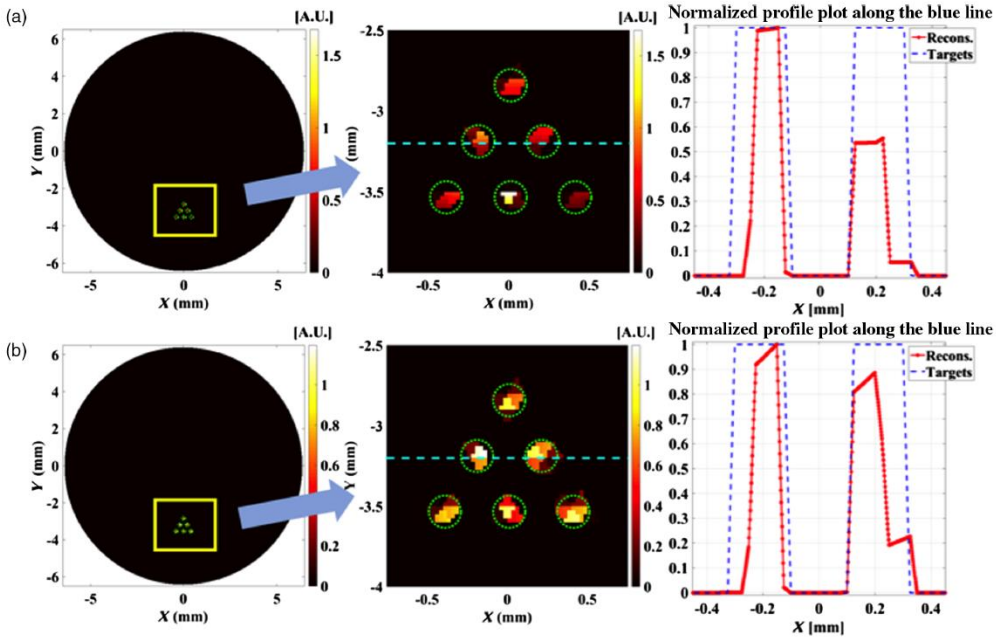

Figure 2.29. Reconstructed XLCT images, zoomed in regions and profile plots for numerical simulations with six targets. (a) Reconstructed results with data from one fiber bundle and (b) reconstructed results with data from six fiber bundles.

Table 2.6. Quantitative image quality metrics for numerical simulations of one and six fiber bundles.

Number of fiber bundles	Diameter (mm)/TSE	CtCD (mm)/CDE	DICE
1	0.1388/30.62%	0.3713/7.19%	47.1%
6	0.1844/7.8%	0.4156/3.9%	41.9%

The fiber bundle position may influence the XLCT imaging. To investigate how the fiber bundle position can affect the XLCT reconstruction, we performed additional numerical simulations. The settings of the simulations were the same as the single-fiber bundle case, except with different fiber bundle positions. We placed the fiber bundle at different angles (30 deg, 45 deg, 60 deg, 90 deg, 270 deg, 300 deg, 330 deg, and 360 deg) as shown in Fig. 2.30. The reconstructed images are shown in Fig. 2.31, from which we see that the reconstructed image results become better as the fiber bundle moved close to the six targets. The case with the fiber bundle at 270 deg has the best result. When the fiber bundle was at 90 deg (the furthest position from the targets), the reconstruction result is still acceptable with all six targets reconstructed successfully. In the previous simulation, we placed the fiber bundle at 90 deg in numerical simulations and 360 deg in the following phantom experiment. The bottom left target has barely been reconstructed when the fiber bundle was placed at 30 deg, 45 deg, or 60 deg. This is reasonable because multiple targets

were simultaneously excited, and we only had one detector with six angular projections. In the future, we can acquire measurements at more angular projections or more fiber bundles as detectors to overcome this issue.

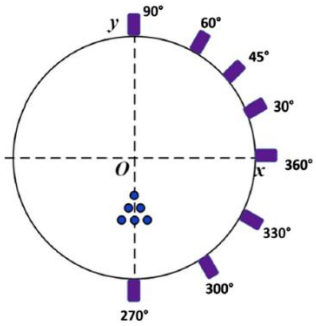

Figure 2.30. Phantom geometry and fiber bundle positions for the numerical simulation studies on the effect of fiber bundle position in XLCT imaging.

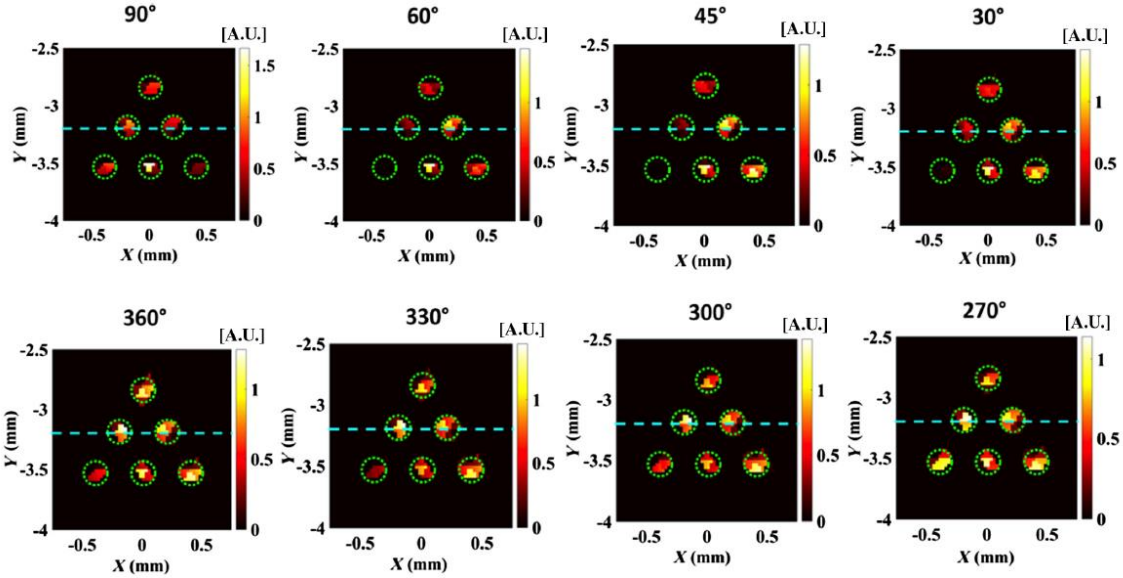

Figure 2.31. Reconstructed XLCT images for the numerical simulations with different fiber bundle positions. The angle indicates the single fiber bundle position.

2.3.6. Phantom experiments of focused x-ray beam based XLCT imaging

To validate our experimental set-up, we performed a phantom experiment with a solid cylindrical phantom as shown in Fig. 2.30. The background phantom was a 40 mm long and 25 mm diameter cylindrical phantom composed of 1% TiO_2 and 200 mL resin. For the targets, we used two glass capillary tubes (1000-800/12, Drummond Scientific), placed side by side as seen in Fig. 2.30(b), with an inner diameter of 0.4 mm and wall thickness of 0.2 mm. The tubes were filled with a solution of 1% intralipid, 2% agar, and 10 mg/mL of GOS:Eu^{3+} (UKL63/UF-R1, Phosphor Techn. Ltd.). We embedded the targets with center positions of (-0.4 mm, -6.5 mm) and (0.4 mm, -6.5 mm) from the phantom

center. During imaging, the x-ray detector was used to determine the phantom boundary for the beginning of the measurement through observing the x-ray intensity changes. The x-ray scan depth was 5 mm from the phantom top surface and we used a single optical fiber bundle, positioned 10 mm below the phantom top surface to collect the emitted optical photons from the side-surface as seen in Fig. 2.30(c, d). Measurements were taken from six angular projections using an angular step size of 30 degrees. To scan the entire phantom, we used 125 linear scan steps with a step size of 0.2 mm for each angular projection. For the data acquisition, the fan-cooled PMT was operated with a control voltage of 0.75 V and the amplifier has a gain of 25. For each linear scan position, the oscilloscope was set to acquire 1 s of measurements from the PMT. For this set-up, the current measurement time is 6 projections×125 steps×1 second or 12.5 minutes. During imaging, the x-ray tube was operated at 30 kVp and 0.5 mA.

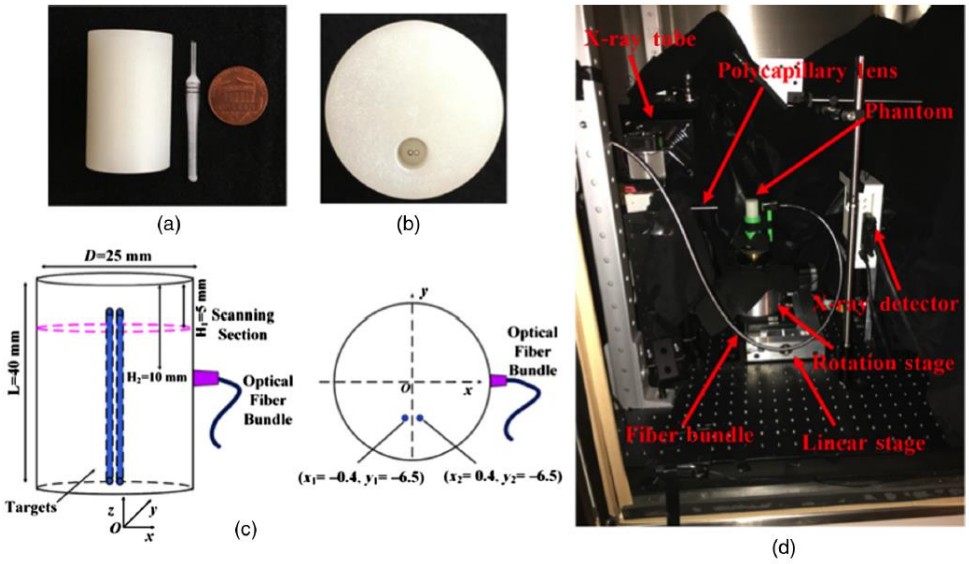

Figure 2.32. (a) White light picture showing the side view of the solid phantom (left), the targets (middle), and a penny (right) as reference. (b) Top view of the solid phantom, where two capillary tubes as targets were placed inside the hole of the solid phantom. (c) The phantom geometry used for the experiment, where two capillary tubes are the targets. (d) The focused x-ray beam-based XLCT system setup.

In the XLCT reconstruction for the phantom experiment, we also used the L^1 regularized MM algorithm and the same finite-element mesh was used. The reconstructed transverse section was discretized with a 2D grid with a pixel size of 50 μm^2 and the measured x-ray beam size models were applied in the reconstruction. Figure 2.33 shows the results from the phantom experiment. Fig. 2.33(b) shows the reconstructed XLCT image and Fig. 2.33(c) shows the zoomed-in target region, indicated by the green box in (b) where the true target size and position is represented by the green circle, determined from the microCT image (Fig. 2.33(a)). From the reconstructed image, we can see that both targets have been reconstructed successfully and clearly resolved, as indicated by the normalized line-profile plot in Fig. 2.33(d). The quantitative image evaluation metrics for the reconstruction is also listed in Table 2.7. From the full width half maximum (FWHM),

the reconstructed target size was 0.45 mm with an error 0f 12.5%. In addition, the CtCD is 0.75 mm with an error of 6.25%. Lastly, the DICE was calculated as 80%. Based on these results, we can conclude that multiple targets can be successfully reconstructed using our proposed focused x-ray beam based XLCT imaging system.

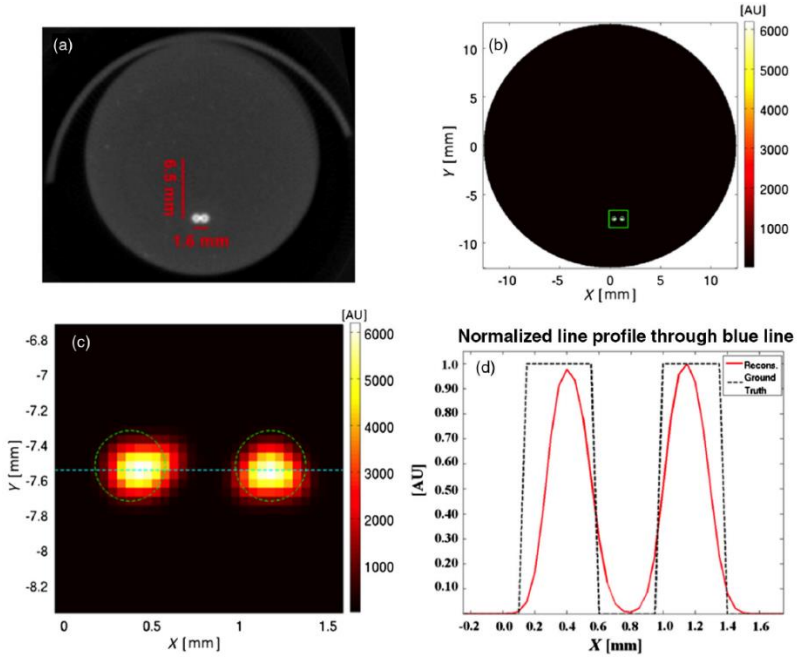

Figure 2.33. (a) A transverse section from the reconstructed microCT image of the phantom with two targets, (b) reconstructed XLCT image, (c) the zoomed in image of the reconstructed image, and (d) the profile plot across the two targets. The green square in (b) indicates the zoomed in region. The green circle in (c) indicates the exact target size and position. The blue dotted line in (c) indicates the profile location.

Table 2.7. Quantitative image quality metrics for the phantom experiment with two-targets.

Diameter (mm)/TSE	CtCD (mm)/CDE	DICE
0.45/12.5%	0.75/6.25%	80.0%

2.3.7. Discussion and conclusions

In this work, for the first time, we have used a polycapillary lens to focus the output x-ray beam for higher photon flux and applied the focused x-ray beam for XLCT imaging. We have generated an x-ray beam with a diameter as small as 98 μm at the focal spot of the lens. Comparing the photon flux between the focused x-ray beam and the collimated (1 mm diameter) x-ray beam, we found 1200 times increase in photon flux density increase with the focused x-ray beam. In our previous work in Section 2.1, it took 130 minutes to scan a 12.8 mm diameter phantom using the superfine collimated x-ray beam with a diameter of 0.175 mm. In this study, it took only 12.5 minutes to scan a 25 mm diameter phantom using the focused x-ray beam. Due to the improvement in photon flux density, we can dramatically reduce the required scan time for XLCT imaging. From Fig. 2.24, we can see that with a 0.1s exposure time for the focused x-ray beam (Fig. 2.24(a)), we have a

much brighter signal than using 2s exposure with the 1 mm diameter collimated x-ray beam (Fig. 2.24(b)). In future studies, we plan to purse a continuous scan mode using a PMT based detection set-up where we anticipate a single angular projection scan can be completed in less than 10 seconds, which will allow for a six-projection XLCT scan to be performed in under 1 minute.

Though a single PMT can only measure the optical density at one spot, our numerical simulations and phantom experiment demonstrated that sparse sampling with a single optical fiber bundle is sufficient to reconstruct complex targets embedded deeply in turbid media. In our simulations, we also showed that more measurements from more fiber bundles can improve the image quality, thus in the future, we plan to incorporate more fiber bundles and PMTs to achieve better XLCT images.

One concern is that most of the x-ray photons in the focused x-ray beam are within the range of 15-20 keV as shown in Fig. 2.25, which means that that the focused x-ray beam may not penetrate large objects. We performed attenuation measurements and found that there is a sufficient number of x-ray photons that can pass through a 2 cm slab of turbid media, which implies that our focused x-ray beam is appropriate for imaging mouse sized objects.

It would also be ideal if we could count the number of x-ray photons directly. Gafchromic EBT3 films might be possible to achieve this, only if the x-ray photons have the same energy, which is not the case here. Here we simply used an EMCCD camera to compare the intensity on the top surface of the phantom when the same target is excited by the x-ray beams. The luminescence intensity is proportional to the x-ray photon number if the photons have the same energies. We found the luminescence intensity from the 0.1 mm focused x-ray beam was 12 times larger than the 1.0 mm collimated x-ray beam. Considering the 10 times difference in beam diameters (or 100 times difference in the beam area), we estimate that the x-ray flux in the focused beam is 1200 times larger than the collimated beam. Of note, the collimated x-ray beams were generated using a tungsten target, which has much higher energy peaks than molybdenum which was used in the focused x-ray beam.

According to [67], CT scans with a dose of 194.3 mSv are unlikely to cause any radiation damage to mice. It was also reported that a single lethal radiation dose to mice is 26,800 mSv [67, 68]. Although the measured x-ray dose in this study measured as 68.634 mSv, far below the lethal dose, it is 46 times larger than reported in Section 2.2.5. This is reasonable because the focused x-ray beam has a much greater x-ray photon flux, which means a greater radiation dose per time. To mitigate the radiation dose, we can utilize a continuous scan mode and if we achieve a scan time of 2 minutes, for example, the radiation dose would be reduced approximately 11 mSv.

Another challenge we faced is to find the initial and final x-ray beam positions corresponding to the actual starting and ending points for each angular projection. The x-

ray detector can be used to detect the changes in x-ray beam intensity, but this is not always obvious to determine, which can lead to potential errors in XLCT data mapping. In future systems, we plan to rotate the x-ray beam instead of the object, which means the field-of-view will be fixed.

In the phantom experiments, we set the linear scanning step size to be 200 μm, which is equal to the average dual-cone diameter. For the numerical simulations we used a step size of 100 μm, close to the focal point diameter. For both cases, we can reconstruct the targets well, which indicates that the linear scanning step size can be larger than the smallest x-ray beam diameter.

In summary, in this work we have built a focused x-ray beam based XLCT imaging system for the first time. We can perform sparse sampling using only a single optical fiber bundle and PMT. We also found a large increase (1200 times) in the x-ray photon flux density compared to the collimated x-ray beam. Both the numerical simulations and phantom experiments performed have demonstrated the feasibility of the proposed XLCT imaging system.

Acknowledgment: I would like to thank Dr. Wei Zhang (Postdoctoral Scholar in Dr. Li's lab at the time during these works). He built both the superfine pinhole and multiple-pinhole collimator based XLCT imaging systems and I have assisted him with the build of the focused x-ray beam based XLCT imaging system. I have assisted with and taken many of the experimental measurements and analyzed the data in these works.

CHAPTER 3

SENSITIVITY OF XLCT IMAGING

3.1. Sensitivity Study of XLCT Imaging

Previous studies with XLCT imaging have demonstrated that the method can obtain high resolution and high sensitivity simultaneously. In particular, in terms of the sensitivity, it was previously determined that the minimum detectable concentration was subpicomolar for superficial targets [19, 69]. In addition, XLCT has been demonstrated through numerical simulations in [46] to be able to image a 4.8 mm diameter and 1 mg/mL (27.6 mM) concentration GOS:Eu^{3+} target and experimentally up to a scanning depth of 7.7 mm in [20]. These studies have shown the potentials of XLCT as a useful molecular imaging modality. However, so far there is no study on XLCT's sensitivity of imaging x-ray excitable phosphor targets in deep turbid media.

For small-animal imaging studies, high-resolution (microscopic) x-ray computed tomography (microCT) systems have been developed and widely used to study models of human disease [70, 71]. These systems are capable of providing the necessary resolving abilities required for small-animal research at generally a low-cost, and thus remain popular. However, since microCT systems operate under the same principles as conventional CT systems, they also suffer from the same limitations, including the lack of sensitivity for contrast agents. It should be noted, that for XLCT, with the addition of an x-ray detector to detect the traversed x-ray beam, it is possible to obtain anatomical images simultaneously with the x-ray luminescence; thus, XLCT and CT are inherently co-registered.

To the best of our knowledge, there is no comparison study between CT and XLCT in imaging nanophosphor targets in deep turbid media. In this study, we compared the sensitivity of two imaging modalities, XLCT and microCT, by performing phantom experiments to demonstrate the enhancement in sensitivity obtained from XLCT imaging than from microCT alone. Although most XLCT systems are designed with the ability to perform microCT imaging as well (since XLCT is multimodal), we performed the CT scan with our dedicated microCT system.

3.1.1. Experimental set-up for XLCT and microCT imaging

In this study, we used the same imaging system described in Section 2.1.2, with the addition of a manual lab jack that allowed us to adjust the x-ray scanning depth. A schematic and image of the imaging system is shown in Fig. 3.1 and Fig. 3.2, respectively.

In short, an x-ray tube (Neptune 5200, Oxford Instruments) generated x-ray photons with a maximum power of 100 W (50 kVp and 2.0 mA) which were then collimated with a lab-made collimator to provide a 1 mm diameter pencil beam. The phantom was placed approximately 50 mm away from the x-ray source on top of the manual lab jack (LJ750/M, Thorlabs) that allowed us to vary the x-ray beam scanning depth from 6 to 23 mm. The lab jack was fixed on top of a motorized rotary stage (B4872TS-ZR, Velmex Inc.) that was then fixed on a motorized linear stage (Unislide MA40, Velmex Inc.). The x-ray beam was detected by an x-ray detector (Shad-o-box 1024, Rad-Icon Imag. Corp.) fixed opposite of the x-ray source. A small portion of the emitted luminescent signal (photons) from the target propagated to the phantom top surface and were reflected by a flat mirror to be detected by a water-cooled EMCCD camera (C9100-13, Hamamatsu). The entire XLCT imaging system was fixed on an optical bench inside of a light-tight and x-ray shielding cabinet and was controlled by programs on a lab computer.

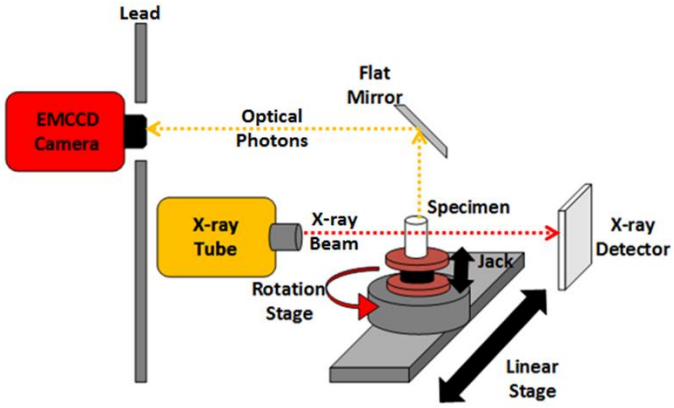

Figure 3.1. Schematic of the XLCT imaging system.

A photograph of the microCT imaging system is shown in Fig. 3.3. The x-ray tube (Jupiter 5000, Oxford Instruments) generated x-ray photons with a maximum power of 50 W (50 kVp and 1.0 mA) and the output x-ray beam was filtered by 0.4 mm of aluminum. The transmitted x-ray photons were detected by an x-ray detector (Shad-o-Box 1024, Rad-Icon Imag. Corp). Both the x-ray tube and detector were fixed to a rotational gantry that rotated from 0 to 360 degrees during imaging to provide images at different angular projection angles. Between the x-ray source and detector, the sample to be imaged was placed on a sample stage, which was moved into the FOV of the x-ray detector by a motorized linear stage (Unislide MA25, Velmex Inc.). The entire system was fixed to an optical table inside of an x-ray shielding cabinet and was programmed and controlled by a lab computer. We used a cylindrical plastic phantom embedded with small metal balls to calculate system parameters of the microCT system, such as the source to detector and source to isocenter distances following approaches in [72].

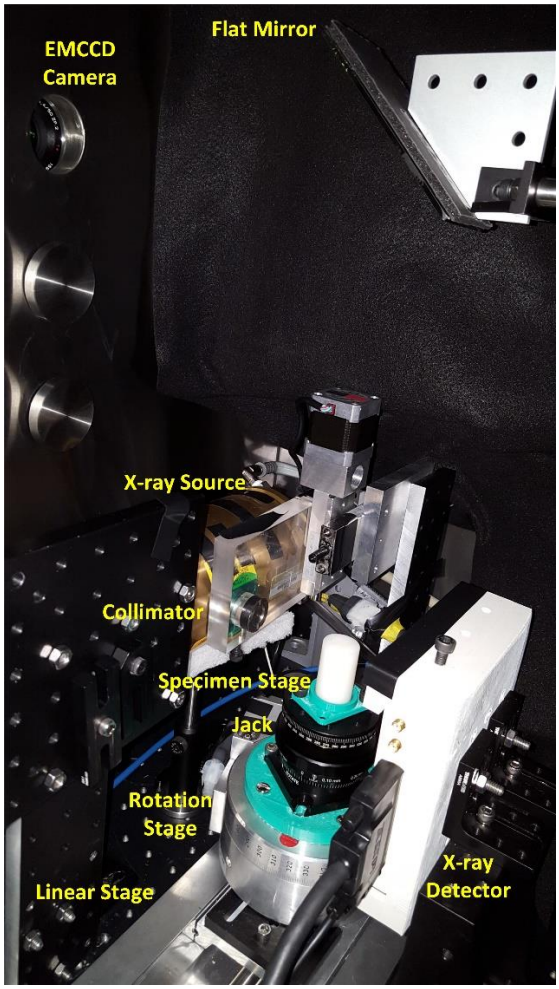

Figure 3.2. Photograph of the XLCT imaging system set-up.

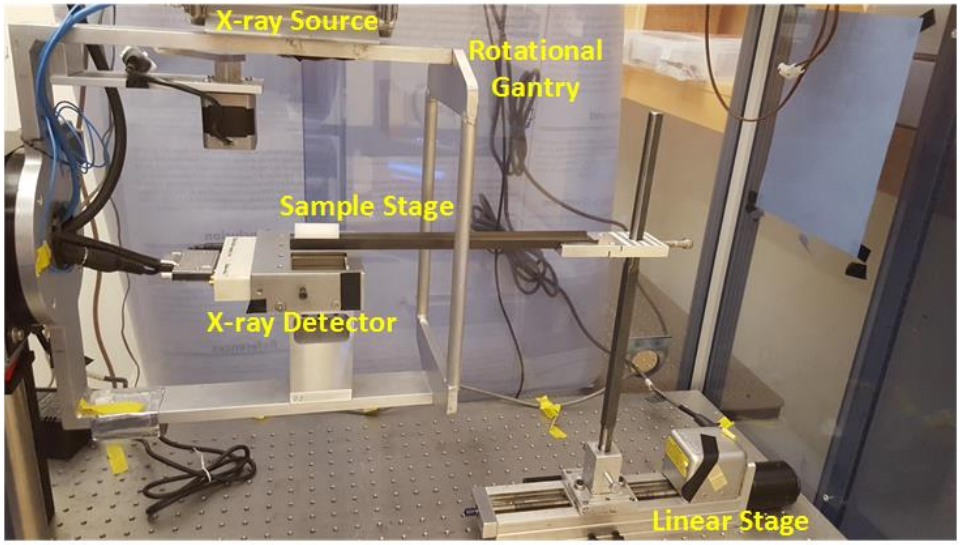

Figure 3.3. Photograph of the microCT imaging system set-up.

3.1.2. Phantom fabrication and experimental scanning schemes

To evaluate the sensitivity of XLCT, we performed a set of cylindrical phantom experiments with four different phantoms, each containing a cylindrical target. The geometry of the phantom with its target is shown in Fig. 3.4. The cylindrical phantoms were 40 mm long and 25 mm in diameter and were composed of 1% intralipid and 2% agar containing a 4.60 mm off-center through-hole to embed the target as shown in Fig. 3.4(b). The background contained no GOS particles. The cylindrical target had a diameter of 4.60 mm and a length of 35 mm and was composed of 1% intralipid, 2% agar, and the GOS:Eu^{3+} phosphor particles. The target was inserted into the through-hole and then the remaining 5 mm was capped off with background material. For the four different experimental cases, the targets had a GOS concentration of 27.6 mM, 2.76 mM, 276 µM, and 27.6 µM, or 10, 1.0, 0.1, and 0.01 mg/mL, respectively. The optical properties of the phantom were estimated to have the absorption coefficient (μ_a) of 0.0072 mm^{-1} and the reduced scattering coefficient ($\mu`_s$) of 1.0 mm^{-1} at the wavelength of 703 nm, corresponding to the highest emission peak for GOS:Eu^{3+}.

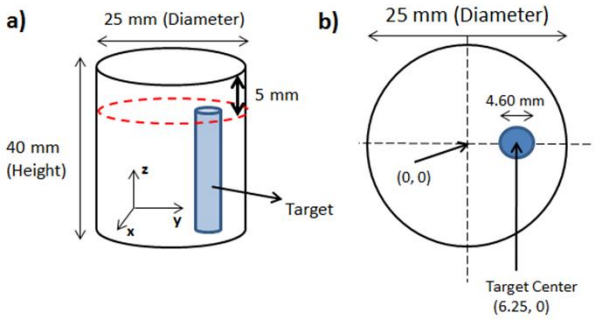

Figure 3.4. Phantom geometry used in the experimental study. (a) Overall phantom geometry; (b) Top-surface geometry.

To study the effects of optical absorbers such as ink on the sensitivity of XLCT, we also created a second set of phantoms, this time adding India ink as an absorber. These phantoms were estimated to have optical properties of μ_a = 0.0072 mm^{-1} and $\mu`_s$ = 1.0 mm^{-1} at the wavelength of 703 nm, which is close to the optical properties of tissue.

All the cylindrical XLCT phantoms were fabricated following the procedure used in [73]. Briefly, the solution of agar and water were heated up to 95.0°C to dissolve the agar. The intralipid (and GOS:Eu^{3+} for the target solution) was then added into the solution at 60°C (50°C for the GOS:Eu^{3+}). Then, the liquid solution was placed into a mold and allowed to solidify at room temperature.

For all XLCT measurements, the EMCCD camera was operated at -92.50°C with an EM Gain and an analog gain of 255 and 5, respectively. The x-ray tube output was set to maximum (50 kVp, 2.0 mA, or 100 W) for all experiments as well. We took

measurements from 6 angular projections with an angular step size of 30°. Since the diameter of the phantom was 25 mm, based on the size of the x-ray beam (1 mm), 25 linear steps were used to scan the entire phantom for each angular projection. For each linear step, one x-ray luminescence image was acquired from the phantom top surface. The EMCCD camera exposure time used for all cases is given in Table 3.1. The x-ray detector was used to determine the phantom boundary (start location for scanning). For each of the phantoms without India ink, to test the depth capabilities of XLCT for imaging, we took measurements at 4 different scanning depths (6, 11, 16, and 21 mm), which is the distance from the top surface of the phantom. For the phantoms with India ink, we only performed a single scan for each concentration at a scanning depth of 11 mm, which is close to the typical radius (or depth) of a mice torso. The XLCT images were reconstructed using our forward model described in Section 1.3.4 and the L^1 regularized MM reconstruction framework. Only the scanned transverse sections of the phantoms were reconstructed which was discretized using a 2D grid with a pixel size of 200 μm^2 and the sensitivity matrix was interpolated onto the grid.

Table 3.1. XLCT imaging EMCCD camera exposure times.

Target Conc.	Scan Depth (mm)	Exposure Time (s)
No Ink		
	6	0.080
27.6 mM	11	0.300
(10 mg/mL)	16	0.500
	21	2.000
	6	0.080
2.76 mM	11	1.000
(1.0 mg/mL)	16	2.000
	21	5.000
	6	0.500
276 μM	11	2.000
(0.1 mg/mL)	16	4.000
	21	5.000
	6	1.000
27.6 μM	11	5.000
(0.01 mg/mL)	16	8.000
	21	10.000
Ink Phantoms		
27.6 mM	11	0.080
2.76 mM	11	0.500
276 μM	11	1.000
27.6 μM	11	3.000

To compare the sensitivity of XLCT to that of microCT, immediately after the XLCT data acquisition, each phantom was placed into our microCT system to perform a full CT scan. The x-ray tube output was set to 50 kVp and 0.33 mA (16.5 W) to avoid x-ray detector saturation. For the microCT scan, 180 projections with an angular step size of

2° were used and the x-ray detector exposure time was set to 500 ms. The microCT image reconstruction was performed using a filtered-back-projection (FBP) algorithm with a Shepp-Logan filter.

3.1.3. XLCT measurements and reconstructed images

Before the XLCT image reconstruction, we analyzed the XLCT measurements on the top surface of the phantom to examine how the measurements changed for different target concentrations and different scanning depths. We captured the top surface optical signal from a single projection during which the target was closest to the x-ray source and the x-ray beam traversed the center of the target of concentration 2.76 mM (1.0 mg/mL), using an EMCCD camera exposure time of 500 ms for all cases for four different scan depths (6, 11, 16, and 21 mm). The raw measurements pictures are shown in Fig. 3.5 where the dotted green circle indicates the top surface boundary. The pictures in the top row (Fig. 3.5(a)) are plotted with the same color bar for comparison and the pictures in the bottom row (Fig. 3.5(b)) are plotted with their own color bar for better view. Fig. 3.5 indicates that there are sufficient optical photons that reach the top surface for the XLCT reconstruction for a target as deep as 21 mm. In Fig. 3.6(a), the measurements from the first angular projection of the phantom embedded with a 27.6 μM (0.01 mg/mL) GOS:Eu^{3+} target are plotted. At each linear scan position (x-axis), the total intensity in the EMCCD camera image is summed up (y-axis). In Fig. 6b, the EMCCD camera images for positions 9 (left) and 14 (right) are shown to demonstrate the difference in the signal acquired while the x-ray beam excited the GOS:Eu^{3+} target (right) and while the x-ray beam did not (left). When the x-ray beam traversed the target, the measured optical signal had good contrast to the background as seen in the right image. When the x-ray beam did not excite the target and went through the background phantom, there were almost no measured signals and no contrast as seen in the left image.

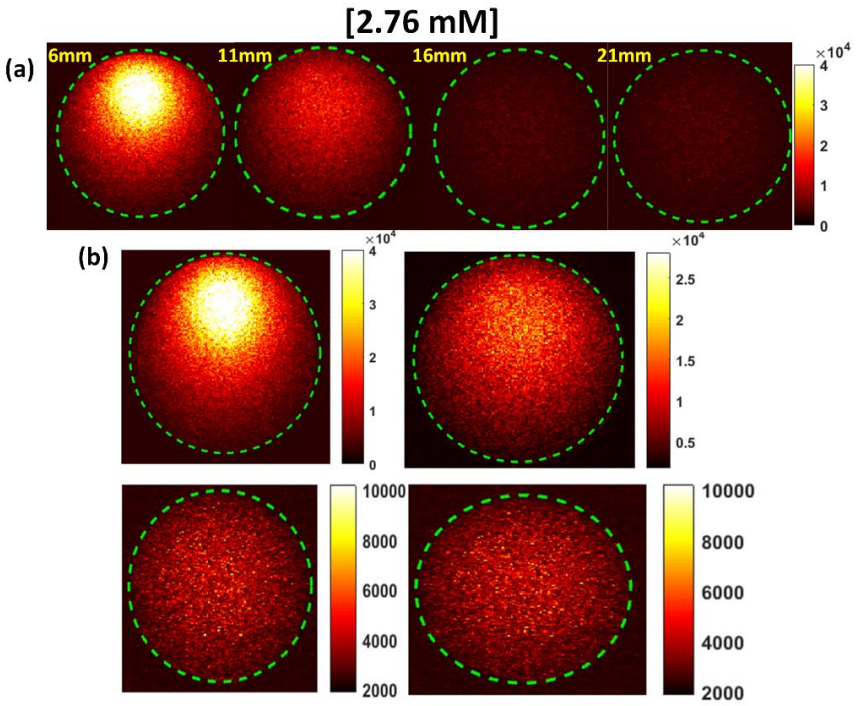

Figure 3.5. Top surface EMCCD camera image for the phantom embedded with a 2.76 mM (1.0 mg/mL) GOS:Eu^{3+} target under x-ray excitation at varying scanning depths. (a) All images shown with the same color bar. (b) Each image with its own adjusted color bar for better view.

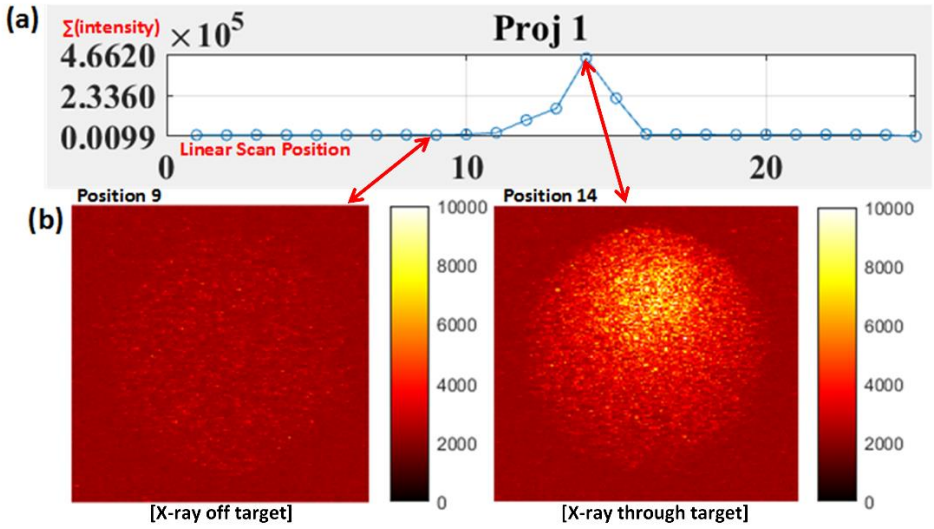

Figure 3.6. Measurements from the phantom embedded with a 27.6 µM (0.01 mg/mL) GOS:Eu^{3+} target under x-ray excitation at a scan depth of 6 mm. (a) Plot of measurements at each linear scan position for a typical angular projection. (b) Actual EMCCD camera images for positions 9 (left) where the target was not excited by the x-ray and for position 14 (right) where the x-ray beam passed through the target. Images are plotted with the same color bar.

Fig. 3.7 shows the XLCT reconstructed images for the phantoms without India ink for varying concentrations (27.6 mM, 2.76 mM, 276 µM, and 27.6 µM) and x-ray scanning depths (6, 11, 16, 21 mm). Four different columns in Fig. 3.7 show the reconstructed XLCT

images from four different target concentrations with the leftmost column indicating the highest concentration (27.6 mM). The four rows in Fig. 3.7 represent the reconstructed XLCT images for four different scan depths with the bottom row indicating the maximum depth used (21 mm). Each reconstructed image in Fig. 3.7 is plotted with its own color bar that indicates the reconstructed phosphor concentration. We have also normalized the XLCT reconstructed images by their own EMCCD camera exposure time (Table 3.1) so that the effects of exposure can be minimized. Fig. 3.8 shows the zoomed-in target region for each case (same image arrangement as Fig. 3.7). The green circle indicates the true target's location in both Figs. 3.7 and 3.8. From the reconstructed images alone, it is quite clear the target was reconstructed successfully in the correct location for all the scan depths and target concentrations. Table 3.2 shows the evaluated image quality metrics for each case. In nearly all cases the DICE was around 90%, indicating a high similarity between the reconstructed target and true target, except for 27.6 μM at the depth of 21 mm which had a DICE of 54.286%. In addition, for each concentration (except for 27.6 μM), the TSE was at most 4.35%, indicating that across the 4 scanning depths, the reconstructed target size varied by less than the 4.35%.

In Fig. 3.9, the reconstructed target size (normalized to the actual size), is plotted against the scan depth for the four different target concentration cases. Ideally, the value should stay at 1.0 across all the scanning depths. As indicated by Fig. 3.9, the reconstructed target size changes by less than 4.35% for all four concentrations at four different scanning depths, except for the worst-case scenario of 27.6 μM at 21 mm depth. For this case, the DICE was lowest (54.286%) and the TSE was the greatest (43.48%). The increase in TSE and lower DICE can be attributed to the low and noisy signal obtained from such a low concentration at a significant depth. Lastly in Fig. 3.10, the average reconstructed values inside the target region for each concentration at each scan depth were plotted. For better view, the values are plotted in logarithmic scale (base 10). From the plot, we can see that the higher concentration targets were always reconstructed with higher values than the lesser concentrations. In addition, for the depths up to 16 mm, which is sufficient for mice imaging, we have calculated the standard deviation between the reconstructed average values to be 26%, 31%, 31%, and 28% for the 27.6 mM, 2.76 mM, 276 μM, and 27.6 μM concentrations respectively. This indicates that across the scanning depths, the average reconstructed values only differed by about 30% on average. From the average reconstructed values, we also calculated the ratio between them to be approximately 349.5:40.7:9.2:1.0. Between the two highest concentrations (27.6 mM and 2.76 mM) and the two smallest concentrations (276 μM and 27.6 μM) we have about a 9:1 ratio in the average reconstructed values. Between the 2.76 mM and 276 μM concentrations, we only had about a 4.5:1 ratio difference, which was smaller than expected.

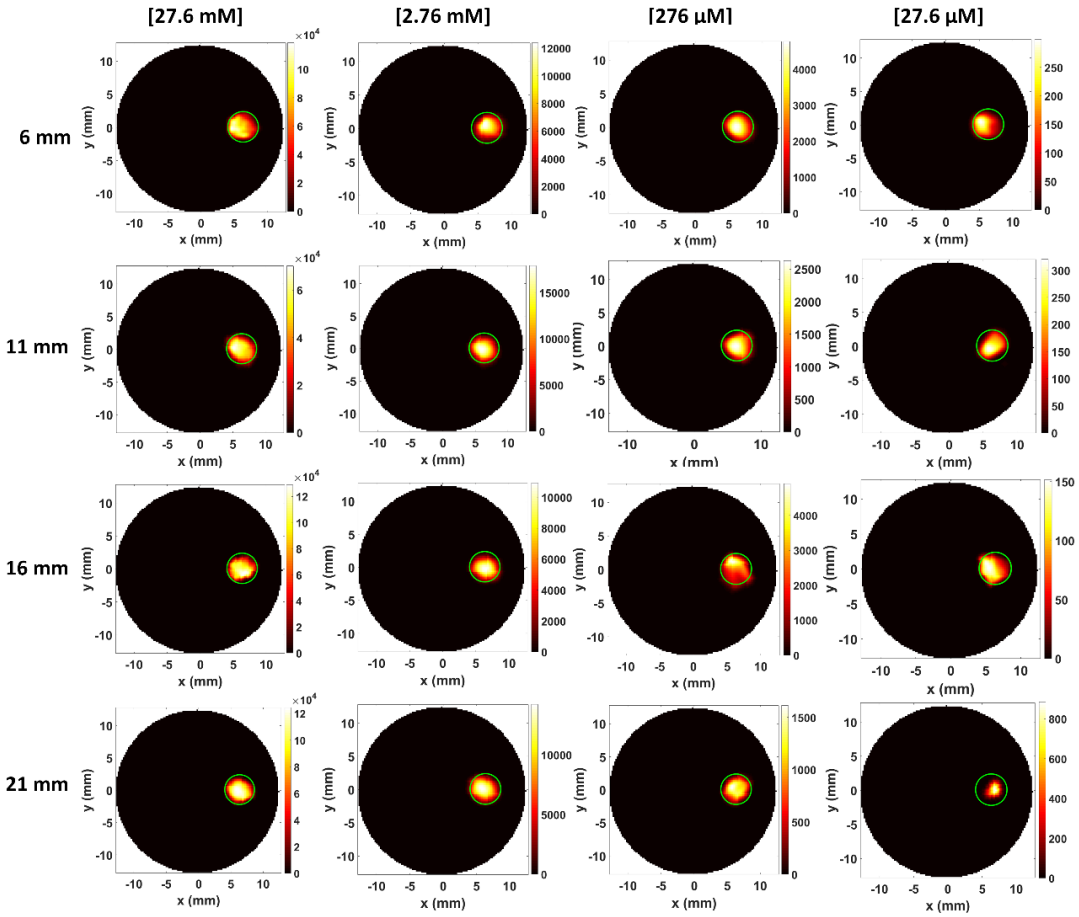

Figure 3.7. XLCT reconstructed images for different GOS:Eu^{3+} target concentrations at different scanning depths. The green circle depicts the true target location.

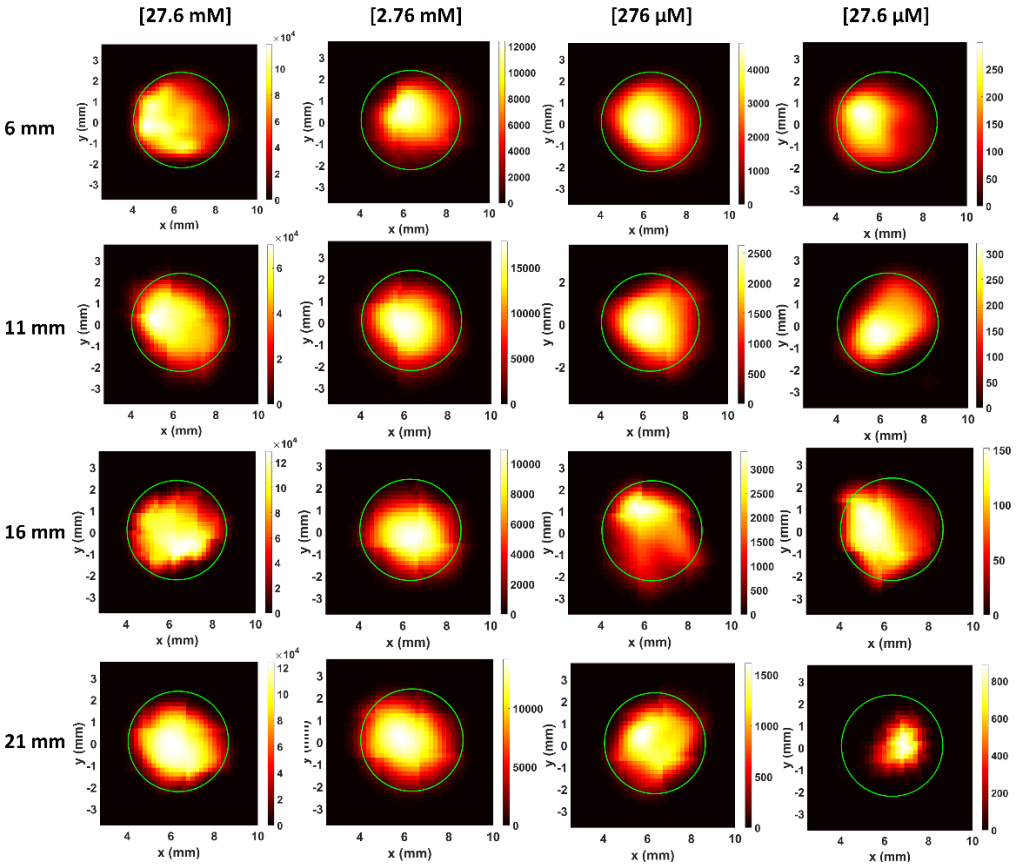

Figure 3.8. The zoomed-in target region for XLCT reconstructed images in shown in Fig. 3.7.

Table 3.2. XLCT image quality metrics (Phantoms with no India ink)

Target Conc.	Scan Depth (mm)	Diameter (mm)/TSE (%)	DICE (%)
27.6 mM (10 mg/mL)	6	4.800/4.35	94.002
	11	4.600/0	90.972
	16	4.600/0	91.579
	21	4.600/0	92.664
2.76 mM (1.0 mg/mL)	6	4.800/4.35	89.975
	11	4.800/4.35	90.361
	16	4.800/4.35	90.037
	21	4.800/4.35	91.558
276 µM (0.1 mg/mL)	6	4.800/4.35	93.141
	11	4.600/0	87.383
	16	4.600/0	88.426
	21	4.400/4.35	91.919
27.6 µM (0.01 mg/mL)	6	4.600/0	87.671
	11	4.400/4.35	87.548
	16	4.600/0	88.674
	21	2.600/43.48	54.286

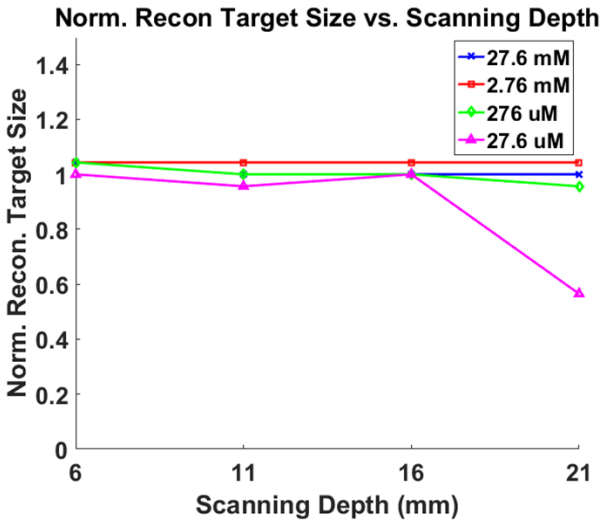

Figure 3.9. Plot of normalized XLCT reconstructed target size versus the x-ray beam scanning depth for the non-ink phantoms containing four varying GOS:Eu^{3+} target concentrations.

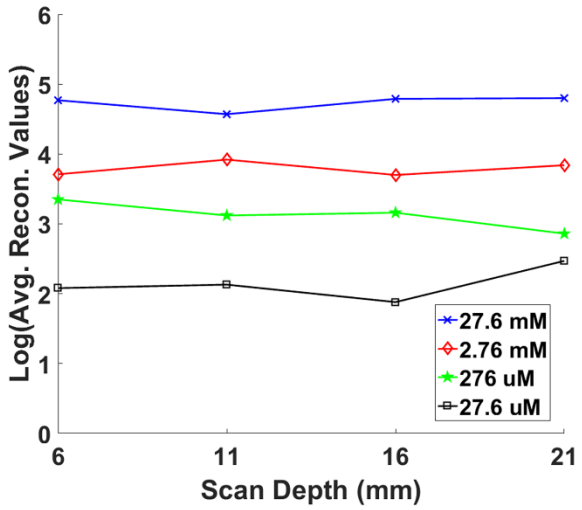

Figure 3.10. Plot of the average reconstructed values for each concentration at each scanning depth. The values given in the plot are in logarithmic (base 10) scale.

3.1.4. MicroCT imaging results

Fig. 3.11 shows the results of the microCT imaging. Prior to performing a full scan, a single projection image for each concentration was taken with an exposure time of 50 ms. After the preprocessing (i.e. dead pixel correction), a single projection image is shown in Fig. 3.11(a). From these images, the target can only clearly be seen in the 27.6 mM case but not in the other three cases (2.76 mM, 276 µM, and 27.6 µM). After performing a full microCT scan, the reconstructed microCT images at a single transverse slice are displayed in Fig. 3.11(b) for the four different target concentration cases. Although we could not see the target in the single projection image taken for the 2.76 mM case, after the full scan, the

target can be visualized as shown in Fig. 11(b). Again, the target could not be reconstructed for the cases of 276 µM and 27.6 µM. To further analyze the reconstructed microCT images, we plot the normalized profile lines across the targets in Fig. 3.11(c). The vertical line profile position is indicated by the green dotted line in Fig. 11b. From the line profile of the 27.6 mM case, the contrast between the target and background can be clearly visualized in the plot. For the 2.76 mM concentration, the contrast can be seen but it is not as evident as in the prior case. The rest of the concentrations demonstrated no contrast in their normalized line profiles. It appears that the limit of detection in microCT for a GOS:Eu^{3+} target is about 2.76 mM, which is currently 100 times lower than that of XLCT.

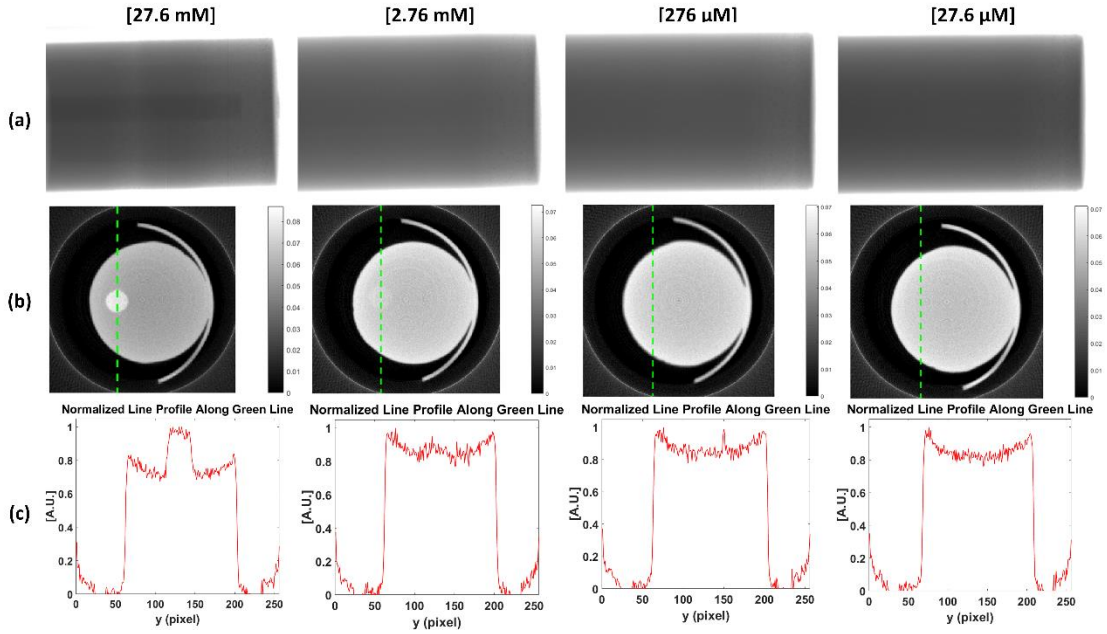

Figure 3.11. microCT imaging results. (a) Single projection images. (b) microCT reconstructed images. (c) Normalized line profile along vertical green line shown in (b).

3.1.5. Effects of optical absorber on XLCT reconstruction

For the phantoms fabricated with India ink to closely mimic the optical absorption of tissues, we performed both a full XLCT and microCT scan. For the XLCT measurements, we only used a single scanning depth at 11 mm. The reconstructed XLCT images and the zoomed-in target region for these phantoms are shown in Fig. 3.12(a) and Fig. 3.12(b), respectively. The only noticeable effect from the addition of the ink was a minor decrease in the optical signal intensity. The decrease was not enough to compromise the reconstruction and for all cases, the target was reconstructed successfully in the correct position. Table 3 shows the evaluated image quality metrics each case. The maximum TSE for all the cases was again 4.35%, similar to our results for the non-ink phantoms. In addition, the DICE was around 90% for all cases (89.774, 91.255, and 92.015 %) except the 27.6 µM; however, the result is still acceptable at 79.195%. Based on the microCT reconstruction for these phantoms, the extra addition of ink did not change the results,

primarily because the addition of ink does not cause any noticeable change in x-ray attenuation.

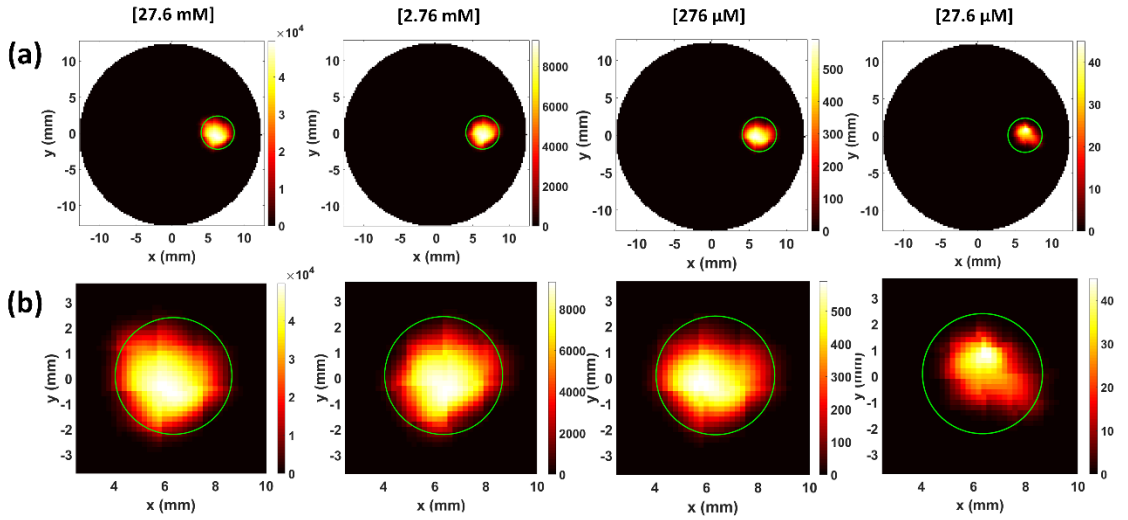

Figure 3.12. XLCT reconstructed images for the phantoms with added India ink. (a) The reconstructed image. (b) Zoomed-in target region

3.1.6. Discussion and conclusions

In this work, the sensitivity of two imaging modalities, XLCT and microCT were compared using phantom experiments with GOS:Eu^{3+} targets. In our study, we used GOS:Eu^{3+} target concentrations consistent with those used for numerical simulations for CT reconstruction in [46]. For all concentrations, XLCT was able to detect the optical signal emitted from the target when the target was excited by the x-ray beam and based on our XLCT reconstructed images (Fig. 3.7), the signal was sufficient to reconstruct the target in the correct location with high DICE and low TSE (Table 3.2). We can also see from Fig. 3.9 that even as we increase our scanning depth, we can still reconstruct our target with a low TSE, which means that there was little variation in the reconstructed target size. In addition, we found that the standard deviation in the average reconstructed values was about 30% for depths up to 16 mm. Since we have not performed a calibration of our system in regards to the reconstructed values or concentrations, we believe this result is acceptable. Overall, from the results obtained, it seems that we have not quite yet reached the threshold for detection for XLCT, especially at 6 mm depth.

One phenomenon observed during our XLCT scans was the presence of some background luminescence emitted from our phantom. During all times of scanning, from the EMCCD camera images the top surface of the phantom was always visible (with very low contrast) indicating that this was probably not due to the EMCCD camera noise but some other phenomena. For x-ray luminescence imaging, it was reported in [9] that a source of background luminescence during imaging is water which our phantom is mostly composed of. However, our results could not verify this conclusion as shown in Fig. 3.6, in which we did not observe the signal variations when the x-ray beam excited the

background phantom (98% water) from linear steps 1-10. Especially we observed the same amount of background signals when the x-ray beam barely touched the phantom in linear scan step 1 (the left-most point in Fig. 3.6(a)), which indicates that the background signals might not be from the x-ray excitation of water. Furthermore, the emitted signal from the 0.01 mg/mL target is approximately 400 times larger than the background signal, which indicates that the XLCT detection limitation is far beyond 0.01 mg/mL for a deep GOS:Eu^{3+} target.

Our microCT reconstructed images are shown in Fig. 3.11(b). Based off these results, we can see that the target can be visualized for the 27.6 mM and 2.76 mM cases and not for the other lower concentrations. Based on the low contrast seen from the microCT image for the 2.76 mM case, it seems this is approximately the limit of detection for microCT. The results are very consistent when comparing the numerical simulation results from [46] to our reconstructed microCT images (Fig. 3.10(b)), since the 1.0 mg/mL (2.76 mM) results both demonstrate similar contrast. From the results it is quite clear that the use of an x-ray induced optical signal (as in XLCT), provides a significant increase in sensitivity for detection of GOS:Eu^{3+} targets compared to the purely x-ray attenuation based microCT imaging alone. We also found that the presence of an optical absorber such as India ink, does not dramatically affect our results. Although there is a minor decrease in the optical signal overall, it is not enough to compromise our image quality dramatically.

One of the major advantages of XLCT over other optical imaging modalities like FMT, are the use of photons with wavelengths in the near-infrared (NIR) range. Upon x-ray excitation, the GOS:Eu^{3+} particles will emit photons primarily at 623 and 703 nm. Photons at these wavelengths have very high tissue penetration ability with modest scattering thus are ideal for optical imaging at depth. In a previous study [46] it was demonstrated by numerical simulations that XLCT could image a 4.8 mm diameter GOS:Eu^{3+} target with the same concentrations used in this study, up to a scanning depth of 20 mm. In addition, XLCT was demonstrated experimentally in [20] to be able to image up to a depth of 7.7 mm. In this study, we performed imaging on a 4.6 mm diameter target and shown experimentally we could perform imaging with concentrations as low as 27.6 μM at a scanning depth of 21 mm (Fig. 3.7). From Table 3.2, we can see that for each case (with exception to 27.6 μM), as the scanning depth increased, there was little variation in our reconstructed target size with a maximum target size error of 4.35%. For the 27.6 μM target at 21 mm scanning depth, the large target size error can be attributed to the weak signal obtained from such a small concentration of GOS:Eu^{3+} at such a significant depth (21 mm). For molecular imaging however, the depths shown are sufficient for most applications.

In this study, we demonstrated that XLCT's use of x-ray induced NIR optical photons as the basis for image contrast as opposed to x-ray attenuation (as in CT) brings dramatic improvements in the ability to detect contrast agents based on nanophosphors (e.g. GOS:Eu^{3+}). From our microCT reconstruction, we found that we could barely detect

targets at a concentration of 2.76 mM while for XLCT, we successfully reconstructed targets with concentrations as low as 27.6 μM and could go even lower. Future directions regarding XLCT can allow for even higher measurement sensitivity than observed in this study. With ongoing research regarding nanophosphor synthesis, we may see phosphors fabricated with greater light yield (such as in [37, 40]) which can improve the sensitivity of XLCT. In addition, the sensitivity can also be improved by using a higher sensitivity photon detector or a higher flux x-ray beam as seen in Section 2.3. Overall, with the combined merits of both x-ray (high spatial resolution) and optical (high sensitivity) imaging modalities as well as the ability to image at significant depths, XLCT has great potentials to become a powerful tool for molecular imaging where in the past, x-rays played little role.

3.2. Background Luminescence in XLCT imaging

The signal generation in XLCT is a form of radioluminescence where the ionizing radiation (in this case, x-ray photons) causes the emission of optical photons from the embedded contrast agents, and it is generally assumed that all the optical photons generated are emitted only from the contrast agents. However, numerous studies have reported other sources of optical photons from the radioluminescence of air, water, and biological tissue [9, 74-89] at energies below the Cerenkov radiation threshold which will provide background noise and limit the molecular sensitivity of XLCT imaging. Yamamoto *et al.* conducted various luminescence imaging experiments with different sources of radiation to image both water and air. Using proton-beam irradiation, they found that water was able to luminescence, even during traditional proton-therapy, and determined that this information could be useful for dose and range estimation [74-77, 84]. With carbon-ion irradiation, they performed similar luminescence imaging (also with energy below the Cerenkov-threshold) and determined, by measuring and deriving the light spectra, that this water luminescence was likely caused by an electromagnetic pulse produced from the dipole displacement inside water molecules as the derived spectra was found to be proportional to $\lambda^{-2.0}$ [77, 78]. In addition, they also determined other radiation sources such as alpha particles [80], beta particles [81], and gamma photons [82] could also produce luminescence in water at energies below the Cerenkov-threshold. Ionization and production of luminescence in air is also generally a well-documented phenomenon and is primarily attributed to atmospheric nitrogen [86, 87]. Lastly, x-ray photons were also demonstrated in the luminescence imaging of water at sub-Cerenkov-threshold energy levels [84, 85] and the emitted luminescence was found to be proportional to the x-ray energy. In particular, this generation of optical photons with low energy x-rays is of particular concern or interest for XLI/XLCT imaging. To examine this phenomenon further, and to observe its implications for XLI/XLCT imaging, we performed several experiments in this study. We performed two-dimensional (2D) XLI of water, air, and tissue-mimicking phantoms, including a phantom embedded with 0.01 mg/mL GOS:Eu^{3+} particles, and imaged the phantoms at different scanning depths using a focused x-ray beam with energy much less than the Cerenkov radiation threshold (260 keV for water). We have

also used a spectrograph mounted on an EMCCD camera to measure the emitted x-ray luminescence spectra from distilled water, two different tissue-mimicking phantoms, and meat (tissue) and fat samples from both chicken and pork.

3.2.1. Experimental set-up and phantoms for XLI experiments

A schematic of the experimental set-up used for the XLI is shown in Fig. 3.13(a) and a photograph of the set-up is shown in Fig. 3.13(b). We used a similar set-up as described in Section 2.3 for our imaging studies. In short, we used the X-Beam Powerflux x-ray tube which generated a focused x-ray beam with a focal diameter of about 100 µm as the x-ray source. The sample for XLI was placed on the manual lab jack that is fixed to a motorized rotary stage and then mounted to a motorized linear stage. The x-ray beam was constantly monitored by an x-ray detector fixed opposite of the x-ray tube. Objects to be imaged were positioned such that the x-ray beam passed its center and we performed the XLI without rotating the object for different scanning depths from the object top surface. Emitted optical photons were then reflected by a flat mirror and detected with a water-cooled EMCCD camera with a focusing lens which was shielded by a lead wall to protect from scattered high-energy x-ray photons. The entire system was placed in a light-tight and x-ray shielding cabinet and controlled by programs on a lab computer.

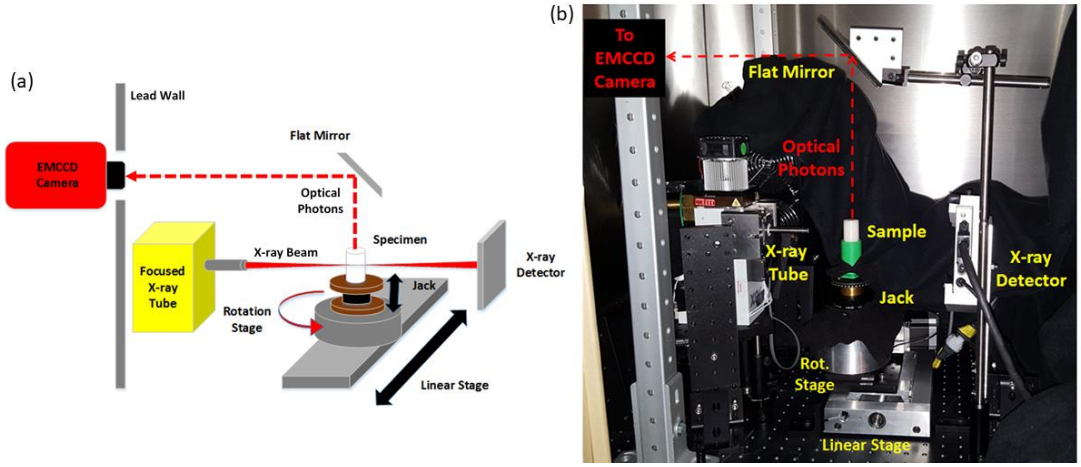

Figure 3.13. Experimental set-up for the XLI. (a) Schematic of the XLI set-up; (b) Photograph of the XLI set-up.

We performed XLI experiments for five different phantoms as listed in Table 3.3 and have also listed their scanning scheme parameters. The geometry of the first three phantoms is plotted in Fig. 3.13(a). The fourth and fifth phantoms were the air and liquid water phantoms as shown in Fig. 3.13(b), in which the computer-aided design (CAD) model of them is plotted. The first phantom was an agar phantom that was composed of water and 2% agar. The second phantom was a titanium dioxide (TiO_2) phantom that was composed of 2% agar, 1% TiO_2, and 0.003% India ink such that the phantom had tissue-mimicking optical properties of μ_a = 0.007 mm^{-1} (absorption coefficient) and $\mu`_s$ = 1.00 mm^{-1} (reduced scattering coefficient) at the wavelength of 703 nm, the longest emission

peak for GOS:Eu^{3+}. The third phantom, a GOS:Eu^{3+} phantom, had the same composition as the second phantom, except that it contained a through-hole of 4.60 mm diameter which was embedded with a target containing 0.01 mg/mL of GOS:Eu^{3+} particles (UKL63/UF-R1, Phosphor Tech. Ltd.) as shown in Fig. 3.13(a) (blue cylinder). The three phantoms were used to compare the radioluminescence from water and tissue-mimicking phantoms, including a tissue-mimicking phantom which was embedded with a small concentration (0.01 mg/mL) of GOS:Eu^{3+} particles.

Table 3.3. Phantoms for the XLI experiment.

Phantom Name	Phantom Composition	Scanning Parameters	Target
Agar Phantom	2% agar, water	X-ray: 50 kV, 1.0 mA EMCCD Exposure: 5s	None
TiO_2 Phantom	2% agar, 1% TiO_2, 0.003% India Ink	X-ray: 50 kV, 1.0 mA EMCCD Exposure: 5s	None
GOS:Eu^{3+} Phantom	2% agar, 1% TiO_2, 0.003% India Ink	X-ray: 50 kV, 1.0 mA EMCCD Exposure: 5s	0.01 mg/mL GOS:Eu^{3+} Size: 4.60 mm
Air	Air	X-ray: 50 kV, 1.0 mA EMCCD Exposure: 60s	None
Distilled Water	Distilled Water	X-ray: 50 kV, 1.0 mA EMCCD Exposure: 60s	None

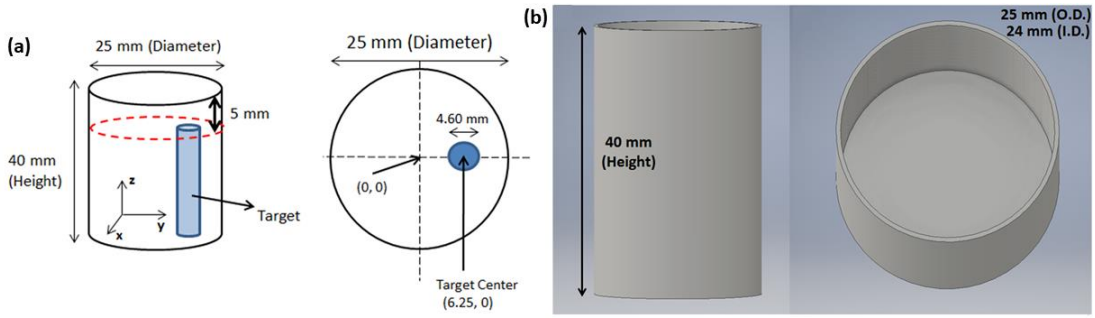

Figure 3.14. Phantom geometries for the XLI experiment. (a) Cylindrical turbid-media phantom geometry; (b) CAD model of the container used for XLI of air and water. Note: for (a), only the GOS:Eu^{3+} phantom contained a target.

For the first three phantom experiments, the phantom was placed on the stage of the XLI system (seen in Fig. 3.13(b)). During the experiments, the x-ray tube was operated at a tube voltage of 50 kV and a tube current of 1.0 mA (50 W) while the EMCCD camera was cooled to a temperature of -92.20ºC and operated at the maximum EM gain and sensitivity gain of 255 and 5 respectively. During imaging, the x-ray beam was positioned to excite the center of the phantoms, and for the phantom with the GOS:Eu^{3+} target, the beam passed the center of the target as well. For the phantom experiments, an EMCCD camera exposure time of 5 seconds was used for each scanning depth (defined as the distance from the scanned section to the top surface of the phantom) of 1 mm to 10 mm (10 depths total, 1 mm increments). We acquired a total of 3 images for each scanning depth to obtain an average. In addition, we took background images (dark images) with the same measurement parameters except with the x-ray tube was off.

Using a 3D printer (Makerbot Replicator 2X, Makerbot), we fabricated a cylindrical black ABS plastic container with an outer diameter (O.D.) of 25 mm and an inner diameter (I.D.) of 24 mm and height of 40 mm with an open top (Fig. 3.14(b)). We performed XLI using the same parameters as the phantom experiment described above for the first three phantoms, except that the EMCCD camera exposure time was increased to 1 minute. For the XLI of air, we irradiated the empty container. For the XLI of liquid water, we filled the container with distilled water prior to imaging. Like the previous experiment, we took 3 images for each scan depth from 1 mm to 10 mm as well as dark images (x-ray off).

3.2.2. Measurement set-up and phantoms for the x-ray luminescence spectra

Fig. 3.15(a) shows a schematic of the experimental set-up used for the measurements of the x-ray luminescence spectra and Fig. 3.15(b) shows a photograph of the set-up. A sample to be measured was placed inside a 3D printed, thin-wall (1 mm) black ABS plastic container which has an optical fiber bundle inserted and sealed into the bottom of the container. The fiber bundle has an aperture diameter of 3 mm and one end was fixed using a lab-made adapter to the front of a spectrograph (Imspector V8E, Specim) which has a spectral sensitivity range from 380 to 800 nm and was calibrated using 2 monochromatic lasers with known wavelengths. The spectrograph was mounted on the same EMCCD camera used for the previous XLI experiments and was operated at the maximum gain and a temperature of -92.20ºC.

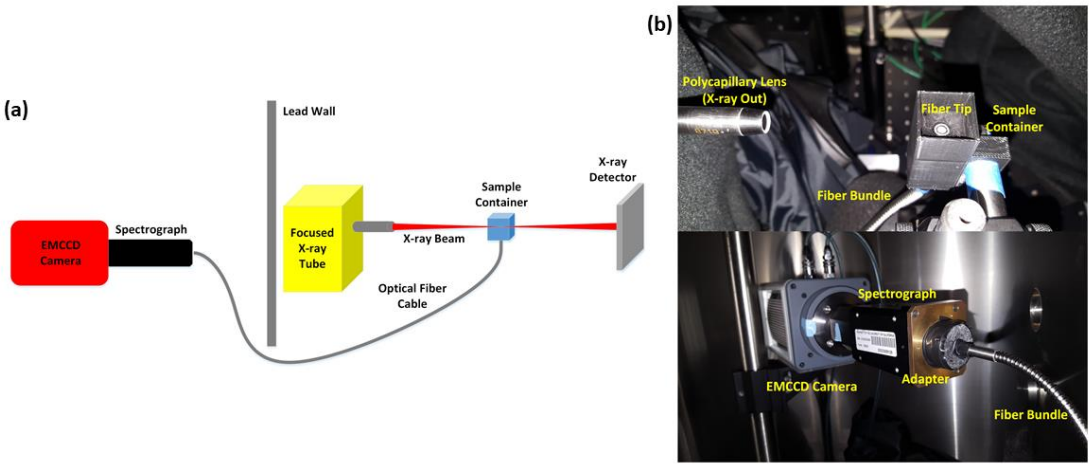

Figure 3.15. Set-up for x-ray luminescence spectra measurements. (a) Schematic set-up; (b) Photography of set-up.

All the phantoms for the x-ray luminescence spectra measurements and their measurement parameters are listed below in Table 3.4. The first sample to be measured was a suspension of GOS:Eu^{3+} particles (1.0 mg/mL) which we used to confirm the known emission peaks from previous literature to ensure that the spectrometer was calibrated properly. The GOS:Eu^{3+} particles were mixed with distilled water and the solution was poured into the container for measurement. For the GOS:Eu^{3+} measurement, we used an EMCCD camera exposure time of 1 min. Next, we irradiated and measured the x-ray

luminescence spectra of distilled water as well as cubic phantoms made of TiO_2 and India ink that had the same optical properties as in the previous XLI phantom experiments as well as an additional phantom composed of 1% Intralipid and 2% agar to compare between two different recipes commonly used for background phantoms. The distilled water was poured into the container for measurement and the phantoms were each cut into cubes of 10 mm^2 size and then placed into the container directly on top of the fiber bundle tip. During all measurements, the top of the container is sealed with a black lid to prevent ambient light. Also of note, the stability of water luminescence was confirmed in [74, 84] and it was determined that distilled and tap-water had no difference in radioluminescence intensity and distribution. Lastly, as a simple comparison between the tissue-mimicking phantoms and real biological tissue we also used chicken and pork samples and measured their x-ray luminescence spectra as well. We separated the pure fat portions from the portions containing only the meat and measured the spectra of both separately. The meat and fat were cut into similar sizes as the cubic phantoms before being placed in the container. The exposure time of the EMCCD camera was increased to 10 mins for all of these measurements. For each measurement, the x-ray beam was positioned 2 mm above the optical fiber bundle tip in the container (confirmed using the x-ray detector).

After each measurement was taken, a background spectrum was acquired using the same settings with the x-ray beam turned off. The x-ray tube was set to max power for all measurements (50 kV and 1.0 mA). During these experiments, the EMCCD camera and the spectrograph were placed inside of an x-ray shielding, light-tight cabinet and were covered with a black blanket.

Table 3.4. Phantoms for the x-ray luminescence spectra measurements.

Phantom Name	Phantom Composition	Measurement Parameters
GOS:Eu^{3+} particles	GOS:Eu^{3+}, water	X-ray Tube: 50 kV, 1.0 mA EMCCD Exposure: 60 s
Distilled Water	Distilled Water	X-ray Tube: 50 kV, 1.0 mA EMCCD Exposure: 600 s
TiO_2 Phantom	2% agar, 1% TiO_2, 0.003% India Ink	X-ray Tube: 50 kV, 1.0 mA EMCCD Exposure: 600 s
Intralipid Phantom	2% agar, 1% intralipid	X-ray Tube: 50 kV, 1.0 mA EMCCD Exposure: 600 s
Chicken Meat	Chicken Meat	X-ray Tube: 50 kV, 1.0 mA EMCCD Exposure: 600 s
Pork Meat	Pork Meat	X-ray Tube: 50 kV, 1.0 mA EMCCD Exposure: 600 s
Chicken Fat	Chicken Fat	X-ray Tube: 50 kV, 1.0 mA EMCCD Exposure: 600 s
Pork Fat	Pork Fat	X-ray Tube: 50 kV, 1.0 mA EMCCD Exposure: 600 s

3.2.3. XLI experimental results

In Fig. 3.16, we show the top surface measurements by the EMCCD camera for the three different phantoms (Agar phantom (Fig. 3.16b), TiO_2 phantom (Fig. 3.16c), and the GOS:Eu^{3+} phantom (Fig. 3.16d)) under x-ray irradiation for the scanning depth of 5 mm

and a background image when the x-ray beam was off (Fig. 3.16a). For the agar phantom, we can visualize the x-ray beam as it enters the phantom initially, then the intensity quickly fades away. The luminescence intensity seems to increase in the area where the x-ray beam entered the phantom indicating optical photons being generated by the agar phantom from the x-ray irradiation. For the case of the tissue-mimicking phantom with no targets (Fig. 3.16c), the x-ray beam could not be visualized entering the phantom as we could in Fig. 3.16b due to the absorption and scattering of optical photons by the phantom, but the overall luminescence intensity from the phantom top surface is still brighter for this case than for water. Lastly, we can see that with the inclusion of a 0.01 mg/mL GOS:Eu^{3+} target, the overall signal intensity from the phantom top surface increases quite dramatically because the target emits much more photons than the background phantom.

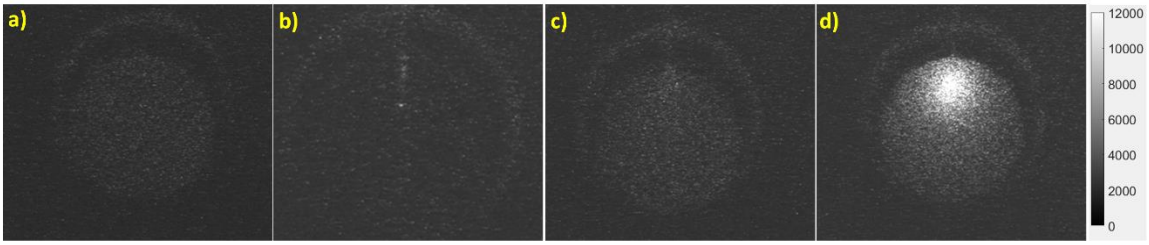

Figure 3.16. Top surface EMCCD camera images for the 5 mm scan depth. A) background image (x-ray off), b) agar phantom (x-ray on), c) TiO_2 phantom (x-ray on), d) GOS:Eu^{3+} phantom (x-ray on). The grayscale indicates the luminescence intensity in arbitrary units.

To further compare the luminescence intensities for the three phantoms for all the scanning depths, we took an elliptical region of interest (ROI) of 2.8 by 5.5 mm^2 on the phantom top surface for all three images acquired at each scan depth, and obtained an averaged intensity value in that region. Then using the dark images acquired, we subtracted the mean dark value for all the cases. The final intensity values obtained are then plotted for each case for each of the scanning depths in Fig. 3.17 using the logarithm (base-10) of the intensities for better visualization. The highest luminescence intensity was seen for the GOS:Eu^{3+} phantom (red line), then the TiO_2 phantom (green line), finally the lowest intensity was seen in the agar phantom (blue line). From Fig. 3.17, for the scan depth of 1 mm, the ratios of the luminescence intensity for the cases with the GOS:Eu^{3+} target to the intensity for the TiO_2 phantom and for the water phantom (prior to taking the logarithm) was calculated to be 12.5:1.0 and 18.0:1.0 respectively, which means that the TiO_2 phantom and agar phantom is equivalent to a GOS:Eu^{3+} target with an approximate concentration of 0.8 µg /mL and 0.55 µg/mL, respectively in terms of the emitted luminescence intensity.

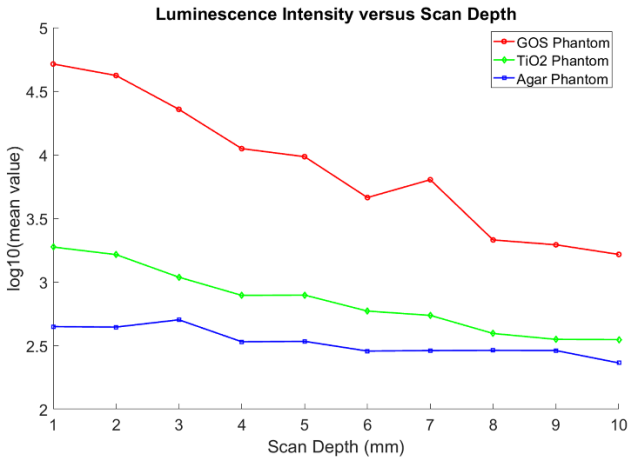

Figure 3.17. Plot of the luminescence intensity versus the x-ray scan depths for the XLI experiment. Logarithm scale is used to better visualize the intensity differences.

Fig. 3.18 shows an EMCCD camera image from the irradiation of air (Fig. 3.18a) and water (Fig. 3.18b) at the scan depth of 5 mm. The scale of these images was adjusted for better visualization. In both images, the focused x-ray beam could be clearly visualized (from the ionization of air) and for the case of water, we can see as the x-ray beam passes through the water in the container, that there are optical photons being generated despite that the x-ray energy level used (50 kV) is well below the Cerenkov radiation threshold. Because there are three LEDs on our x-ray tube, we can see a small reflection on the top surface of the water in Fig. 3.18b (highlighted as noise in the figure) due to them not being perfectly covered. To compare the intensity values for different scan depths, we plotted the mean value from a similar 2.8 by 5.5 mm^2 elliptical ROI from the 3 images acquired at each scan depth after background subtraction in Fig. 3.19. We can see that for each scan depth, there was very little difference in the luminescence intensities for both cases. In addition, the average intensity obtained from water was approximately 3 times greater in magnitude than for the case of air for all ten scan depths.

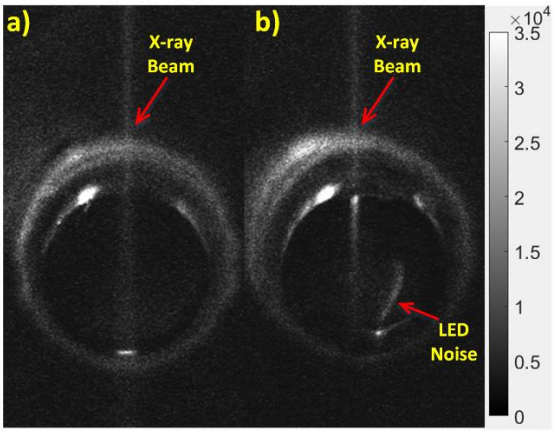

Figure 3.18. EMCCD camera images with adjusted scale to show the radioluminescence of a) air and b) water at 5 mm scan depth. The grayscale indicates the luminescence intensity in arbitrary units.

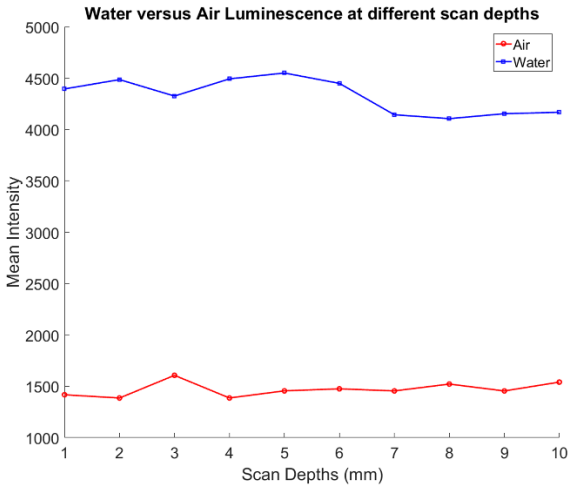

Figure 3.19. Plot of the mean intensity values versus scanning depth for the case of water (blue line) and air (red line) x-ray luminescence.

3.2.4. X-ray luminescence spectra results

After taking the measurements from the spectrograph with the EMCCD camera, a simple image correction was performed on the images to reduce the EMCCD image noise (hot spots) using the open source ImageJ software (ImageJ, NIH). Afterwards, the background spectrum was removed and the final resulting spectra for each case were plotted using MATLAB. The emission spectrum from GOS:Eu^{3+} was previously shown in Fig. 1.1 (not reshown here for redundancy). For the GOS:Eu^{3+} particles, we identify the emission characteristic peaks at 588, 612, 623, and 703 nm respectively as indicated in Fig. 1.1, which validates this spectrum measurement system.

The x-ray luminescence spectra for distilled water and the tissue-mimicking phantoms are shown in Figs. 3.20 and Fig. 3.21, respectively. For the spectrum of water under x-ray irradiation, we see a broad spectrum across the entire visible range is produced. The two peaks around 775 and 800 nm are from EMCCD camera noise that was not completely removed during the image correction. For the spectrum obtained from the intralipid phantom (Fig. 21(a)), we also do not observe any obvious peaks as well and for the spectrum of the phantom made from the TiO_2 (Fig. 21(b)), we see a small but broad peak from around 415 nm to around 750 nm produced under x-ray irradiation which is unseen in the previous two cases. In addition, the overall spectral intensity was also higher in the TiO_2 compared with the intralipid. These samples were all measured in the same time window for more comparable results. Lastly, we plotted the measured x-ray luminescence spectra from the chicken and pork meat samples (Fig. 3.22) and fat samples (Fig. 3.23). From the spectra obtained from the fat samples (Fig. 3.23), we can see very obviously in both cases, that there is a large peak around the 600 nm range. With exception to the peak that can be seen at around 525-550 nm for the chicken fat (Fig. 3.23(a)), the spectra for fat in both cases seem to share similarities in their overall shape and intensities.

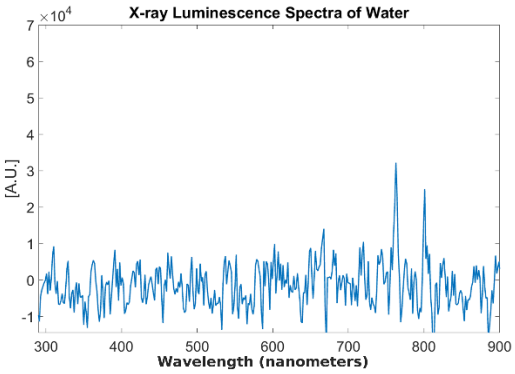

Figure 3.20. Measured x-ray luminescence spectra for distilled water.

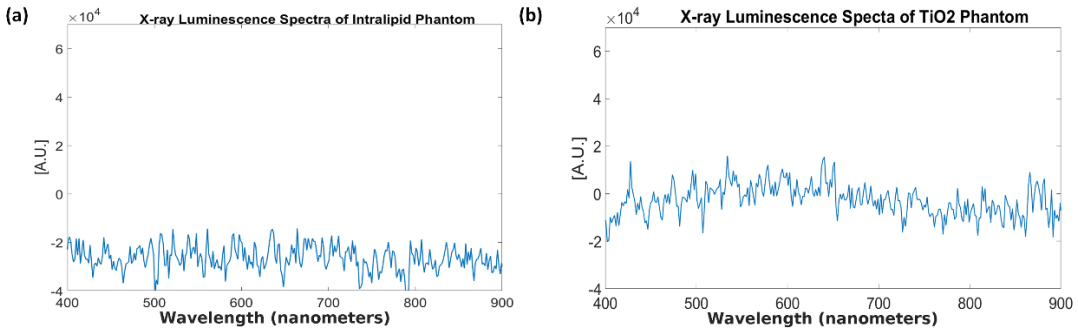

Figure 3.21. Measured x-ray luminescence spectra for the two different tissue phantoms. (a) Intralipid phantom (b) TiO_2 phantom.

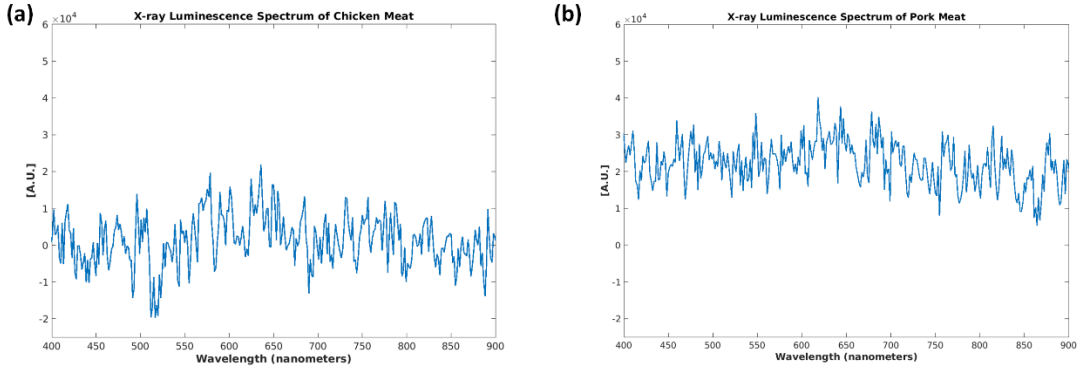

Figure 3.22. Measured x-ray luminescence spectra from the different meat samples. (a) Chicken meat and (b) Pork meat.

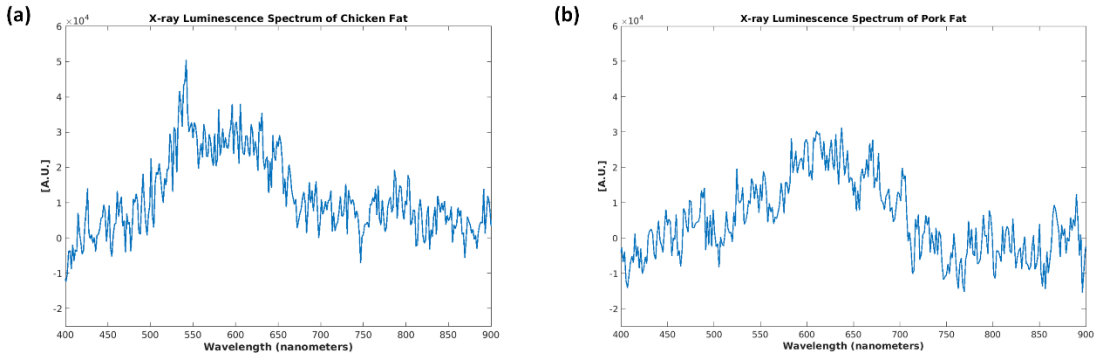

Figure 3.23. Measured x-ray luminescence spectra from the different fat samples. (a) Chicken fat and (b) Pork fat.

3.2.5. Discussion and conclusions

In this work, we performed x-ray luminescence imaging (XLI) of air, water, and tissue-mimicking phantoms and measured the x-ray luminescence spectra of water, two different types of tissue-mimicking phantoms, as well as meat and fat samples from both chicken and pork. These sources of optical photons should be considered, as they will limit the molecular sensitivity of XLCT imaging, especially for *in vivo* imaging studies. From our results of the XLI of the different types of phantoms (Figs. 3.16 and Fig. 3.17) we can see clear differences in the luminescence intensities for each case. As expected, the GOS:Eu^{3+} phantom had the highest luminescence intensity. When compared to the luminescence from the TiO_2 phantom, we can see that the luminescence intensity was slightly higher than the agar phantom as well which means there is another source of optical photons in the TiO_2 phantom. With regards to the luminescence intensity as the scanning depth was increased, we can see an expected drop in the intensity. For the GOS:Eu^{3+} phantom, we can see that even at the 10 mm scan depth, after subtraction of the background signal, we still have a strong signal which is expected since we were able to reconstruct a similar phantom with the same concentration target in Section 3.1 [54, 55] demonstrating XLCT for scanning depths up to 21 mm. In addition, GOS:Eu^{3+} is known to emit optical photons in the red and near-infrared range (NIR optic window) with good tissue penetration ability which means that photons can travel longer distances, thus being able to reach the top surface even when generated at large scan depths. If the signal-to-noise ratio is 1, we can estimate that the XLCT imaging sensitivity limitation is about 0.8 µg/mL if the GOS:Eu^{3+} particles are used as contrast agents. A recently published study has reported that the luminescent efficiency of nanoscale rare-earth phosphors is about 40% of that from the microscale particles (as was used in this paper) [36]. Thus, we can estimate that the XLCT imaging limitation of nanophosphors is about 2.0 µg/mL (or about 5.28 µM) for the phantom experiments. It is worth noting that the imaging limitation is also dependent upon other factors as well such as the imaging depth.

For the experiment comparing the XLI of air and water (Figs. 3.18 and Fig. 3.19) we can see that water produced a greater luminescence intensity than air, about 3 times the

intensity (Fig. 3.19) and that for the different scanning depths there was very little change in the intensities seen for both due to the fact that there is almost no optical absorption and scattering in these two media. The luminescence of air was expected as it is a well-documented phenomenon and is attributed primarily to the ionization of nitrogen in the air [9, 86-87]. Since the ionization produces optical photons primarily in the range of 350-450 nm, it should not be a major problem for XLCT imaging since photons in this short wavelength range can easily be absorbed by tissues and then filtered with a long pass filter. For the XLI of water, we can see in Fig. 3.18b for the distilled water and even in Fig. 3.16b for the agar phantom, that as the x-ray beam entered our sample, the luminescence intensity is actually increased quite a bit as the x-ray energy is being absorbed by the water even though the x-ray photon energy is far below the Cerenkov radiation threshold. Recently, there has been much research regarding the radioluminescence of water at energy levels well below the Cerenkov radiation threshold which was confirmed in our experiment. Currently, the exact mechanism of this phenomenon is not yet fully understood, but several proposals have been made from the ionization of radicals generated in water [88] and more recently as mentioned before, from carbon-ion irradiation experiments, from the electromagnetic pulse produced from the dipole displacement inside water molecules [79]. Reports on the radioluminescence yield of water have also estimated that per 100 keV x-ray photon absorbed, 0.17 optical photons are emitted [9].

In Figs. 3.20-3.23, we plotted the results of the different x-ray luminescence spectra for the different cases. In [79], using carbon-ion irradiation and an EMCCD camera equipped with long pass filters at various wavelengths, the spectra of water there was found to range from 300-700 nm, with most of the luminescence occurring in the UV or blue part of the spectrum (300-500 nm). In addition, in [80], the radioluminescence of water using alpha particles was also shown to produce a pretty broad spectrum from about 350 to 650 nm. In the spectrum shown for the phantom made from TiO_2 and India ink (Fig. 21b), we found that there was a broad emission peak from about 415 to 750 nm which was not seen in the spectrum for intralipid (Fig. 3.21a), which might suggest that we prefer to use intralipid as the optical scatterer instead of TiO_2 in future XLCT imaging experiments. As a quick and easy comparison to the tissue-mimicking phantoms, we obtained both chicken and pork from a local store, and separated meat and fat samples from each to see any differences in the obtained spectra. As we can see from Figs. 3.22 and 3.23, the spectra we obtained, especially for the fat samples differed quite a bit in terms of the shape. Of course, the meat samples themselves also have small traces of fat as well so we see some similar characteristics in both the meat and fat spectra, although we have a more apparent peak in the fat samples that arises starting in both at around 400 nm and extending to approximately 700 nm. Compared with the tissue-mimicking phantoms, it looks like the meat does not have any obvious emission peaks as seen in Fig. 3.22. The fat spectra, however, has a more noticeable emission peak as seen in Fig. 3.23. If nanophosphors that emit at 700 nm or longer are used for XLI/XLCT imaging the background luminescence at the shorter wavelengths can be spectrally filtered out, if necessary, to obtain a higher signal-to-

background (SBR) ratio for improved imaging. In addition, other techniques for removing background noise can also be used to achieve a higher SBR for XLCT to improve the image quality. For example, more recently there has been much interest in applying deep-learning methods to aid in not only image analysis, but also in image reconstruction [90, 91]. For example, we could incorporate different information such as spectral or spatial information (e.g. x-ray beam location) to reduce unwanted background signals via post-processing. We could possibly remove the photons caused by air scintillation since this phenomenon can be observed directly from the images by possibly training an algorithm to recognize this (similar to pattern recognition). In addition, we could possibly monitor the x-ray beam position and remove any signals not in the trajectory which would improve the imaging.

In summary, we have measured the x-ray luminescence intensity from distilled water and different phantoms, from which we can see that the luminescence intensity from the phantom background is equivalent to a GOS:Eu^{3+} microphosphor target concentration of 0.8 µg/mL or 2.0 µg/mL (5.28 µM) for nanophosphor GOS:Eu^{3+}. We have validated our x-ray luminescence spectrum measurement set-up and then measured the x-ray luminescence spectrum from distilled water, an Intralipid phantom, a TiO_2 phantom, as well as samples of both chicken and pork meat and fat as comparisons to real biological tissue. Our results suggest that it is better to use intralipid instead of TiO_2 phantoms for future XLCT phantom imaging studies.

CHAPTER 4

HIGH-RESOLUTION XLCT IMAGING

4.1. Method for Improving the Spatial Resolution of NB-XLCT Imaging

For the traditional NB-XLCT imaging, the fundamental limit of spatial resolution is determined by the beam aperture size [19, 50]. From these studies, we know that it is not possible to separate two targets when the x-ray beam size is larger than the target diameter and edge-to-edge (EtE) distance. In our studies in Section 2.1 [50], we reported that the spatial resolution of NB-XLCT imaging is about double the scanning x-ray beam diameter. Thus, efforts towards improving the spatial resolution of XLCT imaging have focused on methods for obtaining a small x-ray beam size. We previously demonstrated two methods for achieving a small x-ray beam size. The first is by collimation of the x-ray beams with a small collimator aperture (Section 2.1) but this method has disadvantages of a low x-ray photon utilization efficiency but is easy to implement at a low cost. The other method we demonstrated was by use of a polycapillary lens to focus the x-ray beam to a fine focal spot (Section 2.3). This method can produce a high flux x-ray beam but it relatively costly to implement. In this study, we will report a new approach to improve the spatial resolution in NB-XLCT imaging to further break its current spatial resolution limit of double the x-ray beam size. The approach does not add any physical costs but is accomplished simply by reducing the x-ray beam scanning step size. The obvious trade-off of this approach is the increase in scanning time as more steps are then needed to traverse the phantom for each angular projection. In this work, we will demonstrate the efficacy of using smaller x-ray beam step sizes for improving the spatial resolution and imaging quality by numerical simulations and phantom experiments.

4.1.1. Proposed scanning scheme

For conventional NB-XLCT imaging, the object is scanned by a sequence of single x-ray beams moving at predefined directions and positions, similar to the first-generation CT imaging systems. With the multiple-beam approach (Section 2.2), multiple x-rays beams can be used, but the scanning step size is still kept equal to the scanning beam diameters. Under such scanning strategies, the spatial resolution is determined by the x-ray beam diameter. In this study, we modified the scanning scheme for conventional NB-XLCT by reducing the scanning step size to be less than the x-ray beam size. This can be applied to both the single-beam and multiple-beam cases, but for simplicity, we will only demonstrate the single-beam approach. Figure 4.1 shows the proposed scanning strategy

for the single-beam case. For this approach, for each angular projection, the number of linear scanning steps (N_L) is determined by the diameter of the entire scanning region (D_{region}) and the scanning step size (S_{step}) as $N_L = D_{region}/S_{step}$.

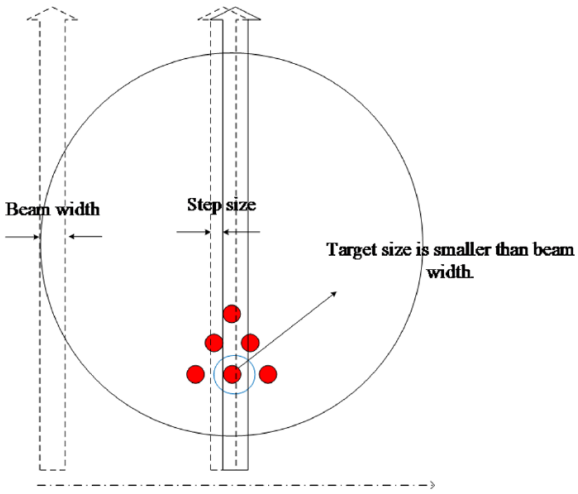

Figure 4.1. Schematic representation of linear scan setup for one typical angular projection. The red dots indicate the targets. The vertical arrows indicate the x-ray beams.

4.1.2. Numerical simulation set-up

To validate the feasibility and effectiveness of our proposed scanning strategy in XLCT, four cylindrical phantoms (phantoms A, B, C, and D) were designed for numerical simulations. For all phantoms, the diameter and height were set to 12.8 and 10 mm, respectively, as shown in Fig. 4.2(a). Six luminescent targets of 6 mm in height were placed in the phantoms at a depth of 2 mm. The diameter and EtE distance settings of the six targets for all four numerical phantoms are listed in Table 4.1. The positions of the six targets and the four fiber bundles are shown in Fig. 4.2(b). The targets' diameter is the same as the EtE distance, which has been changed from 0.4 to 0.8 mm in this study. In the transverse plot, as shown in Fig. 4.2(b), the six targets formed an equilateral triangle whose centroid was fixed at (0, −3.2 mm). The absorption coefficient (μ_a) and the reduced scattering coefficient ($\mu`_s$) of the phantom were set to 0.0072 and 0.72 mm^{-1}, respectively, at the wavelength of 703 nm, which is the longest wavelength peak in the emission spectrum of GOS:Eu^{3+}. In the simulation studies, we set the phosphor particle concentration to be 1.0 and 0 mg/mL in the target and background regions, respectively.

For all numerical simulations, four optical fiber bundles were placed 2 mm below the scanned section and 90 deg apart from each other, which were employed to collect the emitted photons on the phantom surface, as shown in Fig. 4.2(a). The diameter of the x-ray beam was fixed at 0.8 mm, and the linear scan step size was set to 0.8, 0.4, 0.2, and 0.1 mm, respectively, for each simulation. We used six angular projections with the angular

step size of 30 deg. The numerical measurements at each angular projection were generated with the forward model of XLCT proposed in Section 1.3.4. To make the simulations more realistic, 50% white Gaussian noise was added to the numerical measurements.

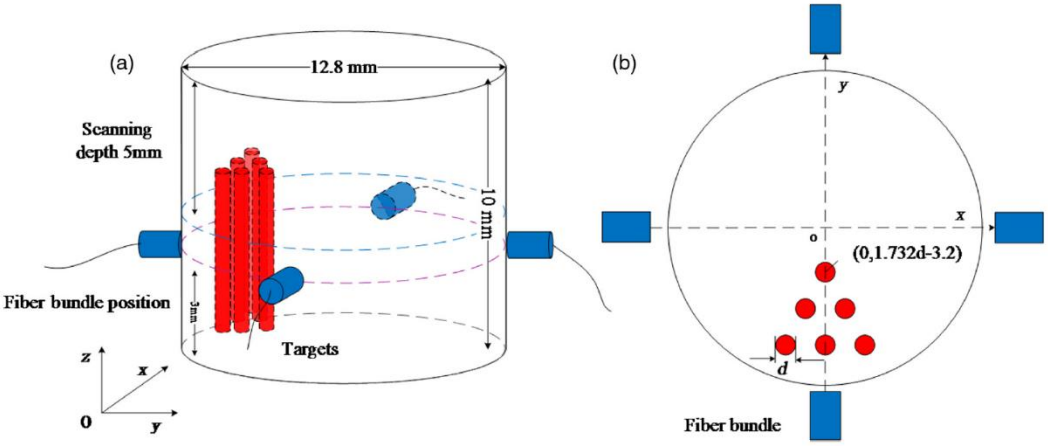

Figure 4.2. Phantom geometry and detectors setup used in the numerical simulations. (a) Overall phantom geometry and (b) transverse plot of the phantom to show the positions of six targets and four fiber bundles.

Table 4.1. Geometry of the targets embedded in each phantom for numerical simulations.

Phantom	Target Diameter (mm)	EtE Distance (mm)
A	0.8	0.8
B	0.6	0.6
C	0.5	0.5
D	0.4	0.4

4.1.3. Phantom experimental set-up

We performed our XLCT imaging experiments using the system described in Section 2.3.1. The XLCT scans were performed on a cylindrical phantom shown in Fig. 4.3. A schematic of the phantom is shown in Figs. 4.3(a) and 4.3(b) from which we can see that the phantom had a diameter of 25 mm and a height of 40 mm and was composed of 1% intralipid and 2% agar and was embedded off-center with four capillary tube targets. The same background solution was mixed with 10 mg/mL of GOS:Eu^{3+} particles (UKL63/UF-R1, Phosphor Techn. Ltd.) and was injected into the capillary tubes (Drummond Scientific) which had an inner diameter and an outer diameter of 0.4 and 0.8 mm, respectively. After the phantom was created and completely solidified, we performed a microCT scan using our lab-made microCT system, as previously described in Section 3.1.1, to determine the positions of the embedded targets. A single slice from the microCT reconstruction, corresponding to the XLCT scanning section, is shown in Fig. 4.3(c). Based on the image, the center positions of the four embedded targets were determined to be (−1.5 mm, −5.35 mm), (−1.5 mm, −6.15 mm), (−0.7 mm, −5.35 mm), and (−0.7 mm, −6.15 mm) from the center of the phantom. We then performed an XLCT scan of the phantom to validate the proposed method. We operated the x-ray tube at 30 kV and 0.5 mA and took measurements at six angular projections (30 deg/projection) using 520 steps of 50-μm step

size (four times smaller step size than our normal parameters). Lastly, we acquired 10 ms of data from the PMT at each step, as in [60], which will be detailed in Section 5.1.

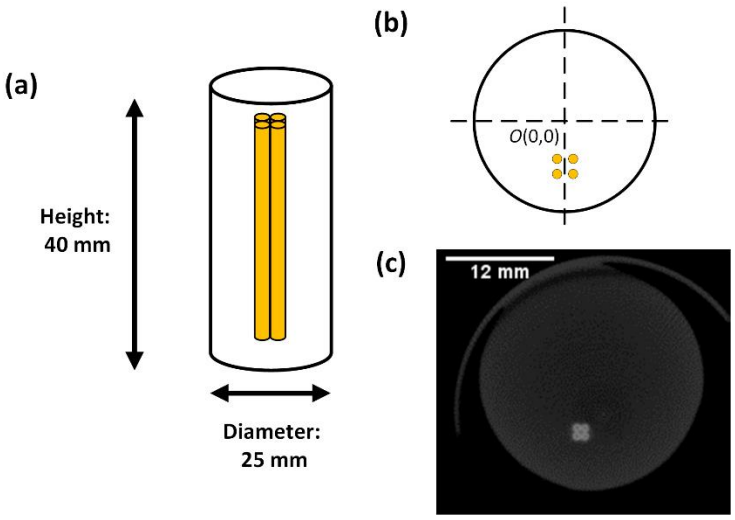

Figure 4.3. Phantom for experimental studies. (a) Schematic representation of the side view; (b) schematic representation of the top view; and (c) microCT image of phantom used in study.

4.1.4. Numerical simulation results

The XLCT image reconstruction was performed using the L^1 regularized MM reconstruction framework. For the XLCT simulations, the phantom was discretized by a finite element mesh (FEM) with 26,638 nodes, 153,053 tetrahedral elements, and 11,456 face elements, and the reconstructed section was interpolated onto a grid of 25 μm^2 pixel size and then the system matrix was interpolated onto the grid from the FEM.

For the simulations of phantom A, we simulated XLCT scanning using a straight x-ray beam with a fixed diameter of 0.8 mm but with different scanning step sizes from 0.8, 0.4, 0.2 to 0.1 mm. Figure 4.4 plots the reconstructed XLCT images of phantom A with different scanning step sizes of 0.8 mm [Fig. 4.4(a)], 0.4 mm [Fig. 4.4(b)], 0.2 mm [Fig. 4.4(c)], and 0.1 mm [Fig. 4.4(d)]. From Fig. 4.4, we can see substantial improvements in the image quality by decreasing the scanning step size. Figure 4.4(e) shows the intensity profiles along the center line of the middle row targets in Figs. 4.4(a-d). The quantitative analysis results of the simulations using phantom A are presented in Table 4.2. As shown in Table 4.2, when the scanning step size reduces from 0.8 to 0.1 mm, each of the calculated image quality metrics improved quite substantially. This indicates the improvements in shape and location accuracy, target size accuracy, spatial resolution, and overall reconstruction accuracy. There is a further increment of DICE and decrement of TSE and NMSE as the scanning step size decreases from 0.4 to 0.2 mm. There are no significant changes in DICE, TSE, SPI, and NMSE when the scanning step size is reduced from 0.2 [Fig. 4.4(c)] to 0.1 mm [Fig. 4.4(d)].

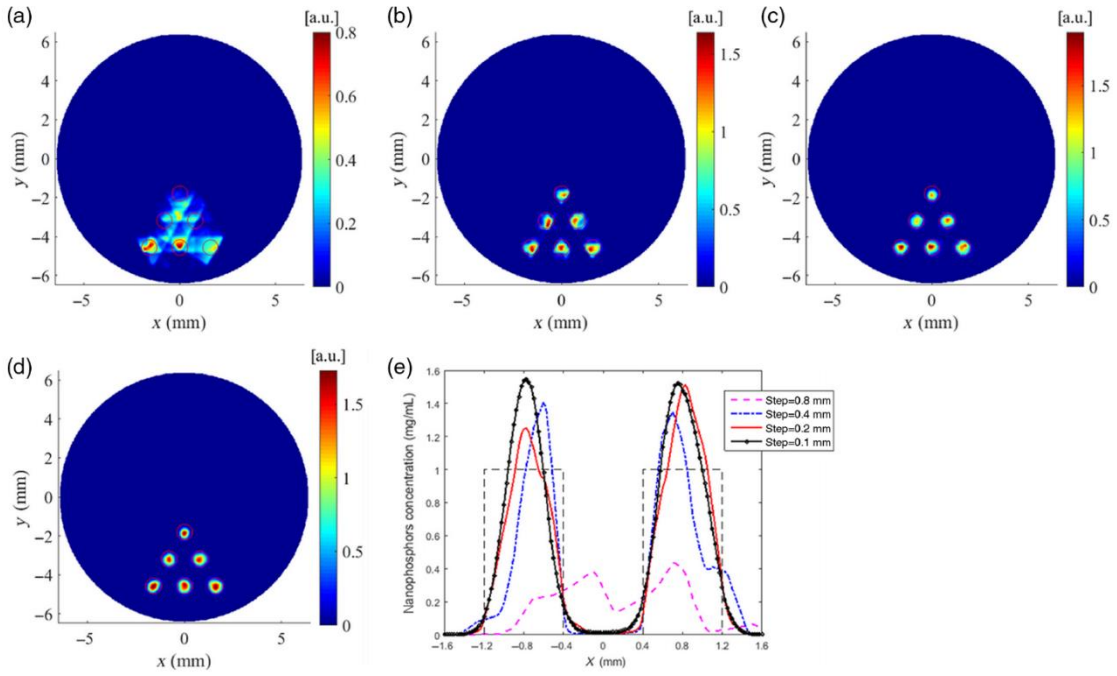

Figure 4.4. Reconstructed XLCT images for the simulations of phantom A with different scanning step sizes: (a) 0.8 mm, (b) 0.4 mm, (c) 0.2 mm, and (d) 0.1 mm. (e) Intensity profiles along the center line of the middle row targets of phantom A.

Table 4.2. The quantitative image quality metrics for the simulations of phantom A with different scanning step sizes.

Scan step (mm)	DICE (%)	TSE (%)	SPI	NMSE
0.8	39.7	38.8	0.693	0.602
0.4	83.6	10.9	0.994	0.191
0.2	90.7	5.0	0.995	0.139
0.1	90.6	6.3	0.992	0.132

For the simulations of phantom B, we simulated XLCT scanning with the same scan settings as the previous simulation. Figure 4.5 shows the reconstruction images of phantom B. The six targets were hardly resolved when the scanning step size of 0.8 mm was adopted, as shown in Fig. 4.5(a). When the scanning step size of 0.4 mm, which is smaller than the target diameter, was used, the six targets were easily resolved with better shapes at the correct locations, as shown in Fig. 4.5(b). The quality of the reconstructed images was improved further by decreasing the scanning step size to 0.2 and 0.1 mm, as shown in Figs. 4.5(c) and 4.5(d). Figure 4.5(e) plots the intensity profiles along the center line of the middle row targets in Figs. 4.5(a)– 4.5(d). The quantitative analysis results are listed in Table 4.3, from which we see the improvement of the reconstruction quality such as the shape and location accuracy, target size accuracy, spatial resolution, and reconstruction accuracy when the scanning beam size was reduced. We have also noticed that there are only slight differences in the quantitative analysis results of DICE, SPI, and NMSE when the scanning step size is reduced from 0.2 to 0.1 mm.

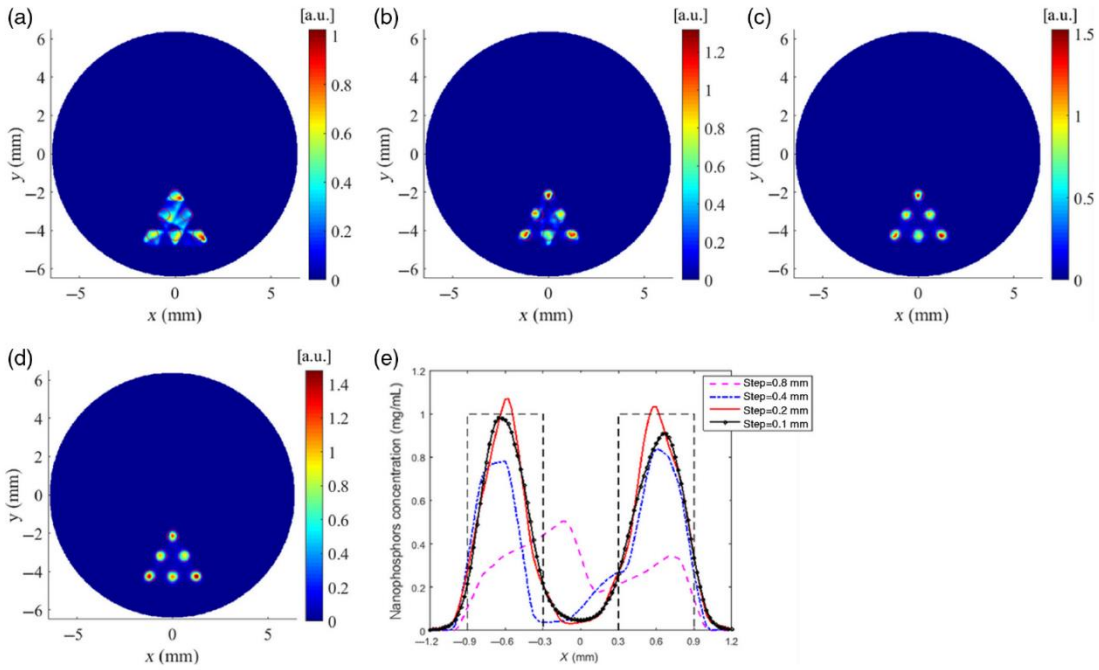

Figure 4.5. Reconstructed XLCT images for the simulations of phantom B with different scanning step sizes: (a) 0.8 mm, (b) 0.4 mm, (c) 0.2 mm, and (d) 0.1 mm. (e) Intensity profiles along the center line of the middle row targets of phantom B.

Table 4.3. The quantitative image quality metrics for the simulations of phantom B with different scanning step sizes.

Scan step (mm)	DICE (%)	TSE (%)	SPI	NMSE
0.8	55.9	33.0	0.649	0.485
0.4	70.3	22.9	0.954	0.226
0.2	81.7	17.7	0.970	0.159
0.1	80.9	12.9	0.952	0.164

We conducted numerical simulations on phantom C with the same scan settings as the previous simulations. The reconstructed images of phantom C are plotted in Fig. 4.6, from which we can see that all targets could be resolved successfully for the step sizes of 0.2 and 0.1 mm. Intensity profiles along the center line of the middle row targets in Figs. 4.6(a-d) were drawn and displayed in Fig. 4.6(e). The DICE, TSE, SPI, and NMSE of the reconstruction results were calculated and are listed in Table 4.4. As the scanning step size reduced from 0.8 to 0.1 mm, the SPI increased monotonically from 0.836 to 0.924, indicating that the proposed scanning strategy with a smaller scanning step size achieved much better separation of the targets. At the same time, a monotonic improvement of the reconstruction accuracy can be maintained as indicated by the NMSE shown in Table 4.4. The reduction of scanning step size can result in better accuracy of the reconstructed shape and location of targets as indicated by DICE and TSE.

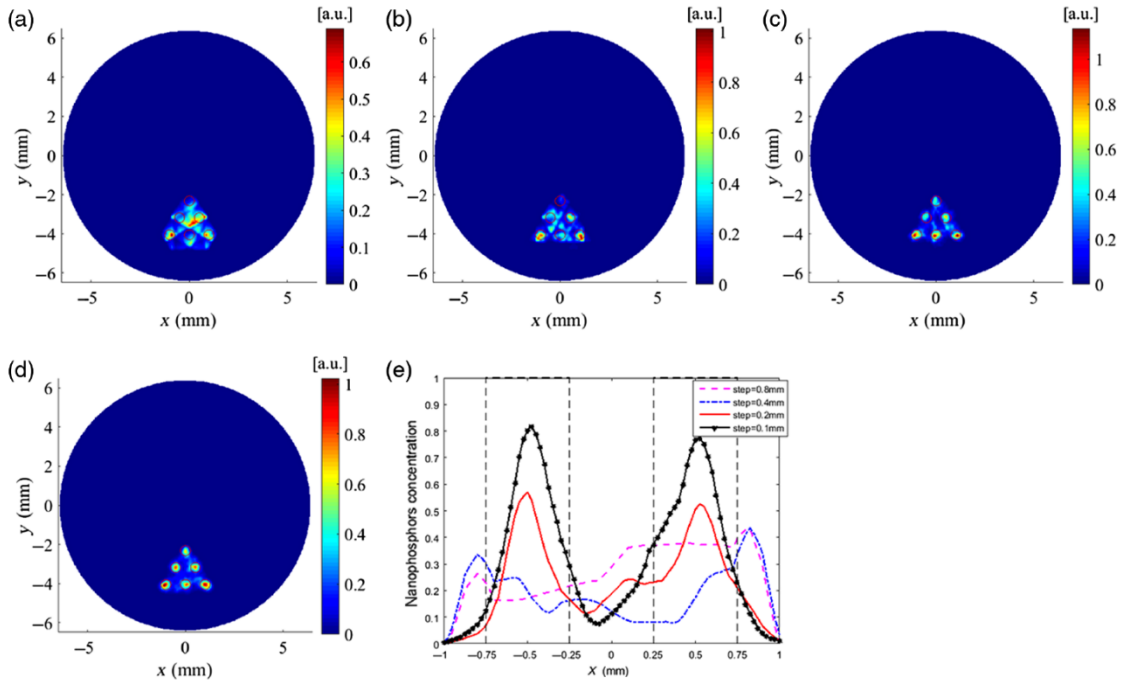

Figure 4.6. Reconstructed XLCT images for the simulations of phantom C with different scanning step sizes: (a) 0.8 mm, (b) 0.4 mm, (c) 0.2 mm, and (d) 0.1 mm. (e) Intensity profiles along the center line of the middle row targets of phantom C.

Table 4.4. The quantitative image quality metrics for the simulations of phantom C with different scanning step sizes.

Scan step (mm)	DICE (%)	TSE (%)	SPI	NMSE
0.8	38.8	59.2	0.836	0.767
0.4	47.0	45.4	0.872	0.601
0.2	58.5	43.3	0.904	0.437
0.1	53.7	36.2	0.924	0.332

To further study the performance limitation of the proposed scanning strategy in resolving targets with a diameter smaller than the x-ray beam width, we simulated XLCT imaging of phantom D, in which both the target diameter and the EtE distance were set to be 0.4 mm, half of the beam diameter. Figure 9 shows the reconstructed XLCT images for this case. From Fig. 4.7, we can see that image quality has improved slightly when the step size decreased. However, the reconstructed XLCT image could not resolve all the six targets even if the step size is reduced to 0.1 mm, which means that the spatial resolution of XLCT imaging depends not only on the scanning step size but also on the x-ray beam size.

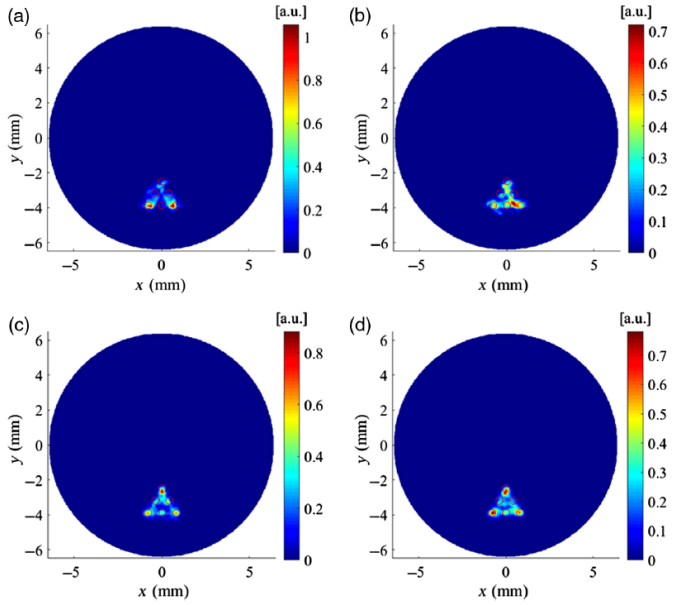

Figure 4.7. Reconstructed XLCT images for the simulations of phantom D with different scanning step sizes: (a) 0.8 mm, (b) 0.4 mm, (c) 0.2 mm, and (d) 0.1 mm.

4.1.5. Phantom experimental results

XLCT image reconstruction was performed from the measurements using a similar approach as the numerical simulations. The L^1 regularized MM algorithm was again utilized with the same FEM, interpolated onto a 50 μm^2 grid. From the XLCT measurement data, we reconstructed three different cases, differing by their linear scanning step sizes: 200 μm (no reduction in step size), 100 μm (two times reduction in step size), and 50 μm (four times reduction in step size) and plotted the results and their corresponding line profile plots for the respective cases in Figs. 4.8 and 4.9. The profile positions used are shown in Figs. 4.8(d-f) where the blue line shows the horizontal position and the magenta line indicates the vertical line profile position. We also performed quantitative analyses by calculating the DICE, TSE, and SPI, as shown in Table 4.5. The true target locations (ground truth) were determined from the microCT image [Fig. 4.3(c)] and are shown by the green circles in the reconstructed XLCT images. Overall, we can see that as the step size decreased, there was an overall improvement in the image quality and the ability to resolve the targets. In addition, the DICE increased from 50.7 to 53.2 and finally to 67.2%; the TSE decreased from 12.5 to 10.9, and finally to 7.8%; and the SPI has an obvious improvement from 0.762 to 0.906, and finally to 0.922, as the step size decreased from 200 to 100 μm and finally to 50 μm (Table 4.5). Overall, our XLCT image reconstruction successfully validates the improvement from our proposed scanning strategy.

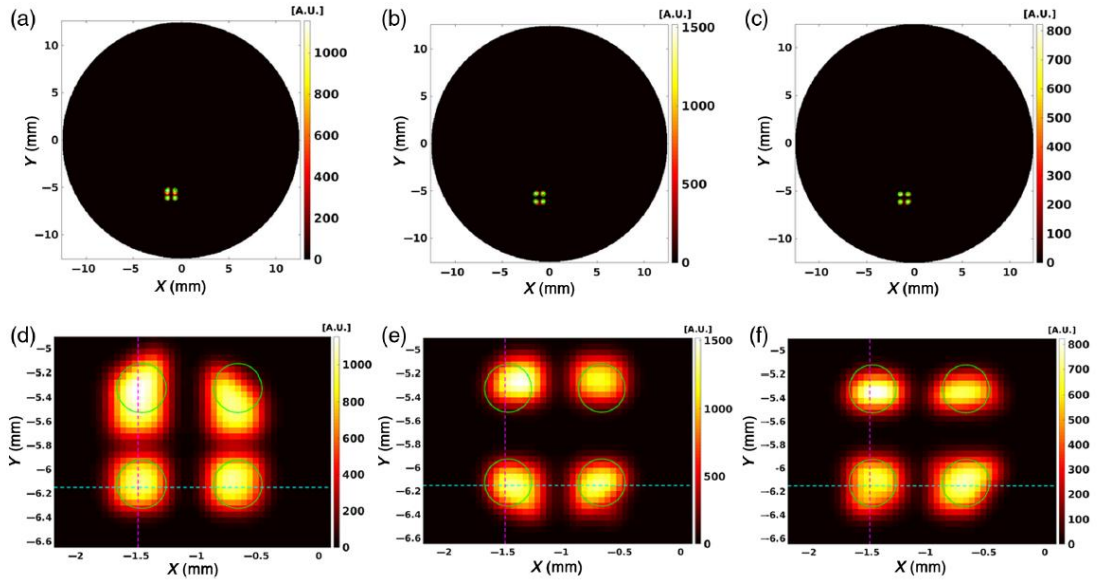

Figure 4.8. Reconstructed XLCT images and the zoomed-in target regions from the phantom experiment for the different cases. (a) No step size reduction. (b) 2× step size reduction. (c) 4× step size reduction. (d) Zoomed-in target region from (a). (e) Zoomed-in target region from (b). (f) Zoomed-in target region from (c). The green circles represent the true target positions obtained from the microCT scan.

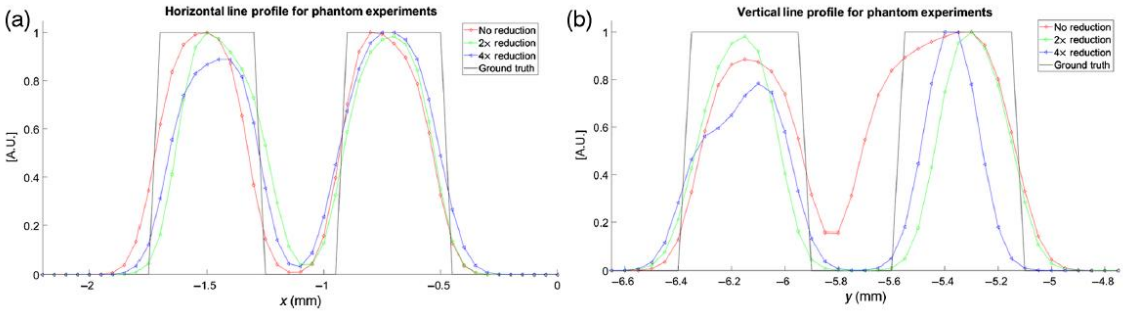

Figure 4.9. Intensity profile plots corresponding to the line positions shown in Figs. 4.8(d-f). (a) Horizontal line profile across bottom two targets. (b) Vertical line profile across left two targets. The intensities are normalized individually to their own line intensities.

Table 4.5. The quantitative image quality metrics of the XLCT-reconstructed images for the phantom experiment.

Case	DICE (%) (Bottom Targets)	TSE (%)	SPI
No Step Reduction (200 μm step size)	50.7	12.5	0.762
2× step reduction (100 μm step size)	53.2	10.9	0.906
4× step reduction (50 μm step size)	67.2	7.8	0.922

4.1.6. Discussions and conclusions

State-of-the-art high-resolution imaging techniques are a driving force behind current biomedical science. Among such, microscopic XLCT imaging stands out as it has the potential to obtain both high sensitivity and spatial resolution. However, its high spatial resolution capacity has not been fully implemented yet. According to previous studies, the spatial resolution limit of XLCT is generally believed to be determined by the beam aperture size. Therefore, generation of superfine x-ray beams, such as superfine collimated x-ray beams imaging (Section 2.1) and focused x-ray beams imaging (Section 2.3), is generally thought to be the only way to improve the spatial resolution of XLCT imaging. However, both methods for generating superfine beams have their own shortcomings. In this study, a scanning strategy, in which the scanning step size is reduced to be less than the x-ray beam size, was proposed to break the spatial resolution limit of the traditional narrow x-ray beam-based XLCT system.

The numerical simulations have demonstrated that the proposed scanning strategy of a smaller step size can achieve better results in the DICE, TSE, and SPI than the traditional one where the step size was equal to the x-ray beam diameter (Section 4.1.4). We have found that targets can be resolved successfully with the proposed scanning strategy when the target size and the EtE distance between targets are smaller than the beam width. We have also conducted XLCT simulations using phantoms with a smaller EtE distance. The first phantom was similar to phantom B except the different EtE distance which was changed from 0.7 to 0.2 mm with an interval of 0.1 mm. The second phantom was similar to phantom C except the different EtE distance which was changed from 0.6 to 0.3 mm with an interval of 0.1 mm. In these numerical studies, the diameter of x-ray beams and the linear scan step size were fixed as 0.8 and 0.1 mm, respectively. With the smaller EtE distance, it is more challenging to reconstruct all targets. However, the proposed scanning strategy has reconstructed all the targets successfully for these cases, while the previously reported scanning method with the same beam size and scanning step size could not resolve all the targets for these cases with much smaller EtE distance than the beam size. These reconstructed XLCT images and detailed analysis are not included in this study for simplicity. These findings help to extend the theory that the spatial resolution of XLCT imaging is determined by not only the x-ray beam size but also the scanning step size. The numerical simulations have demonstrated that our proposed method was also stable and robust against noises. The results of the phantom experiment (Section 4.1.5) have also further validated that the proposed scanning strategy can achieve better results in XLCT image reconstruction.

Certainly, there is an upper bound of spatial resolution improvement by reducing the scanning step size. As shown in the numerical simulation study of phantom D, XLCT could not resolve all the six targets when the scanning step size was reduced to 0.1 mm, because the x-ray beam diameter was 0.8 mm, which was larger than the target diameter of 0.4 mm. From this study, we know that the spatial resolution of XLCT imaging depends

both on the x-ray beam size and the scanning step size. To further investigate the relationship between the XLCT-reconstructed image quality and our proposed method, we have plotted the relative dependence of the four image quality metrics as a function of the x-ray beam size and the scanning step size for different ratios of the x-ray beam size to target diameter (beam/target) in Fig. 4.10, for the successful numerical simulation cases (phantoms A to C). For each setting of the beam/target ratio, we can see that the reconstructed XLCT image quality has a significant improvement as the ratio of the beam size to step size increased from 1 to 4 with increments in both DICE and SPI and decrements in TSE and NMSE. When the beam size/step size ratio is increased to 8, there are no significant changes in the XLCT image quality. Based on Fig. 4.10, our results currently demonstrate that the ideal step size in consideration of the image enhancement and measurement time should be ¼ of the x-ray beam size. Also, when the beam size/step size is larger than 2, the reconstructed image quality increases as the ratio of beam size to target diameter decreases. Therefore, the ideal beam size should be as small as possible according to the trade-off of the spatial resolution and the measurement time.

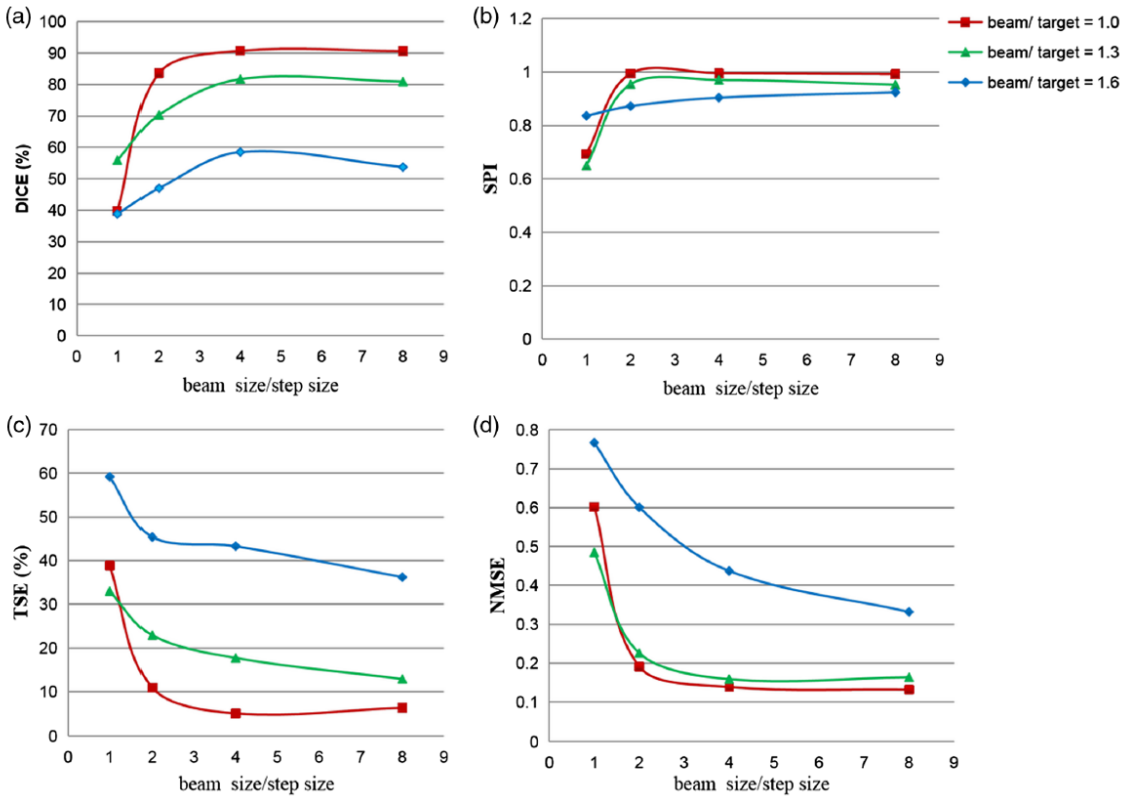

Figure 4.10. The relative dependence of four XLCT image quality evaluation criteria (DICE, SPI, TSE, and NMSE) as a function of beam size/step size in terms of different cases of beam size/target diameter. (a) DICE, (b) SPI, (c) TSE, and (d) NMSE.

We have shown that XLCT imaging with reduced scanning step size can reach a better spatial resolution. However, the reduced step size-based scanning strategy needs more scan steps to cover the same field of view as before, which means more measurement

time is required with the current configuration. To overcome this problem of long scanning time, we used a highly sensitive PMT and a focused x-ray beam with high x-ray intensity to reduce the measurement time per scan step. The current measurement time with the step size of 50 μm was 6 × 520 × 10 ms or 31.2 s, if neglecting the stage movement time. The measurement time can be further reduced to make it more suitable for practical use. One possible way is incorporation of the pre-acquired permissible region of the targets into the scanning configuration to reduce the scanning area and improve the scanning efficiency. The permissible region strategy has been adopted in a cone beam-based XLCT imaging [92].

It is worth noting that we have used four detector fibers in our numerical simulations studies and only one detector fiber in our experimental imaging system. Both studies with either one detector fiber or four detector fibers have verified the efficacy of the proposed method. Currently, we only have one PMT measurement unit in our lab. We are building the next generation of XLCT imaging system (Chapter 5), in which we plan to use four fiber bundles with four PMT detection units [61, 62].

In previous work, we have performed a sensitivity study of XLCT (Chapter 3) under the traditional scanning strategy. In this study, we do not expect the sensitivity to be reduced because other imaging parameters were kept the same as before, except the reduced scanning step size. The sensitivity of the proposed approach should be studied further in the future.

In summary, we have performed four sets of numerical simulations and one set of phantom experiments to validate the proposed scanning scheme of narrow beam based XLCT imaging. Our results have demonstrated that the scanning scheme can improve the spatial resolution substantially, compared to previous methods. In particular, the improvement is up to two times from 0.8 to 0.4 mm for the case with an x-ray beam diameter of 0.8 mm.

4.2. Experimental High-Resolution XLCT Imaging

Our current focused x-ray beam based XLCT imaging system (Section 2.3), can generate x-ray photons with a focal diameter of about 100 μm. Within the section of the x-ray beam that scans the object (mouse-sized object), the x-ray beam diameter has a max width of about 150 μm. Based off studies conducted in Section 2.1, we should be able to resolve targets with edge-to-edge (EtE) distances of 150 μm as well. In the past, it has been a challenge to find or fabricate high-resolution targets of this size for XLCT imaging, thus we have only previously been able to demonstrate a spatial resolution of 0.8 mm (0.4 mm EtE distance). Recently, we have been able to obtain glass capillary tube targets of 150 μm size, which will then allow us now to experimentally demonstrate and verify the high-resolution capabilities of our focused x-ray beam based XLCT imaging system, which will be performed in this following work.

4.2.1. High-resolution XLCT experimental set-up

We have performed two phantom experiments using two sets of targets of different sizes in order to validate the high-resolution imaging capabilities of our XLCT experimental set-up. Fig. 4.11 shows the overall phantom geometry used in this study. Cylindrical phantoms of 12 mm diameter and 20 mm height were created and composed of 1% intralipid, 2% agar, and water. Two sets of high-resolution targets were created using high-precision glass capillary tubes (Drummond Scientific) with O.D./I.D. of 0.40/0.20 mm and 0.30/0.15 mm, respectively. The I.D. of the capillary tubes is considered as the actual target diameter. We then mixed 10 mg/mL of GOS:Eu^{3+} (UKL63/UF-R1, Phosphor Tech. Ltd.) into a similar background solution as the phantom and injected the solution into the capillary tube targets before embedding them into the phantoms as shown in Fig. 4.11(b). One phantom was embedded with two targets of 0.20 mm diameter and the other phantom was embedded with the 0.15 mm diameter targets. For each phantom, the edge-to-edge (EtE) distance of the two embedded targets was the same as the target diameters (i.e. 0.20 mm and 0.15 mm EtE distances respectively).

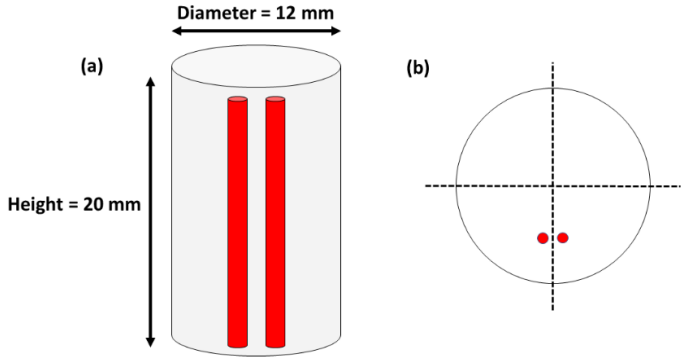

Figure 4.11. Schematic phantom geometry for high-resolution XLCT imaging experiments. (a) Overall phantom geometry; (b) Top-view showing embedded target location.

We performed the XLCT scans inside of our focused x-ray beam based XLCT imaging described in Section 2.3.1. Figure 4.12 shows an updated CAD model of the imaging system. For our XLCT scans, we operated the x-ray tube at a setting of 30 kV and 0.5 mA (15 W) and took measurements from 6 angular projections (30°/projection) using 80 linear steps with a step size of 0.15 mm to traverse the whole phantom. The PMT was operated with a control voltage of 0.750 V and the oscilloscope was set to acquire or save 100 milliseconds (ms) of data from the PMT at each step. After the XLCT scan, we immediately performed a microCT scan inside of our dedicated microCT scanner described in Section 3.1.1. in order to determine the ground-truth location of the embedded targets for each phantom. We acquired microCT projection images from 180 projections using an angular step size of 2°. MicroCT image reconstruction was performed in MATLAB using the filtered back-projection (FBP) algorithm with a Shepp-Logan filter. For XLCT imaging, image reconstruction was performed as before. The images of the scanned section were reconstructed using an optical photon propagation model (radiative transport

equation) inside turbid media, which also included information such as the x-ray beam's known size and location to aid in the reconstruction (Section 1.3.4.). Here, we utilized the L^1 regularized MM framework to reconstruct our XLCT images.

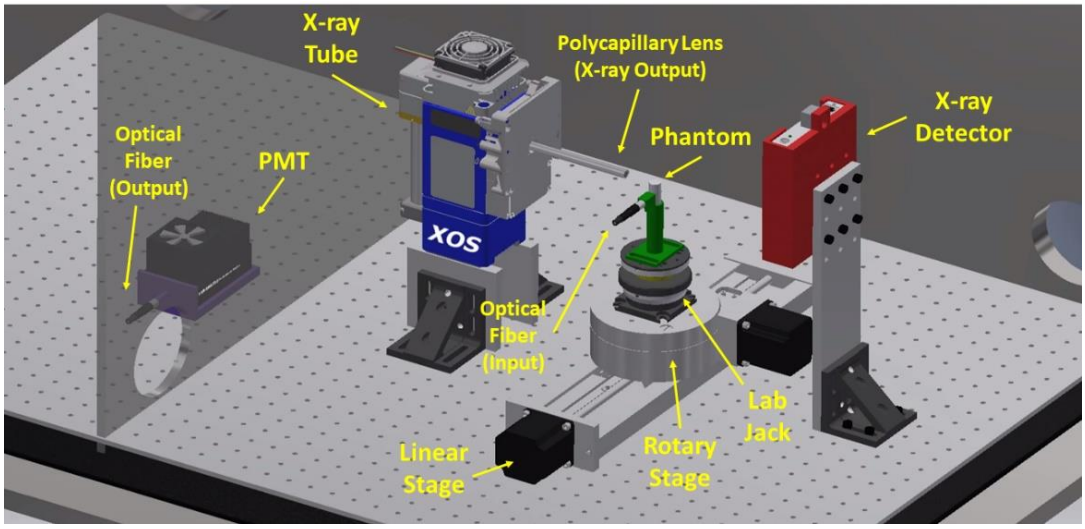

Figure 4.12. CAD model of the focused x-ray beam based XLCT imaging system.

4.2.2. High-resolution XLCT imaging results

Fig. 4.13 shows a single transverse slice from the microCT reconstruction corresponding to the XLCT scan section for both phantoms. Fig. 4.13(a) shows the phantom embedded with two 0.40/0.20 mm (O.D./I.D.) capillary tube targets and Fig. 4.13(b) shows the case with the 0.30/0.15 mm capillary tube targets. Using the microCT image, the center of the phantom was determined, and then the distance from the phantom center to the target centers was used as the ground-truth locations.

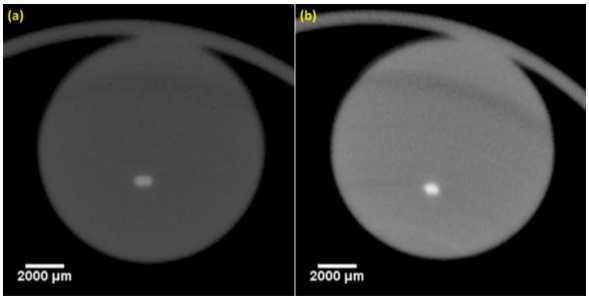

Figure 4.13. microCT image of phantoms used in high-resolution XLCT imaging experiments. (a) Phantom embedded with 0.20 mm diameter targets; (b) Phantom embedded with 0.15 mm diameter targets.

For the XLCT reconstruction, the scanned section was interpolated onto a 2D grid with a pixel size of 25 µm^2. The system matrix was interpolated onto the grid from the system matrix calculated on a finite element mesh. The results of the XLCT reconstruction for the phantom embedded with two 0.20 mm diameter targets are shown in Fig. 4.14. Fig. 4.14(a) shows the raw reconstructed image from the acquired data and Fig. 4.14(b) plots a

zoom in on the target region (shown as a yellow box in Fig. 4.14(a)) with the true target locations (acquired from Fig. 4.13(a)) shown as green circles. We can see that two targets have been clearly resolved with good shape and location accuracy. We have calculated the DICE similarity coefficient for this reconstruction to be 78.5%. To analyze the reconstruction further, a normalized line profile plot through the center of the two targets (blue dashed line in Fig. 4.14(b)) is shown in Fig. 4.14(c) where the true target profile is indicated by a dashed black line and the reconstruction is shown as the red line. We can see good agreement between the two profile plots.

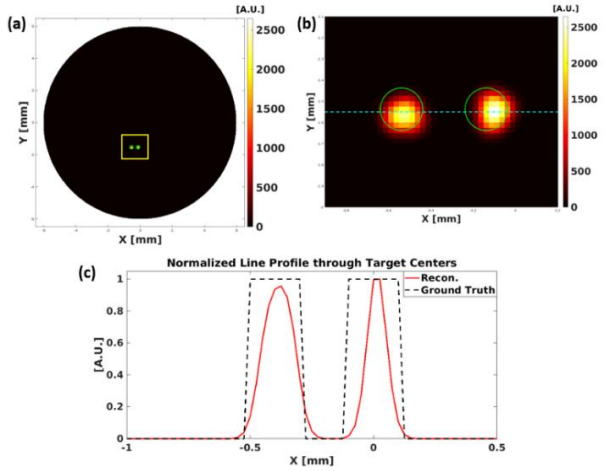

Figure 4.14. XLCT reconstruction of phantom embedded with 0.2 mm (200 µm) diameter targets. (a) XLCT reconstructed image; (b) Zoomed-in target region (yellow box in (a)); (c) Normalized line intensity plot (blue line in (b)).

The results of the XLCT scan of the phantom embedded with two 0.15 mm diameter targets is shown in Fig. 4.15 as before. Again, the two embedded targets were successfully resolved, and the DICE was calculated as 55.6%. Based on the normalized profile plot shown in Fig. 4.15(c), the two targets have been reconstructed very well.

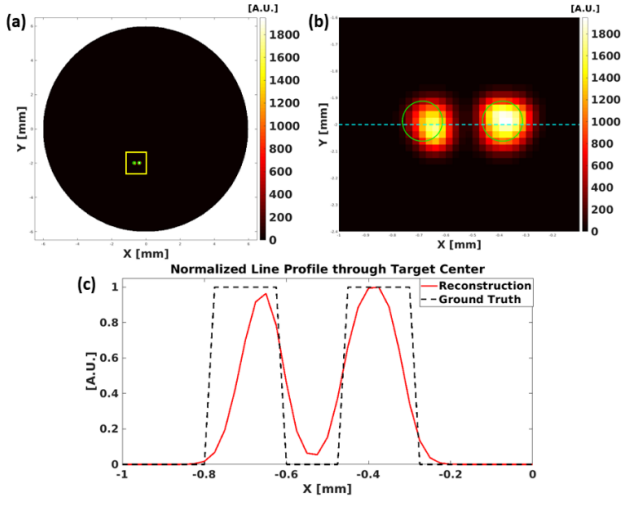

Figure 4.15. XLCT reconstruction of phantom embedded with 0.15 mm (150 µm) diameter targets. (a) XLCT reconstructed image; (b) Zoomed-in target region (yellow box in (a)); (c) Normalized line intensity plot (blue line in (b)).

4.2.3. Discussion and conclusions

In this work, we have performed high-resolution focused x-ray beam based XLCT imaging experiments and have demonstrated that our imaging system described in Section 2.3.1 can resolve two targets embedded in turbid media with EtE distances of 0.15 mm or 150 μm. This is an improvement from our previous experiments where we could only demonstrate imaging with targets embedded with 400 μm EtE distances. For the XLCT reconstruction of the first phantom embedded with the 200 μm targets (Fig. 4.14), we can see a very clear separation between the two targets which is expected as the focused x-ray beam size is much smaller than the EtE separation. When the target EtE distance decreases to 150 μm, as with the second phantom (Fig. 4.15), we can see that the reconstruction quality slightly degrades, as indicated by the decrease in the DICE coefficient, but the value (55.6%) is still acceptable. We anticipate that we are still able to demonstrate even higher-resolution imaging (less than 150 μm EtE) with this system, however, smaller targets are not possible to fabricate with our current resources. With our future small-animal dedicated focused x-ray luminescence tomography (FXLT) imaging system to be described in Chapter 5, we will have even higher spatial-resolution capabilities for XLCT imaging since the x-ray beam size is approximately one-half the size of the beam used in this study.

In summary, in this work we have performed high-resolution XLCT imaging experiments of cylindrical phantoms embedded with two targets with EtE distances as small as 150 μm and have validated that the targets can be successfully resolved. Thus, with our current focused x-ray beam based XLCT imaging set-up, we can currently obtain a spatial resolution of 300 μm. We anticipate that we can still obtain higher spatial resolution, especially if we use a smaller x-ray beam size or incorporate a reduced scanning step size as in Section 4.1. The proposed high spatial-resolution XLCT imaging system with such unique imaging capabilities would have many applications, such as for studying tumor microenvironment (e.g. oxygenation) or structure.

CHAPTER 5

FOCUSED X-RAY LUMINESCENCE TOMOGRAPHY (FXLT) FOR SMALL ANIMAL IMAGING

5.1. Focused X-ray Luminescence Tomography: *ex vivo* mouse studies

High-resolution imaging modalities play an important role for advancing biomedical sciences. Particularly, XLCT imaging has emerged as an attractive tool with various applications, for example in small-animal molecular imaging. With our experimental focused x-ray beam based XLCT imaging system, we have previously successfully demonstrated the ability for imaging mouse-sized objects (cylindrical phantoms). In our first experiments, we performed XLCT imaging of a mouse-sized object in about 12.5 minutes, which is an improvement from the collimated x-ray beam based XLCT, while also still obtaining a sub-millimeter spatial resolution. In this work, we performed XLCT imaging using a dramatically reduced imaging time of 10 ms per linear scan step versus the previous 1 second per linear scan step. We also, for the first time, performed imaging with our focused x-ray beam based XLCT imaging system with a euthanized mouse embedded with a capillary tube filled with phosphor particles.

5.1.1. Experimental set-up for euthanized mouse imaging

For the XLCT imaging experiments, we used the same imaging system described in Section 2.3.1, except with a lab-made specimen holder designed to hold the mouse vertical and stationery during the measurements. The holder was designed with CAD and then 3D printed to fit our XLCT imaging system as shown in Fig. 5.1. As seen in Fig. 5.1(a), the mount was comprised of three parts (labeled 1, 2, and 3). The mouse was fixed with part 1, using strings to securely tie down the mouse so it did not move using the top and bottom rails. In addition, three holes were included in the center section of part 1 that were used for the optical fiber bundle to connect and detect the emitted optical photons. Once the mouse was secured to part 1, it was placed into part 2 which was fixed to the manual lab jack in our XLCT imaging system to provide rigid support from the base. Finally, since the optical fiber cable was long and required additional support, part 3 was used to provide another rigid support structure for the cable while being easily added and removed so that the mount was able to be laid flat, particularly for microCT imaging since our microCT scanner required the imaged object to be laid down flat on the imaging stage. The entire assembled set-up in our XLCT imaging system is shown in Fig. 5.1(b).

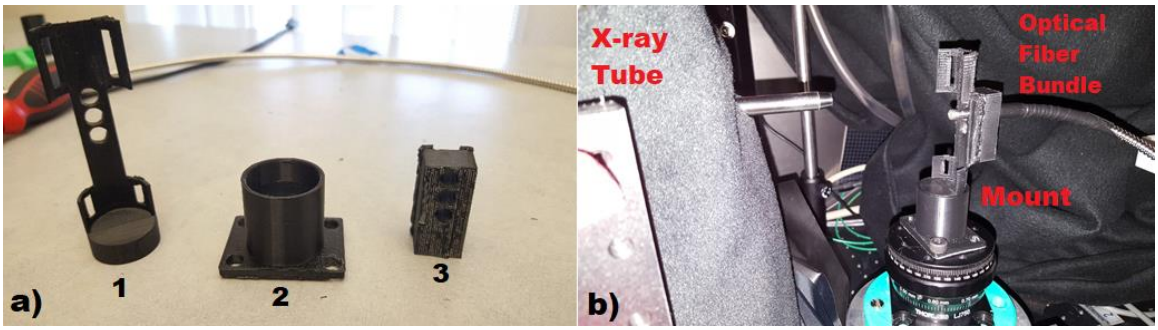

Figure 5.1. Lab-made mount for mouse/phantom and fiber bundle. a) The mount fully disassembled into three parts labeled 1, 2 and 3; b) The mount set-up in the XLCT imaging system.

To first verify the new stage set-up, we first performed a simple phantom experiment using a long cylindrical phantom, whose geometry is shown in Fig. 5.2(a). The phantom had a diameter of 25 mm and height of 90 mm and was embedded off-center with a capillary tube of 2.0 mm outer diameter and 1.0 mm inner diameter (yellow object) as seen in Fig. 5.2(b) (target size: 1.0 mm). The background phantom was comprised of 1% intralipid, 2% agar and the capillary tube was filled with 10 mg/mL of GOS:Eu^{3+} microphosphors (UKL63/UF-R1, Phosphor Tech. Ltd.) in a similar background solution. Once completely solidified, the object was secured onto the lab-made mount and then placed inside of the XLCT system for imaging as seen in Fig. 5.3. The fiber bundle tip was placed such that it contacted the surface of the object. We performed XLCT imaging of a single transverse section using x-ray tube settings of 30 kV and 0.5 mA and using only 10 msec of XLCT data collection from the oscilloscope. To scan the phantom, we acquired 125 linear steps of 0.2 mm step size and took measurements from 6 angular projections (30°/projection). The x-ray beam location and scan depth were confirmed using the x-ray detector. During the experiments, the PMT was operated at a control voltage of 0.750 V and the amplifier gain was 25. Immediately following the XLCT scan, we performed a microCT scan of the object inside of our lab-made microCT system. Based on this current set-up the measurement time (neglecting x-ray detector exposure and stage movement) is (6 projections × 125 steps × 10 msec) or 7.5 secs.

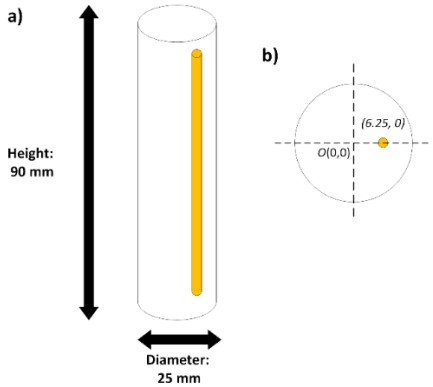

Figure 5.2. Geometry of phantom used for XLCT imaging studies where the target is represented by a yellow cylinder. a) Overall phantom geometry; b) Coordinates of target.

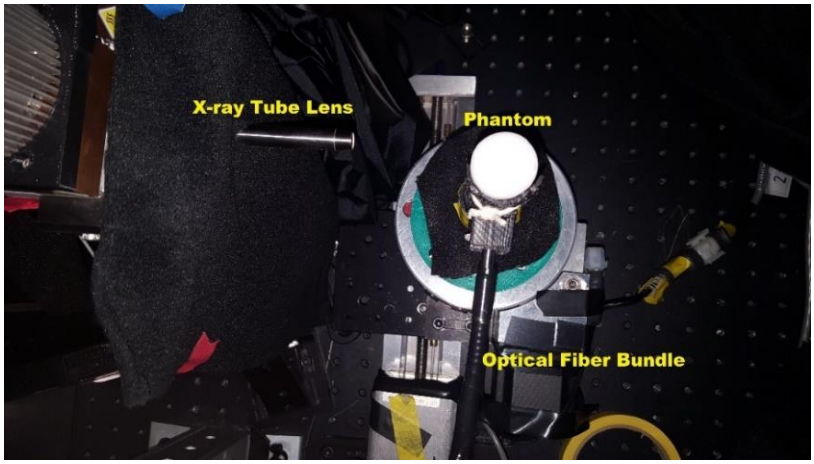

Figure 5.3. Phantom set-up inside the XLCT imaging system.

After the phantom experiment, we then performed XLCT imaging of a euthanized nude mouse. The mouse used in this study was cared for and euthanized under federally approved protocols by UC Merced's Department of Animal Research Services' vivarium center. The mouse used in this imaging study was a 30.696 grams nude male mouse euthanized by CO_2 inhalation. The measured trunk diameter was approximately 24 mm along the center sagittal plane and 25 mm along the transverse plane. A target was prepared by making a solution composed of 1% intralipid, 2% agar, and 10 mg/mL commercial GOS:Eu^{3+} microphosphors (same as the previous phantom experiment) then injecting the solution into a capillary tube to create a 1.0 mm diameter target. Figure 5.4(a) shows a photography of the mouse and the capillary tube target. The capillary tube was inserted into the mouse via the esophagus following the euthanasia and the target's location was verified by performing a microCT scan immediately after the XLCT scan. After the target was inserted, the mouse was mounted in the lab-made stage, as seen in Fig. 5.4(b) and then placed into the XLCT system for imaging as seen below in Fig. 5.5. For the XLCT scan, we used the same parameters as the previous phantom XLCT scan and then followed-up the scan immediately with a microCT scan.

Figure 5.4. (a) Euthanized mouse and capillary tube target used for imaging studies; (b) Euthanized mouse mounted to specimen holder.

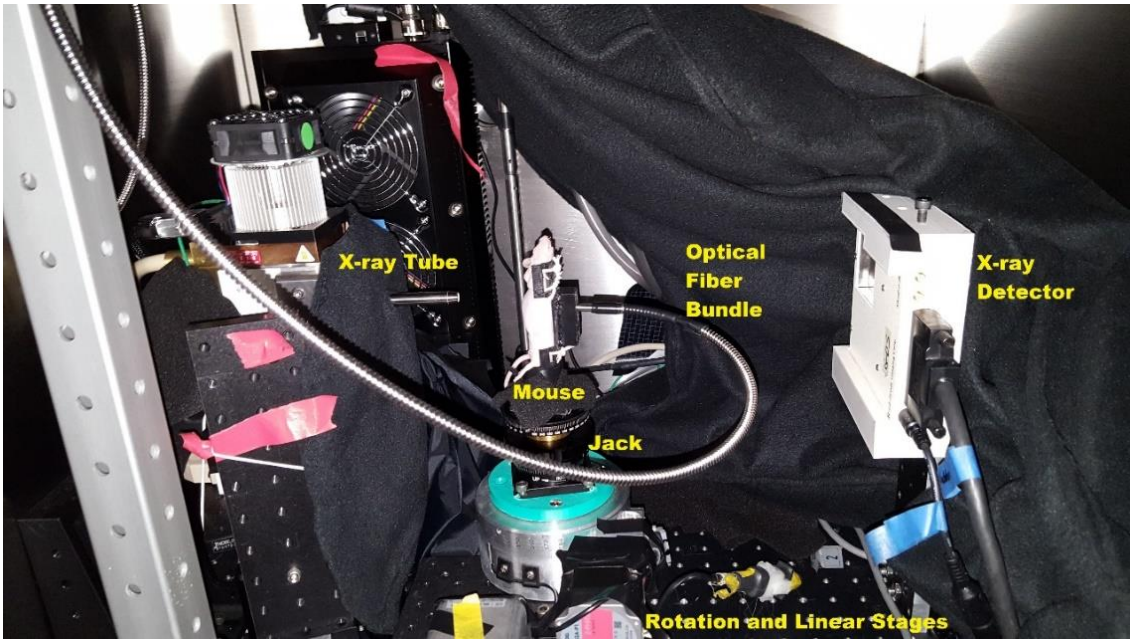

Figure 5.5. XLCT set-up for the euthanized mice imaging. The scanned section was just above the optical fiber bundle.

5.1.2. XLCT experimental imaging results

Fig. 5.6 below plots a single slice of the microCT image corresponding to the scanned section that was used for XLCT imaging. The actual geometry of the phantom including the coordinates of the target is shown in Fig. 5.6(b) from which we can see that the target was implanted at a location of (3.30, 1.80) mm from the origin (center) of the phantom. We then performed an XLCT reconstruction from the XLCT measurements by using the L^1 regularized method in the MM reconstruction framework to solve the inverse problem. For the XLCT reconstruction, the scanned section was interpolated onto a 2D grid with a pixel size of 50 μm^2. The system matrix was interpolated onto the grid from the system matrix calculated on a finite-element mesh. The XLCT reconstructed image is shown in Fig. 5.7 where the green circle indicates the true target location, obtained from the microCT image (Fig. 5.6(b)). A zoom-in of the target region is displayed in Fig. 5.7(b) from which we can see that the target was reconstructed with a very good shape and location accuracy. To further analyze the reconstructed image, a line profile (position shown in Fig. 5.8(a)) is drawn and shown in Fig. 5.8(b) where the dashed black line represents ground truth and the reconstructed target shown with the solid red line from which we can see a good agreement between both profiles. Using the full width ten percent maximum (FWTM), we calculated the reconstructed target size to be 1.200 mm (20% target size error (TSE)) and DICE similarity coefficient of 83.16%.

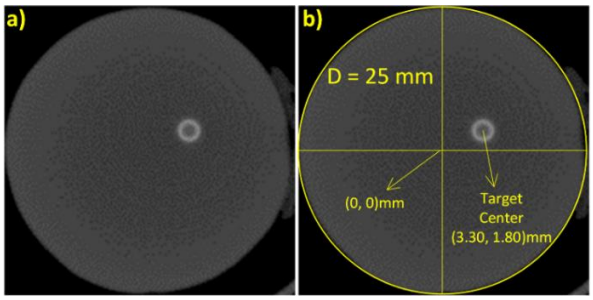

Figure 5.6. Reconstructed microCT image of the cylindrical phantom. a) Reconstructed microCT image; b) Reconstructed microCT image with target coordinates.

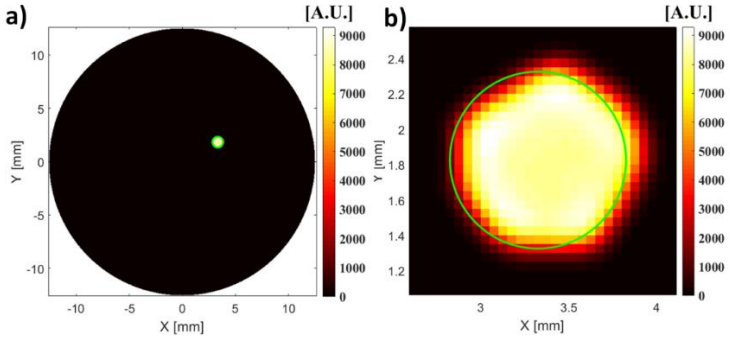

Figure 5.7. Reconstructed XLCT image of the cylindrical phantom. a) Overall reconstructed XLCT image; b) Zoomed-in target region. The green circle shows the true target location.

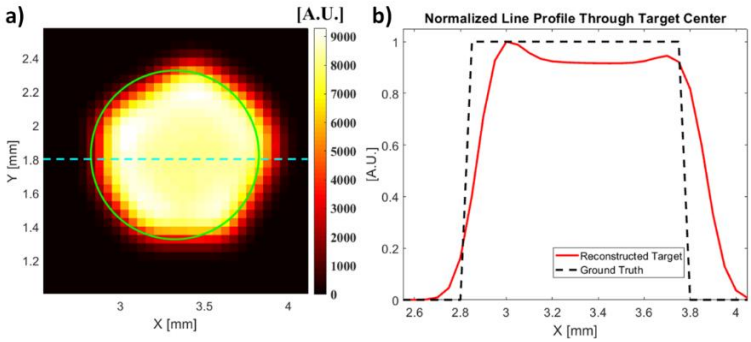

Figure 5.8. Line Profile for the reconstructed XLCT image of the cylindrical phantom. a) Zoomed-in target region with the blue line indicating the profile position; b) The profile plots across the target.

Next, the results of the euthanized mice experiment are shown in Figs. 5.9-5.11, similar to the previous phantom experiment. The reconstructed microCT image of the scanned section is shown in Fig. 5.9. We then overlaid a 25 mm cylinder on top of the reconstructed image (Fig. 5.9(b)) and then plotted the coordinates of the implanted capillary tube as (3.60, 0.45) mm from the center of the circle. During the XLCT reconstruction, we assumed that the mouse was perfectly cylindrical (although it is not) to simplify the reconstruction and performed XLCT reconstruction using the same settings as the phantom experiment. The XLCT reconstructed image is shown in Fig. 5.10 with a zoom-in of the target region in Fig. 5.10(b). The dashed green circle represents the target

location again obtained from the microCT scan. Afterwards, we again draw a line profile through the target center (Fig. 5.11(a)) and then draw the corresponding line profile (Fig. 5.11(b)) from which we again can see a good agreement in the shape and size. Lastly, using the FWTM, the target size was calculated to be 0.950 mm (5% TSE) and the DICE was 92.11% indicating an accurate XLCT reconstruction.

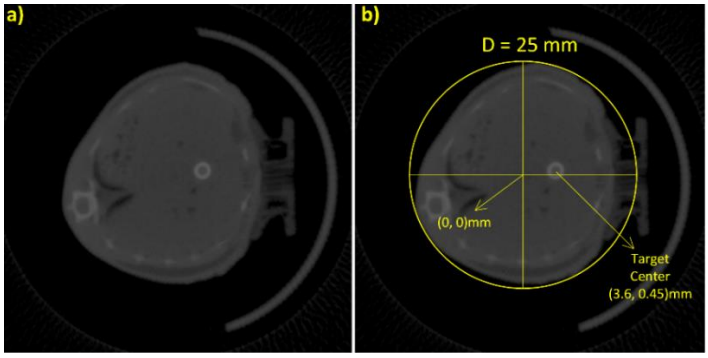

Figure 5.9. Reconstructed microCT image of the euthanized mouse. a) Reconstructed microCT image; b) Reconstructed microCT image with the target coordinates.

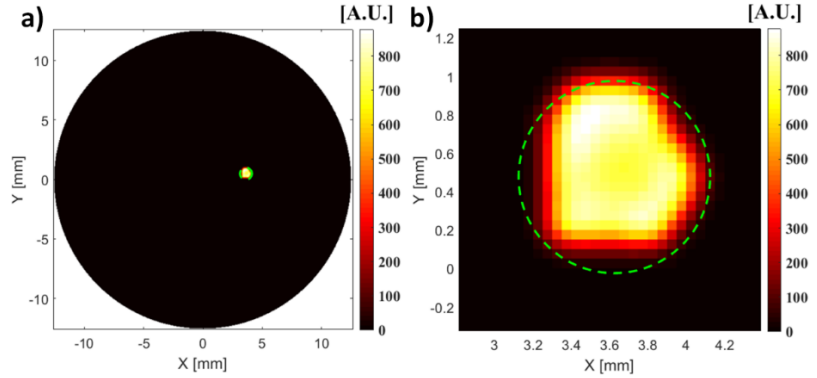

Figure 5.10. Reconstructed XLCT image of the euthanized mouse. a) Overall reconstructed XLCT image; b) Zoomed-in target region. The green circle shows the true target location.

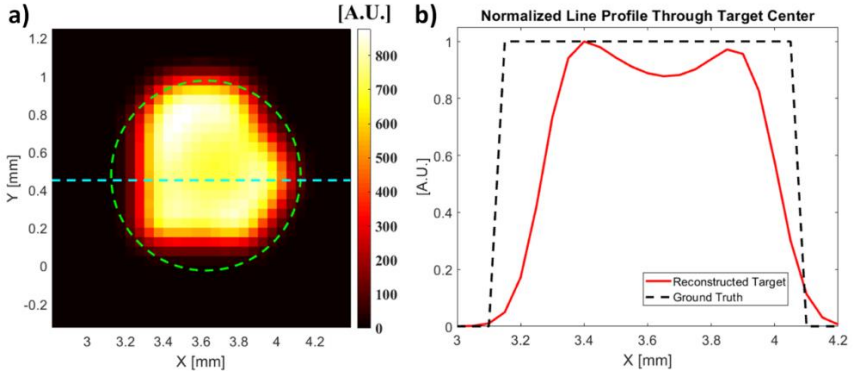

Figure 5.11. Line Profile for XLCT reconstruction of imaged mouse. a) Zoomed-in target region with the blue line indicating the profile position; b) The profile plots across the target.

5.1.3. Discussion and conclusions

In this study we have performed both phantom and euthanized mice XLCT imaging using our focused x-ray beam based XLCT imaging system and have demonstrated that the measurement time could be reduced dramatically, from 12.5 mins in [9] to 7.5 secs (neglecting the stage movement and x-ray detector exposure times). In our phantom experiment, we demonstrated that our XLCT set-up, including the lab-made mount, can perform XLCT imaging of a mouse sized object with tissue-mimicking properties using a reduced optical measurement time of 10 msec per linear step, compared to our previously published study in Section 2.3 where we used 1 sec per linear step, a 100 times reduction in the measurement time. Based on our phantom XLCT reconstruction (Figs. 5.7-5.8), we can see that the target was reconstructed with an excellent shape and location accuracy, even with the reduced optical measurement time. It is also worth noting that the sensitivity (and measurement time required) is dependent upon several factors, including the target concentration, which was 10 mg/mL in this study. Next, we performed XLCT imaging of a euthanized nude and showed the results of the mouse experiments in Figs. 5.9-5.11. After measuring the trunk portion of the mouse to be imaged and from the microCT reconstruction, we decided to perform the XLCT reconstruction of the scanned section using a 25 mm circle, which is close to the actual size of the mouse as seen in Fig. 5.9(b). From the reconstructed images of the euthanized mouse, we can see that the target was successfully reconstructed with a good shape and location accuracy, as seen in the line profile plot (Fig. 5.11(b)). In addition, the reconstructed target size was 0.950 mm giving us only a 5% TSE. Also, the DICE was 92.106% which is even higher than in the phantom experiment and indicates a very high similarity between the reconstructed target and the real target. Even without the homogeneity of tissues and likely higher optical absorption and scattering than with our phantom, there is still enough optical photons that reach the object surface and then to the detection unit using a reduced measurement time of 10 msec per linear step. In the future, we would like to be able to generate a more accurate mesh to be used in our XLCT reconstruction rather than assuming that the mouse was cylindrical, as in this study. We could include a digi-warp algorithm [93] in the future, or other methods to generate a more accurate mesh. In addition, we would like to include a continuous-scan scheme as opposed to the scan-step scheme which was used in this study which can help to reduce the measurement time further.

In summary, we have performed focused x-ray beam based XLCT imaging of both a mouse-sized cylindrical phantom as well as a euthanized mouse, and found that the measurement time, which is of usual concern for the narrow-beam based XLCT imaging, could be dramatically reduced to 7.5 s, a substantial improvement compared with previous studies. In addition, we were able to reconstruct the target with a very good size and location accuracy as seen in the reconstructed XLCT images. In the next section, we designed and built a small-animal dedicated focused x-ray beam based XLCT imaging system that includes a microCT scanner in a single imaging machine which can allow us to perform both imaging (microCT and XLCT) nearly simultaneously and without having

to transfer the object to a separate system for imaging as we did in this study. The planned focused x-ray luminescence tomography (FXLT) imaging system will become a potentially powerful tool for the molecular imaging community.

5.2. Focused X-ray Luminescence Tomography (FXLT) Imaging System for Small Animal Imaging

We have designed several prototype XLCT imaging systems and have demonstrated the unique capabilities of XLCT for obtaining high spatial resolution and high measurement sensitivity. In addition, we have shown the potentials of XLCT imaging for small animal imaging with a euthanized mouse study. In this section, based on all our previous work, we proposed and are building a small animal dedicated focused x-ray luminescence tomography (FXLT) imaging system that also incorporates a microCT scanner. The current state of the proposed system will be described. First, I have designed and constructed a scale 3D model with CAD and discuss the proposed scanning scheme for the system. Then, numerical simulations were performed in order to verify the feasibility of the FXLT imaging. Finally, the current state of the imaging system build is described.

5.2.1. Design of the FXLT scanner and proposed scanning scheme

Figures 5.12 and 5.13 below show the CAD model of our designed FXLT scanner. The imaging system frame is built from extruded T-slotted aluminum bars (80/20 Inc.) and has approximate dimensions of 2.82" × 3.90" × 5.77" (width × length × height). Custom lead-lined stainless-steel panels and door (as seen in Fig. 5.12(a)) were designed and fabricated (BFK Innovation Inc.) and are mounted to the frame to protect from x-ray leakage as well as allowing for the system to be light-tight. The primary imaging system components are fixed onto a custom cut optics board that is mounted onto a heavy-duty ring track (HDRT) (Bishop-Wisecarver) mounted to the imaging system frame (Figs. 5.12(b) and 5.13). The HDRT has a central bore diameter of 650 mm and contains an internal V-track that uses a pinion and shaft system to rotate for different angular projections. We will use a powerful servomotor with a gear-head (SGM7A, Yaskawa) to drive the pinion. As seen in Figs. 5.12b and 5.13, a linear stage is used to position and bring our imaged object into the field-of-view (FOV) of the scanner components that are mounted to the HDRT. First, the object enters the FOV of the microCT scanner. For the microCT scanner, we have an x-ray tube (XTF5011, Oxford Instruments) fixed to an aluminum bracket. Opposite of the x-ray tube, we mount an x-ray detector (Shad-o-Box 1K HS, Teledyne DALSA) to collect our microCT projection images. We also fix the power supply (Shasta Power Supply) to the ring track as well. Following the microCT scan, the object is then positioned into the FOV of the FXLT scanner to perform x-ray optical imaging. Here, we use a powerful focused x-ray tube with polycapillary lens (fleX-Beam, XOS) that has an approximate focal spot size of 49.9 μm (FWHM, Mo-K_α [17.4 keV]) and a photon flux of 2.8×10^7 photons/sec (at 50 keV). The x-ray beam convergence angle is

less than 2 degrees and the beam diameter changes to a maximum of 75 μm within a 10 mm range of the focal spot. The power supply (PCS-50) is fixed and mounted to the ring track. The x-ray tube is fixed onto a heavy-duty precision linear stage (NLS-8, Newmark Systems Inc.) that allows for translational scanning of the focused x-ray beam. Directly opposite of the polycapillary lens, we fix a small scintillator crystal (e.g. Ce: Lu_2SiO_5) that can constantly track the intensity of the focused beam by delivering the signal to a PMT through an optical fiber bundle. This can be used to determine when an object (e.g. Phantom) is in the path of the x-ray beam for boundary determination during image reconstruction. During the FXLT scans, any emitted optical photons that reach the object surface is delivered to an array of four PMTs (H7422-50, Hamamatsu Inc.) by use of two bifurcated liquid-light guides (Series 380, Lumatec) that are optimized for the NIR range (up to 800 nm) with high-efficiency. During the FXLT scans, the light guides are fixed and do not rotate. Before the optical signal is delivered to the PMTs, we can apply a bandpass filter in order to select two wavelengths (up to four) of interest as well which allows for us to perform multiplexed imaging. Then the PMT output signal is further amplified by use of a preamplifier (SR445A, Stanford Research Systems) and then a low-pass filter applied (BLP-10.7+, Cutoff Frequency: 11 MHz, Mini-Circuits) to reduce high-frequency noises before the signal is finally collected by a high-speed digitizer (DTS5730S, CAEN Technologies Inc.) connected to a lab computer. Fig. 5.14 summarizes the scanning scheme of the FXLT scanner schematically.

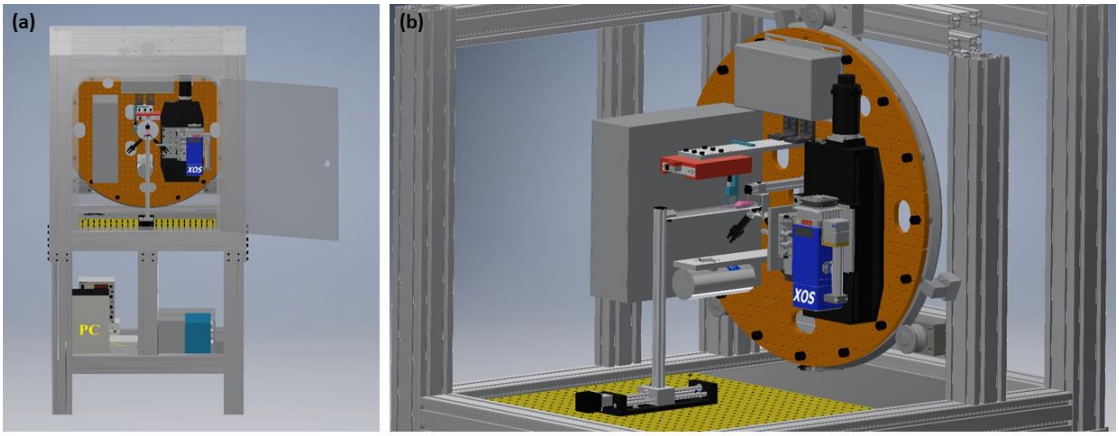

Figure 5.12. CAD model of the designed FXLT Imaging System. (a) Full frontal view with radiation shielding panels and door made transparent; (b) Zoomed-in corner view with radiation panels removed.

As shown in Fig. 5.13, an x-ray tube (XTF5011, Oxford Instruments, 50 kVp and 1 mA) and a flat panel x-ray detector (Shad-o-Box 1K HS, Teledyne Dalsa) are mounted for microCT imaging of the imaged object. Before FXLT imaging, the linear stage places the object in the field of view (FOV) of the microCT that will take measurements at 360 angular projections with an angular step size of 1 degree. After the microCT scan, the linear stage moves the object to the FOV of the FXLT. A filtered back-projection with a Shepp-Logan filter will be used to reconstruct the microCT images.

Our design allows us to have flexibility on the number of angular projections. For the FXLT images, our simulation results have shown that measurements at 6 angular projections are enough to reconstruct complex XLCT images as described in the following section. For each angular projection, we will have a continuous scan for one linear scan in 3 seconds. Thus, the total scan time for each transverse section depends on the angular projection number. For a typical angular projection number of 6, we need less than 1 minute for each transverse section scan if including the rotation time.

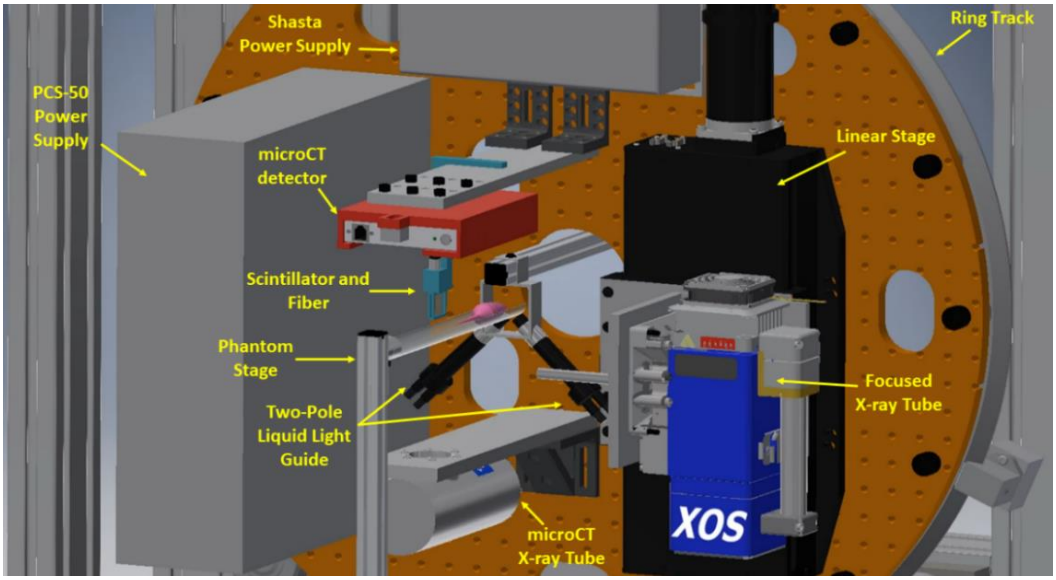

Figure 5.13. Main FXLT imaging components with labels.

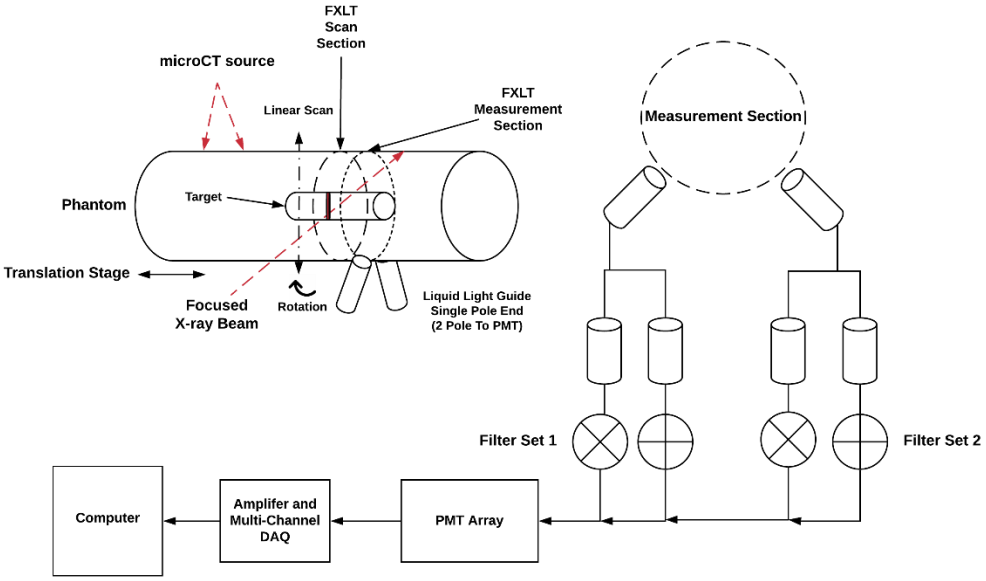

Figure 5.14. Proposed scanning scheme and acquisition for FXLT imaging system.

5.2.2. FXLT numerical simulations

To validate the feasibility of our designed FXLT imaging system, we have performed two sets of numerical simulations. For both simulation studies, we generated a cylindrical background phantom of 12 mm in diameter and 20 mm in height. The background phantom had an absorption coefficient (μ_a) of 0.0072 mm^{-1} and a reduced scattering coefficient ($\mu`_s$) of 0.72 mm^{-1} to mimic the optical properties of mice tissue. Inside the background phantom we placed six cylindrical targets of 1.0 mg/mL GOS:Eu^{3+} concentration as shown in Fig. 5.15. The 15 mm long targets each had diameters of 75 μm and were placed such that each target has an edge-to-edge distance of 75 μm. During the simulated scan, the emitted luminescent photons were collected by 4 detectors (fiber-PMT set-ups) that were positioned 2 mm below the scanned transverse section. We only performed scanning and reconstruction of a single transverse section of the phantom and targets which were discretized with a 2D grid having a pixel size of 10 μm^2.

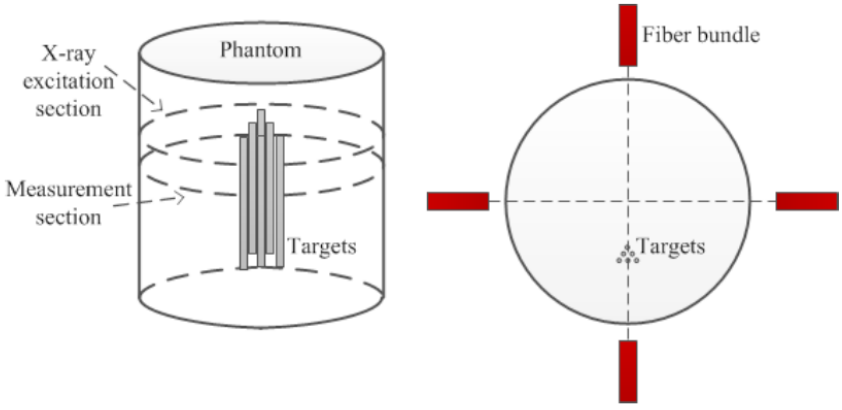

Figure 5.15. Phantom geometry and target positions for numerical simulations. Fiber bundles indicate the measurement locations.

In the first numerical simulation, we simulated the scanning scheme of the proposed FXLT imaging system and included the dual-cone geometry of the focused x-ray beam as well as x-ray attenuation and scattering (of 17.5 keV x-ray photons) in the forward model and reconstruction algorithm. For all simulation cases, we used a single dual-cone x-ray beam to scan the phantom at the depth of 5 mm from the phantom top surface and collected the emitted optical photons using 4 fiber-PMT set-ups surrounding the phantom 2 mm below the scanned section (each spaced 90° apart). In first numerical simulation, we incorporated as closely as we can, the actual dual-cone x-ray beam geometry provided by the manufacture (XOS, East Greenbush, NY) for our designed FXLT system as given below in Table 5.1. However, due to the constraints of our 2D grid, we round the focal spot to 50 μm in diameter and only incorporate the beam changes at ±2 mm (60 μm) as well as ±4 mm (70 μm). We placed the x-ray beam focal spot such that it would scan the center of our phantom during the FXLT scan. For this simulation study, we performed FXLT scans of different angular projections (3, 6, and 9) with angular step sizes of 60, 30, and 20

degrees respectively to determine the effect of different projection numbers on the spatial resolution. In addition, a second set of numerical simulations was performed to determine the effects of the x-ray beam size on the spatial resolution. In this case, we doubled the x-ray beam diameters used in the first simulation.

Table 5.1. Manufacturer provided table of the output x-ray beam size.

Distance from focus	At Focus (25 mm OFD)	±1 mm	±2 mm	±3 mm	±4 mm	±5 mm	±10 mm
Output beam size at 17.5 keV (μm, FWHM)	55	57	60	65	70	78	135

For the image reconstruction, the system matrix generated by the forward model was interpolated to the fine 2D grid. During reconstruction, the L^1 regularization method was applied in the MM reconstruction framework to reconstruct the images. Fig. 5.16 below shows the results of the numerical simulations of different angular projections of the proposed FXLT imaging system from which we can see the six targets have been successfully reconstructed and can be separated for all cases. The green circles in the figure represent the true target locations. We calculated the DICE similarity coefficients for each of the reconstructed cases and for each projection number of 3, 6, and 9 projections, the corresponding DICE was calculated using the full width ten percent maximum (FW10%M) to be 35.249, 46.097, and 49.333 % respectively. In addition, the size of each of the two targets in the middle row was also calculated using the FW10%M and the results shown in Table 5.2. It should be noted that with our numerical simulation setup, it is impossible to obtain a perfect target size (0.075 mm) since our grid is only 10 μm in size. Our results indicate that we can perform FXLT scans with as little as 3 angular projections and that we can improve the spatial resolution and imaging quality using more angular projections if required with the proposed imaging system.

The second set of numerical simulations performed was to investigate the effects of the x-ray beam size on the imaging quality and spatial resolution of the proposed FXLT imaging system. This simulation was set-up the same as the previous simulation, except that the x-ray beam diameter used was twice the size. In this set-up we used an x-ray focal diameter of 100 μm and set the x-ray beam diameter to be 120 μm at ±2 mm away from the focal spot and 140 μm at ±4 mm away from focal spot. For this simulation, we performed scans using both 6 and 9 angular projections using angular step sizes of 30 and 20 degrees respectively. The results of the numerical simulation are shown above in Fig. 5.17. Even at 9 angular projections, the targets cannot be resolved successfully. For the angular projections used (6 and 9), the corresponding DICE for the middle row targets were calculated to be 9.780 and 22.6138 % respectively. Compared to the earlier results in Figs. 5(b, c), the image quality is heavily degraded by using a larger x-ray beam and the targets cannot be resolved. These results are consistent with our previous findings in Section 2.1 where we found that the spatial resolution of XLCT is about double the size of the x-ray beam diameter used.

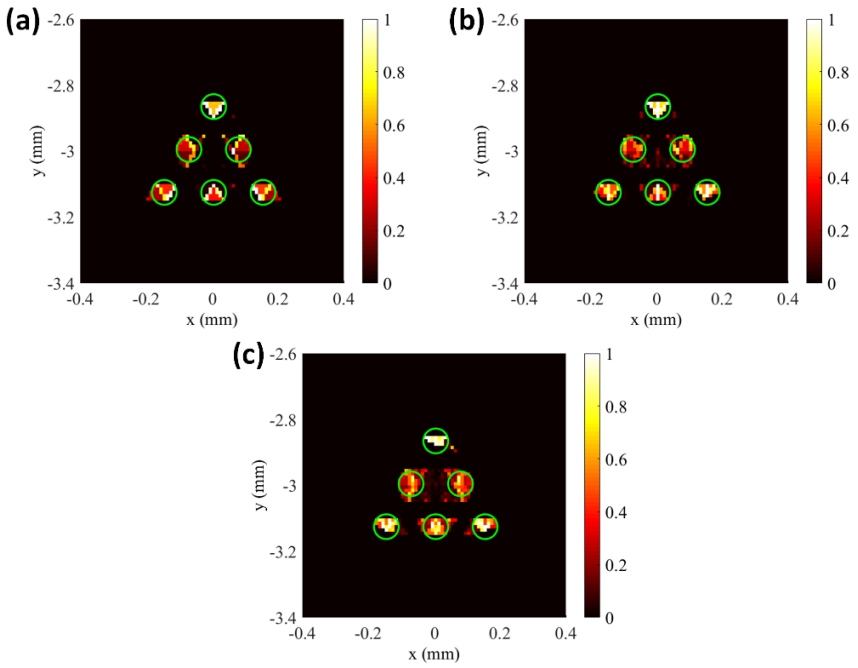

Figure 5.16. Results of numerical simulation determining the effects of projection number on spatial resolution. The green circle represents the true target regions. Reconstructed images at (a) 3 Projections, (b) 6 Projections, and (c) 9 Projections.

Table 5.2. Calculated target sizes for reconstruction with different angular projections.

Number of Angular Projections	Left Target Size (mm)	Right Target Size (mm)
3	0.060	0.060
6	0.060	0.070
9	0.080	0.080

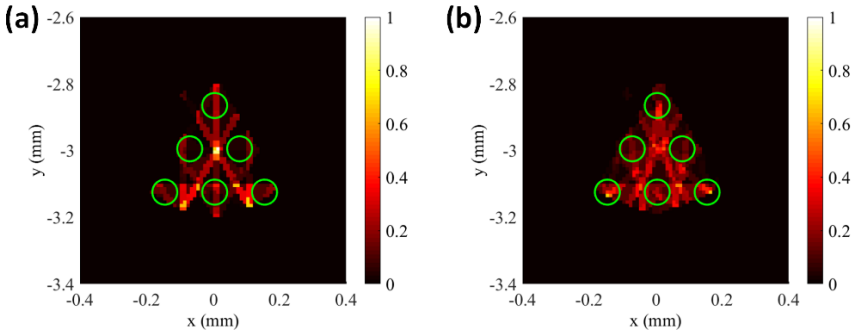

Figure 5.17. Results of numerical simulation of the effect of beam size. Reconstructed images using (a) 6 Projections and (b) 9 Projections. FXLT reconstruction failed when the beam size is large.

In Section 4.1, we demonstrated that the spatial resolution of XLCT imaging could be improved by reducing the scanning step size. We performed an additional set of numerical simulations to demonstrate this method applied to our FXLT imaging system. We performed numerical simulations using similar parameters as the previous numerical simulations but included two more scenarios. In addition, the 2D grid size was increased

from 10 μm^2 to 25 μm^2. The first scenario was XLCT scanning with a 50 μm straight pencil beam (no dual-cone geometry). We then performed a simulation, including the dual-cone geometry (as previous simulations), except that we reduced the scanning step size by two, to show the improvement in the reconstruction quality. The results of these simulations are shown in Fig. 5.18, where Fig. 5.18(a) shows the 50 μm straight pencil beam reconstruction with conventional scanning scheme, Fig. 5.18(b) shows the conventional scanning scheme with the dual-cone geometry, and finally Fig. 5.18(c) shows the results from reducing the scanning step size by two using the dual-cone geometry. We can see that by reducing the scanning step size, the image quality improves, and we obtain a better reconstruction than the other two cases. Based on our results from Section 4.1, if we use ¼ of the typical step size, we can achieve a 1.6 times improvement of the spatial resolution, thus we anticipate that the proposed FXLT imaging system can achieve a spatial resolution of about 94 μm.

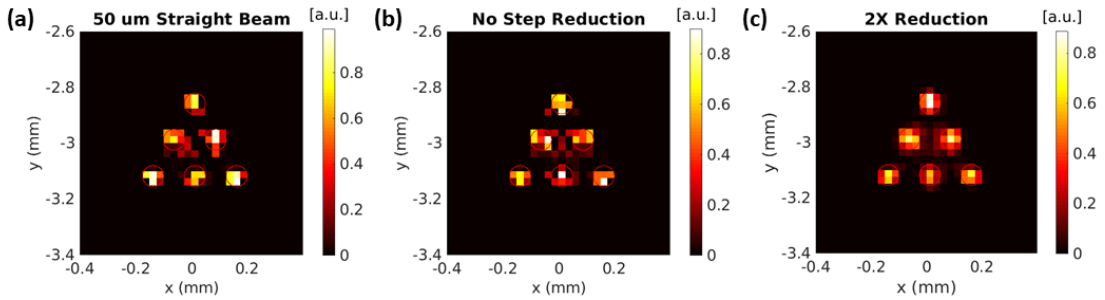

Figure 5.18. FXLT numerical simulation results using (a) 50 μm straight pencil beam, (b) conventional scanning scheme using dual-cone geometry, and (c) dual-cone geometry with a two times step size reduction.

5.2.3. Current status of the FXLT scanner build

In this section, we discuss the current state of the FXLT build in our laboratory showing some of the components we have already purchased and received and the current assembly progress of the imaging system.

The purchased HDRT is shown in Fig. 5.19. The stainless-steel ring track is shown in Fig. 5.19(a) to which we will mount a custom cut optics board to mount the primary components of the imaging system. The pinion in Fig. 5.19(b) accepts a 30 mm shaft that will be coupled to the servomotor to be purchased and drive (rotate) the ring track. This pinion uses a keyless locking bushing in order to secure firmly to the shaft. Between the optics board and ring track, the spacers (Fig. 5.19(c)) will be used to allow some clearance room between the track and mounted components. To support the ring track, we have 3 bearings (Fig. 5.19(d)) positioned 120 degrees apart in our system. Lastly, we have three lubricators (Fig. 5.19(e)) that use ISO 68 hydraulic oil to keep the ring track well lubricated during rotation. The bearings and lubricator attach directly onto the imaging system frame using custom aluminum blocks (example in Fig. 5.19(e) for the lubricator) with a T-nut set-up. The optics board to be mounted (MB30, Thorlabs) was cut using a high-pressure water cutting system to our specifications and is shown in Fig. 5.20.

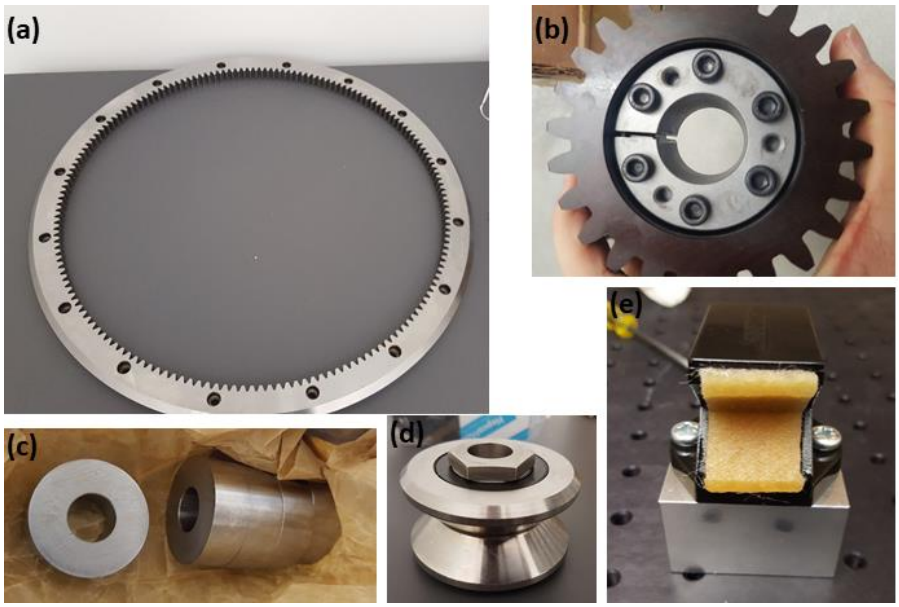

Figure 5.19. Heavy-duty ring track for FXLT imaging system. (a) Ring track; (b) Pinion; (c) spacers; (d) bearings; (e) lubricators.

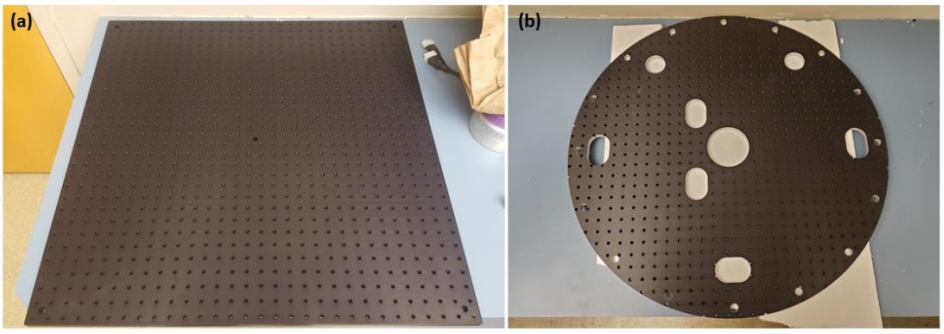

Figure 5.20. Optics board for FXLT imaging system components. (a) Pre-cut optics board; (b) Cut optics board.

The imaging system frame was designed with aluminum extrusions from 80/20 Inc. After designing the frame in CAD, the parts were ordered, and the frame built in our laboratory as shown in Fig. 5.21. We then mounted the HDRT as seen in Fig. 5.21(a) and then the optics board (Fig. 5.21(b)). For radiation and light shielding, the custom designed lead-lined stainless-steel panels (1mm lead; 10 mm total thickness) were fabricated (BFK Innovation Inc.) to our specifications. The panels secure to the aluminum frame using T-nuts and bolts. A single side-panel and the imaging system door is shown in Fig. 5.22 (a) and (b), respectively. The mounted panels and door are shown in Fig. 5.22(c). Additional aluminum blocks are added beneath each of the panels and door to provide additional support.

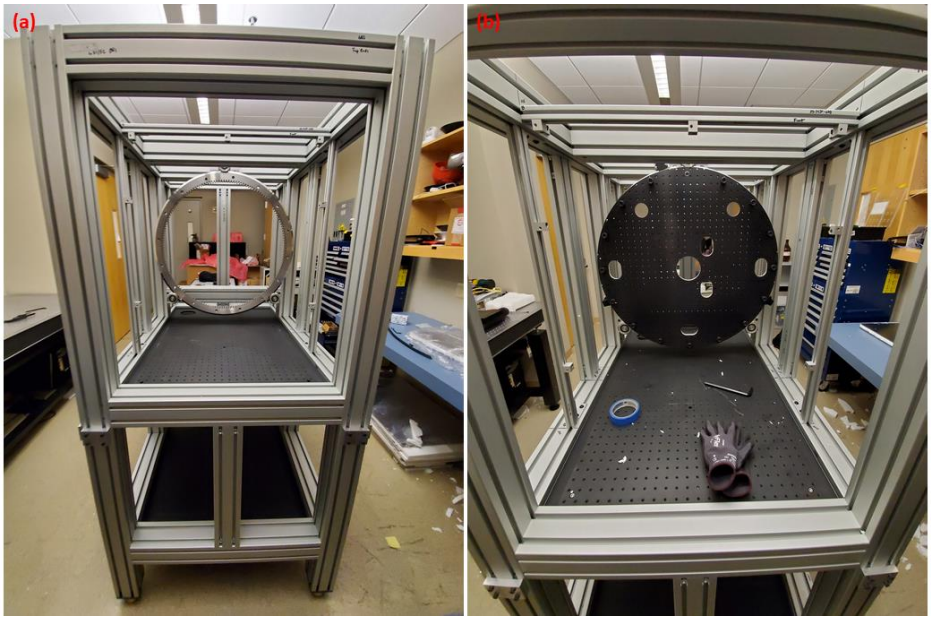

Figure 5.21. (a) Imaging system frame with ring track installed; (b) The optics board mounted to the ring track.

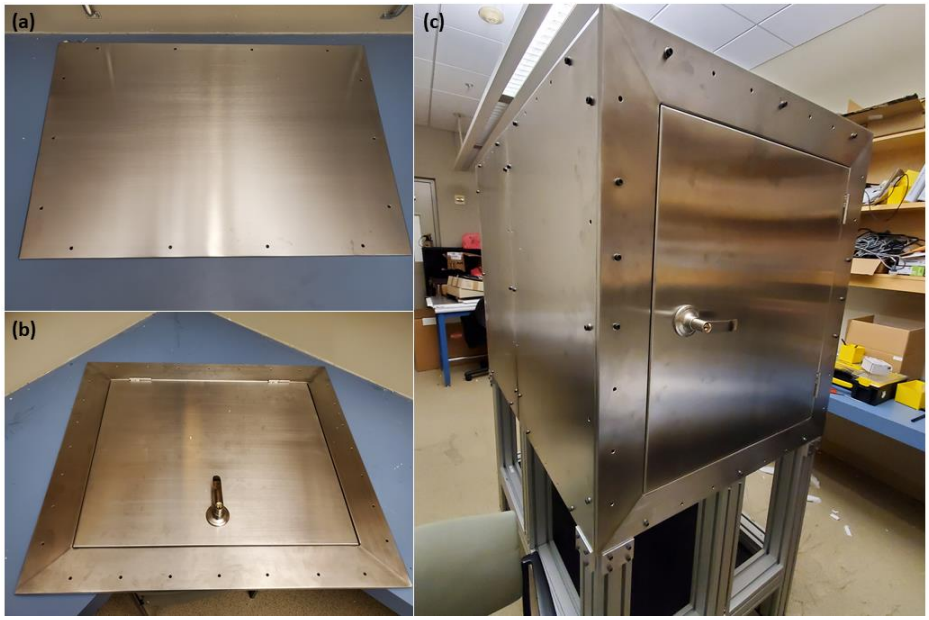

Figure 5.22. (a) Lead-lined stainless-steel side-panel; (b) Imaging system door (also lead lined); (c) Panels and door mounted on the FXLT imaging system frame.

Some additional components are shown below. The x-ray tube for microCT imaging is shown in Fig. 5.23(a) along with its power supply (Fig. 5.23(c)) along with their mounting set-ups in Fig. 5.23(c) and (d), respectively. The x-ray tube for the FXLT imaging is shown in Fig. 5.24 and its mounting bracket is shown in Fig. 5.24(b) that will be mounted to a linear stage (NLS-8). We designed a mountable aluminum box for the power supply as well, but it is currently not completed at this time. We mounted the

microCT set-up and the FXLT linear stage temporarily for demonstration purposes seen in Fig. 5.25. The optical detection system for the FXLT system comprises of an array of four PMTs which have their signal delivered by used of two bifurcated liquid light guides, which have been shown to be more sensitive and efficient at delivering light than the traditional silica core fiber bundles, which we have used previously. The signal, after being delivered to the PMTs is amplified by use of broadband preamplifiers which finally deliver the signal to a high-speed digitizer. The components of the FXLT optical detection set-up is pictured in Fig. 5.26, except for the digitizer.

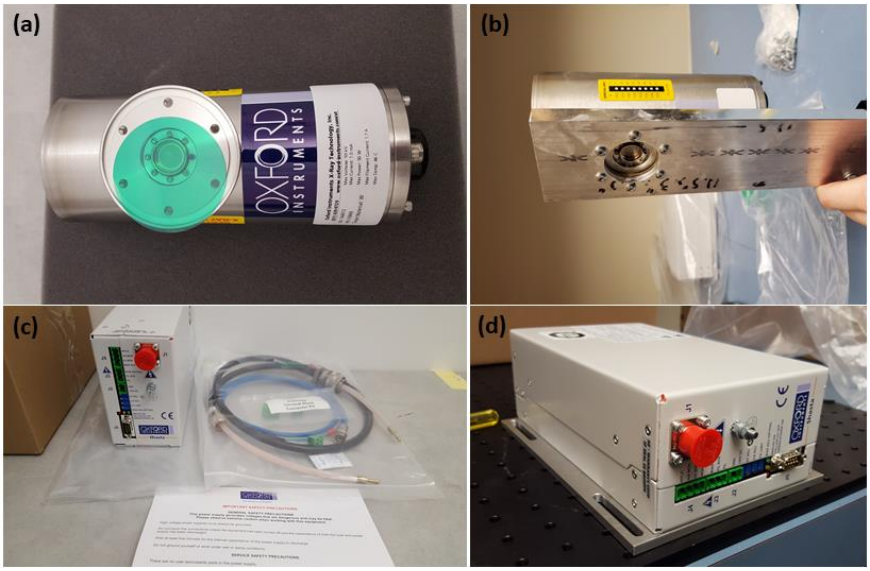

Figure 5.23. (a) microCT x-ray tube; (b) Mounting bracket with the x-ray tube; (c) microCT power supply; (d) Mounting for power supply.

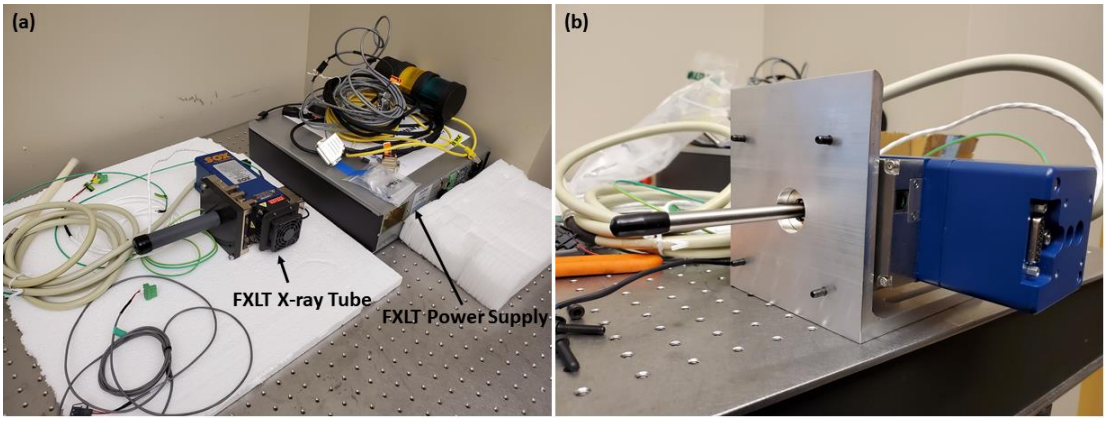

Figure 5.24. (a) FXLT x-ray tube, power supply, and cables; (b) 90-degree bracket for mounting x-ray tube to a linear stage.

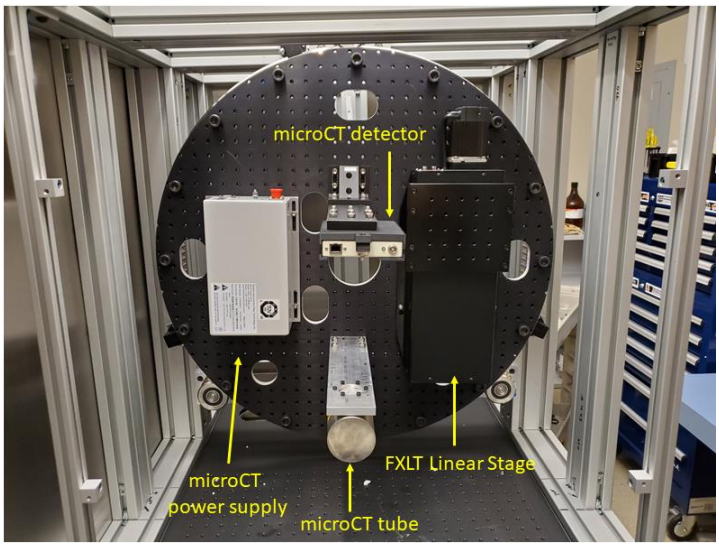

Figure 5.25. microCT components and FXLT linear stage mounted to the gantry set-up. Note: The positions of the components are not the same as the designed position, but only temporarily placed for demonstration purposes. The placement will be the same as the designed CAD model.

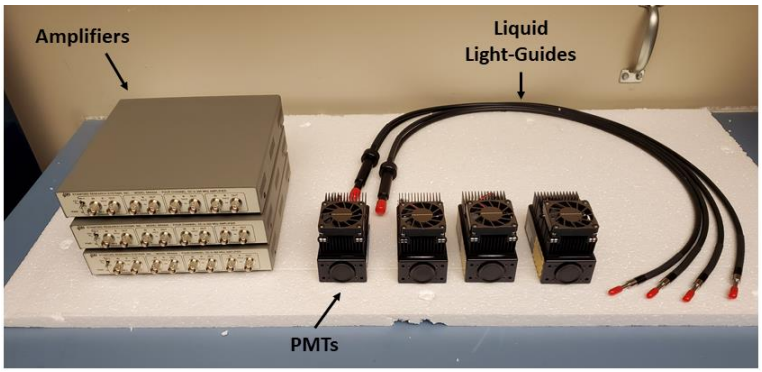

Figure 5.26. FXLT optical detection components.

Overall, the build of the FXLT imaging system is still a work in progress and there is still significant work to be done to make the FXLT imaging system viable and working. After the assembly of the imaging system is completed, we must also develop the control and image acquisition software to perform and automate both the microCT imaging and the FXLT imaging. We must also carefully calibrate the imaging system, for example the rotational resolution of the gantry, after installation of the motor-pinion set-up which is still currently being completed.

In summary, here we proposed and started the build of a small animal dedicated FXLT scanner that can perform both microCT and 3D high-resolution FXLT imaging in a single imaging system. Having the ability to perform both the microCT and FXLT imaging inside of the single scanner is highly beneficial, as it allows for easy co-registration of the anatomical and optical imaging, since the orientation of the imaged object is guaranteed to be the same, unlike our previous generation XLCT scanners which required carefully

calibration to register the two imaging modalities, since the object must be transferred from one set-up to the other. Other additions to the FXLT scanner will also allow for improved imaging compared to previous XLCT imaging systems. First, the x-ray beam size is much smaller (50 μm vs 100 μm in our system described in Section 2.3) which will allow for much higher spatial resolution capabilities. Here, we estimated the FXLT scanner's achievable spatial resolution to be about 94 μm. Next, the use of four highly sensitive PMTs (H7422-50) to detect the optical signals will allow for much higher measurement sensitivity than our previous set-up where only a single PMT was used. In addition, we have opted to switch from silica-core fiber bundles to liquid light-guides which will allow for much higher optical transmission efficiency, especially in the NIR range, which means we can expect much more signal to be delivered to each PMT than previously. From previous studies using GOS:Eu^{3+}, we estimated that the limits of detection (LOD) was approximately 2 μg/mL. With this new set-up, we expect to achieve an even lower LOD, which will be verified in future studies. With additional PMTs, we are now also capable of performing imaging of different nanoparticles with different emission wavelengths as well, which is useful for multiplexed imaging of different targets. We are currently collaborating with other researchers in order to synthesize bright nanophosphors with distinct luminescence spectra which will be a future study with this imaging system.

CHAPTER 6

CONCLUDING REMARKS AND FUTURE DIRECTIONS FOR XLCT IMAGING

Within the last decade, the concept of x-ray induced luminescence imaging has emerged and demonstrated a wide array of potential applications, for example the molecular imaging of small animals, by combining the high spatial resolution of conventional x-ray imaging and the superb measurement sensitivity of optical imaging. Specifically, x-ray luminescence computed tomography (XLCT) imaging emerged as a powerful imaging modality capable of the high-resolution imaging of deeply embedded x-ray excitable contrast agents in three-dimensions. As an optical imaging modality, XLCT can mitigate the *ill-posedness* of deep tissue optical imaging by incorporating a selective-excitation scanning scheme which aids in the image reconstruction. Since the inception of XLCT in 2010, there has been numerous studies exploring the optimization and applications of this technique as discussed in Section 1.3.2. Many groups have proposed XLCT imaging with different x-ray beam geometries, each with their own strengths as well as drawbacks. In particular, the work presented in this dissertation has further demonstrated the strengths of the narrow x-ray beam based XLCT imaging (NB-XLCT) with a selective-excitation scanning scheme and we have also addressed many of the shortcomings of this approach, particularly the long imaging time to make the technique a feasible tool for the molecular imaging community.

In this dissertation, we have developed and built several prototype XLCT imaging systems and demonstrated the advantages of each generation of XLCT scanners. We first built a simple collimated x-ray beam based XLCT imaging system and shown by using a collimator with a small aperture size, we could generate a superfine x-ray beam and achieve high-spatial resolution for XLCT imaging. We have also found that for the NB-XLCT imaging, the spatial resolution has a high dependency on the x-ray beam size as well as the number of measurements used (number of angular projections). We then addressed the long scan time of this approach by proposing the use of multiple narrow x-ray beams to scan our object and were able to reduce the scan time by a factor equal to the number of scanning x-ray beams. We have also shown that the acquired radiation dose was within the range of a typical CT scan.

To further improve upon the spatial resolution and the sensitivity of XLCT imaging, we next proposed and built a focused x-ray beam based XLCT imaging system. With this system, we achieved an improved x-ray photon flux by use of polycapillary optics in order to generate a small x-ray beam instead of a collimator, which was demonstrated to have a low x-ray photon utilization efficiency. In addition, we also shown that using optical fibers

coupled to a PMT could allow much higher optical measurement sensitivity compared with the conventional EMCCD camera-based detection method. With this improved detection efficiency, we could acquire our measurements in a much shorter time than before. The radiation dose for this system was shown to be much higher than the collimated based system, primarily due to the increased x-ray photon flux, but was still not enough to cause significant radiation damage for mice imaging.

We also have shown that the spatial resolution of XLCT imaging could also be improved by use of a reduced scanning step size, although at the cost of a longer measurement time. With the reduced scanning method, we found that we could improve the spatial resolution about 1.6 times. Then, we demonstrated the high-resolution XLCT imaging capabilities with our focused x-ray beam based XLCT imaging system by scanning a cylindrical phantom embedded with multiple targets and shown that we could separate targets with edge-to-edge distances as small as 150 μm with our set-up. With a smaller x-ray beam size, such as in our latest proposed generation of XLCT imaging system (Section 5.2), we are able to achieve much higher spatial resolution, though the fabrication of smaller targets will be challenging.

For our latest generation of XLCT imaging systems, we proposed and are currently building a small animal dedicated focused x-ray luminescence tomography (FXLT) imaging system. We, along with the works of some other research groups [21, 24, 26], have demonstrated the feasibility of XLCT for small-animal imaging. In our study, we used a euthanized mouse embedded with a single capillary tube target and demonstrated that the location of the embedded phosphor particles could be recovered with high precision and accuracy (Section 5.1). With our new FXLT imaging system described in Section 5.2, we design a multimodality scanner (microCT and FXLT), that we hope will become a powerful tool for future applications in molecular imaging once it is completed. One such application would be for measurements of the lifetime measurements of embedded nanophosphors, a similar technique to fluorescence lifetime imaging (FLIM). The light generation of the nanophosphors is considered as a form of phosphorescence, which has longer lifetimes than fluorescence. We previously demonstrated the potentials of XLCT for lifetime imaging in a method called time-domain XLCT imaging [94], which we hope to extract biological microenvironmental information such as tumor oxygenation levels. We can also take advantage of the multiple wavelength emission of nanophosphors and the two-wavelength capacity of our proposed FXLT imaging system to sense physiological parameters inside of a deep tumor, for example the EGFR receptor density in breast cancer using two nanophosphors (with and without EGFR antibodies) with distinct emission wavelengths.

In the XLCT imaging studies demonstrated in this dissertation, we have only reconstructed 2D transverse sections. Although XLCT is capable of 3D imaging by continuously scanning at different imaging depths, we were not able to demonstrate 3D imaging with our current set-ups. Though the proposed FXLT scanner can easily perform 3D imaging by moving the imaging stage with a motorized linear stage, the set-up is different than our previously built systems. We are currently working to upgrade the imaging system described in Section 2.3 in order to perform 3D XLCT imaging and will

demonstrate high-resolution 3D XLCT imaging in future studies. In the upgraded system, we have replaced the manual lab jack with a motorized vertical lift which will make the 3D possible in a feasible imaging time. We show the 3D design and the current experimental setup of the upgraded system in Fig. 6.1 and 6.2, respectively. Note that in actual build (Fig. 6.2) we have opted to use a similar scintillator/fiber set-up as in the FXLT imaging system to detect the focused x-ray beam intensity to determine the object boundary instead of the x-ray detector. We are working to develop the macro code to automate the 3D imaging, which will be demonstrated in a future study.

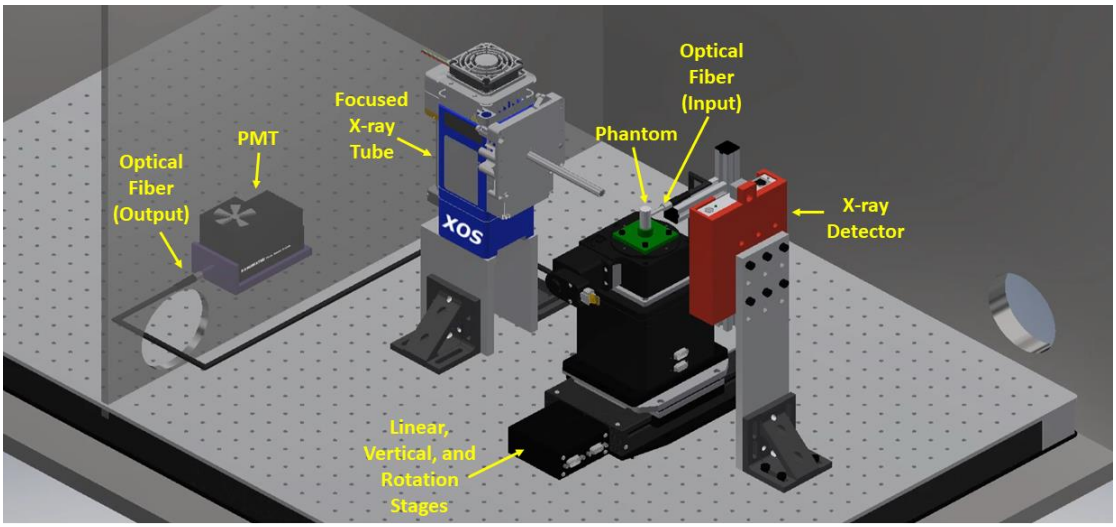

Figure 6.1. CAD model of the upgraded 3D focused x-ray beam based XLCT imaging system.

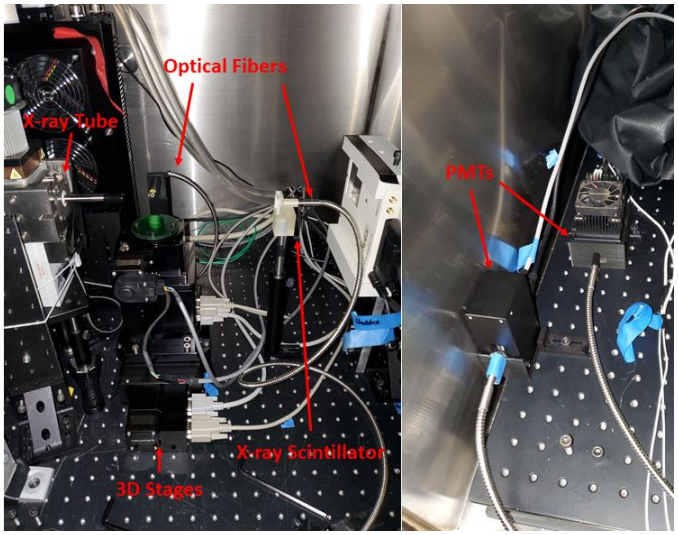

Figure 6.2. Photograph of the upgraded 3D focused x-ray beam based XLCT imaging system.

In addition, we are also currently working with collaborators from Dr. Jeffrey Anker's group at Clemson University to develop and synthesize optically distinct and biocompatible rare-earth elemental nanophosphors to perform multiplexed XLCT imaging with our FXLT scanner. An example of biocompatible nanophosphors that have been

developed by our collaborators are $NaGdF_4$:Eu and $NaGdF_4$:Tb which are enclosed in a silica shell and functionalized with biotin as shown in Fig. 6.3. We can see that the synthesized nanophosphors have unique and distinct luminescence emission which can allow for multiplexed XLCT imaging, which will be demonstrated in future studies with the FXLT imaging system. Details of the nanophosphor synthesis can be found in [62].

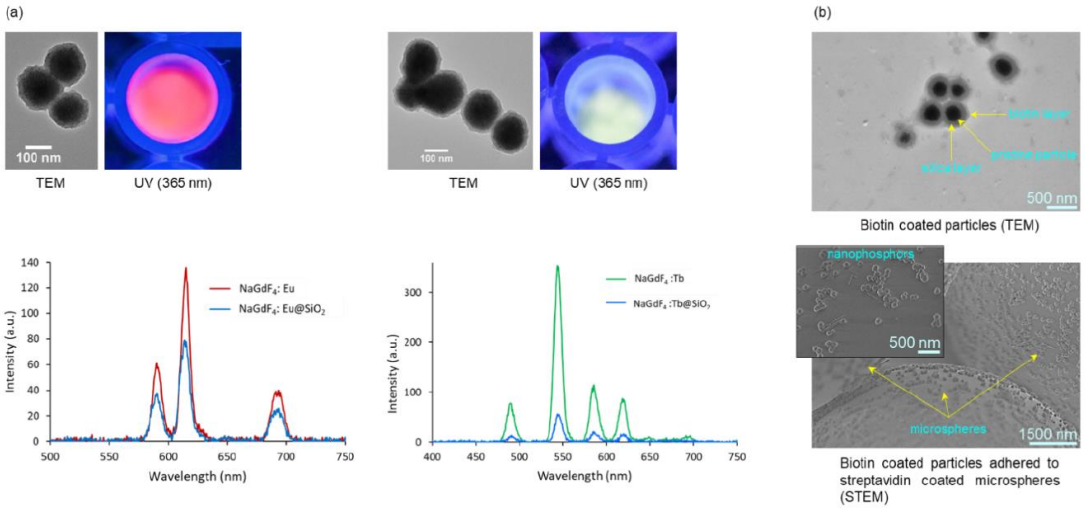

Figure 6.3. $NaGdF_4$ nanophosphors developed by collaborators at Clemson University. (a) Luminescence spectra of $NaGdF_4$:Eu (red) and $NaGdF_4$:Tb (green) nanophosphors , TEM images above the spectra show silica coated particles. (b) TEM image of biotin coated nanophosphors (top), and STEM image of biotin coated nanophosphors adhered to streptavidin coated microspheres (bottom), inset image is a closer view.

Another future work is the application of deep-learning to XLCT imaging. With help from Dr. Ge Wang's group at Rensselear Polytechnic Institute (RPI), we are developing a new XLCT reconstruction algorithm which incorporates deep-learning techniques to aid in the image reconstruction to enhance the scanning efficiency by reducing the number of projection views and translation steps. Deep learning is an efficient method of functional approximation based on a training dataset to construct a nonlinear mapping from low quality images (reconstructed nanophosphors concentration images) to corresponding high quality images. Preliminary work with the development and numerical simulation studies with the proposed deep-learning based XLCT reconstruction algorithm are described in [62]. We are currently working on validating the method with experimental phantom studies which will be discussed in future studies.

REFERENCES

[1] R.F. Mould, *"The early history of x-ray diagnosis with emphasis on the contributions of physics in 1895-1915",* Phys. Med. Biol. **40** (1995) 1741-1787.

[2] W.G. Bradley, *"History of Medical Imaging",* Proc. of the Amer. Philo. Soc., Vol. 152, No. 3 (Sep. 2008) 349-361.

[3] W.A. Kalender, *"X-ray computed tomography,"* Phys. Med. Biol. **51** (2006) R29-R43.

[4] D.T. Ginat and R. Gupta, *"Advances in Computed Tomography Imaging Technology",* Annu. Rev. Biomed. Eng. 2014. 16:431-53.

[5] U. Speck, *"Contrast agents: x-ray contrast agents and molecular imaging – a contradiction?",* Handb. Exp. Pharmacol. **185**, 167-175 (2008).

[6] R.R. Edelman, *"The history of MR Imaging as seen through the pages of radiology",* Radiol., Vol. 273, No. 2 (2014).

[7] F.A. Jaffer and R. Weissleder, *"Molecular imaging in the clinical arena",* J. Amer. Med. Assoc. **293**, 855-862 (2005).

[8] P. Caravan, *"Strategies for increasing the sensitivity of gadolinium based MRI contrast agents",* Chem. Soc. Rev. **35**(6), 512-523 (2006).

[9] G. Pratx, *"A tale of two photons: radioluminescence and its application in molecular imaging",* Proc. of SPIE, Vol. 10049, 1004916 (2017).

[10] Y. Yang, Y. Wu, J. Qi, S. St James, H. Du, P.A. Dokhale K.S. Shah, R. Farell, and S.R. Cherry, *"A prototype PET scanner with DOI-encoding detectors",* J. of Nucl. Med. **49** (7), 1132-1140 (2008).

[11] J. Peremans, B. Cornelissen, B. Van den Bossche, K. Audenaert, and C. Van de Wiele, *"A review of small animal imaging planar and pinhole spect Gamma camera imaging",* Vet. Radiol. Ultrasound **46** (2), 162-170 (2005).

[12] V. Ntziachristos, J. Ripoll, and R. Weissleder, *"Would infrared fluorescence signals propagate through large human organs for clinical studies?",* Opt. Lett. **27**, 333-335 (2002).

[13] X.D. Wang, Y.J. Pang, G. Ku, X.Y. Xie, G. Stoica, and L.H.V. Wang, *"Noninvasive laser induced photoacoustic tomography for structural and functional in vivo imaging of the brain",* Nat. Biotech. **21**(7), 803-806 (2003).

[14] M. Ahmad, G. Pratx, M. Bazalova, and L. Xing, *"X-ray luminescence and x-ray fluorescence computed tomography",* IEEE Access **2**, 1051-1061 (2014).

[15] M. Gambaccini, A. Taibi, A. DelGuerra, M. Marziani, A. Tuffanelli, *"MTF evaluation of a phosphor-coated CCD for x ray imaging",* Phys. in Med. & Bio. **41** (12), 2799-2806 (1996).

[16] H. Chen, D.E. Longfield, V.S. Varahagiri, K.T. Nguyen, A.L. Patrick, H. Qian, D.G. VanDerveer, and J.N. Anker, *"Optical imaging in tissue using X-ray excited luminescenct sensors",* Roy. Chem. Soc. Analyst, **136**, 3438-45 (2011).

[17] H. Chen, A.L. Patrick, Z. Yang, D.G. Vanderveer, and J.N. Anker, *"High-resolution Chemical Imaging Through Tissue with an X-ray Scintillator Sensor",* ACS Analy. Chem. **83**, 5045-49 (2011).

[18] G. Pratx, C.M. Carpenter, C. Sun, R. Rao, and L. Xing, *"Tomographic molecular imaging of x-ray excitable nanoparticles",* Opt. Lett. 35, 3345-3347 (2010).

[19] G. Pratx, C.M. Carpenter, C. Sun, and L. Xing, *"X-ray luminescence computed tomography via selective excitation: a feasibility study",* IEEE Trans. Med. Imag 29, 1992-99 (2010).

[20] C. Li, K. Di, J. Bec, and S.R. Cherry, *"X-ray luminescence optical tomography imaging: experimental studies",* Opt. Lett. **38** (13) (2013).

[21] C.M. Carpenter, C. Sun, G. Pratx, H. Liu, Z. Cheng, and L. Xing, *"Radioluminscent nanophosphors enable multiplexed small-animal imaging",* Opt. Expr. **20** (11) (2012).

[22] Do. Chen, S. Zhu, H. Yi, X. Zhang, Du. Chen, and J. Liang, *"Cone beam x-ray luminescence computed tomography: a feasibility study",* Med. Phys. **40** (3) (2013).

[23] G. Zhang, F. Liu, J. Liu, J. Luo, Y. Xie, J. Bai, and L. Xing, *"Cone beam x-ray luminescence computed tomography based on Bayesian method",* IEEE Trans. on Med. Imag. **36** (1) 225-235 (2017).

[24] X. Liu, Q. Liao, and H. Wang, *"In vivo x-ray luminescence tomographic imaging with single-view data",* Opt. Lett. **38** (22) (2013).

[25] S. Tzoumas, D. Vernekohl, and L. Xing, *"Coded-aperture compressed sensing x-ray luminescence tomography",* IEEE Trans. on Biomed. Eng. **65** (8) (2017).

[26] X. Liu, H. Wang, M. Xu, S. Nie, and H. Lu, *"A wavelet-based single view reconstruction approach for cone beam x-ray luminescence tomography imaging",* Biomed. Opt. Expr. **5** (11) (2014).

[27] W. Cong and G. Wang, *"X-ray fan-beam luminescence tomography",* Austin J. of Biomed. Eng. **1** (5) (2014).

[28] D. Chen, S. Zhu, X. Cao, F. Zhao, and J. Liang, *"X-ray luminescence computed tomography imaging based on X-ray distribution model and adaptively split Bregman method",* Biomed. Opt. Expr. **6** (7) (2015).

[29] B. Quigley, C.D. Smith, S. Cheng, J.S. Souris, C.A. Pelizarri, C. Chen, L. Lo, C.S. Reft, R.D. Wiersma, and P.J. La Riviere, *"Sensitivity evaluation and selective plane imaging geometry for x-ray induced luminescence imaging",* Med. Phys. **44** (10) 5367-5377 (2017).

[30] M.M. Xing, W.H. Cao, T. Pang, X.Q. Ling, N. Chen, *"Preparation and characterization of monodisperse spherical particles of x-ray nano-phosphors based on Gd_2O_2S:Tb",* Chin. Sci. Bull. 54(17), 2982-6 (2009).

[31] J. Thirumalai, R. Chandramohan, S. Valanarasu, T.A. Vijayan, R.M. Somasundaram, T. Mahalingam, S.R. Srikumar, *"Shape-selective synthesis and opto-electronic properties of Eu^{3+}-doped gadolinium oxysulfide nanostructures"*, J. of Mat. Sci. **44** (14), 3889-99 (2009).

[32] Y. Tian, W.H. Cao, X.X. Luo, Y. Fu, *"Preparation and luminescence property of Gd_2O_2S:Tb X-ray nano-phosphors using the complex precipitation method",* J. of Allo. and Compo. 433(1-2), 313-317 (2007).

[33] H.Y. Wang, R.J. Wang, X.M. Sun, R.X. Yan, Y.D. Li, *"Synthesis of red-luminescent Eu^{3+}-doped lanthanide compounds hollow spheres",* Mat. Res. Bull. 40(6), 911-9 (2005).CX

[34] A.M. Pires, M.R. Davalos, E.B. Stucchi, *"Eu^{3+} as a spectroscopic probe in phosphors based on spherical fine particle gadolinium compounds"*, Int. J. Inorg. Mater. 3(7), 785-90 (2001).

[35] C. Sun, G. Pratx, C.M. Carpenter, H. Liu, Z. Cheng, S.S. Gambhir, and L. Xing, *"Synthesis and radioluminescence of PEGylated Eu^{3+}-doped nanophosphors as bioimaging probes",* Adv. Mater. **23** (24) (2011).

[36] H. Chen, F. Wang, T.L. Moore, B. Qi, D. Sulejmanovic, S. Hwu, O.T. Mefford, F. Alexis, and J.N. Anker, *"Bright x-ray and up-conversion nanophosphors annealed using encapsulated sintering agents for bioimaging applications",* J. Mater. Chem. B **5**, 5412 (2017).

[37] L. Sudheendra, G.K. Das, C. Li, D. Stark, S.R. Cherry, and I.M. Kennedy, *"$NaGdF_4$:Eu^{3+} Nanoparticles for Enhanced X-ray Excited Optical Imaging",* Chem. of Mater. 26(5), 1881-8 (2014).

[38] B. Lutz, C. Dentinger, L. Sun, L. Nguyen, J.W. Zhang, A.J. Chmura, A. Allen, S. Chan, B. Knudsen, *"Raman nanoparticle probes for antibody-based protein detection in tissues"*, J. Histochem. Cytochem. **56** (4), 371-379 (2008).

[39] W. Zhang, Y. Shen, M. Liu, P. Gao, H. Pu, L. Fan, R. Jiang, Z. Liu, F. Shi, and H. Lu, *"Sub-10nm water dispersable β-$NaGdF_4$:X% Eu^{3+} nanoparticles with enhanced biocompatibility for in vivo x-ray luminescence computed tomography",* ACS Appl. Mater. Interfaces **9**, 39985-39993 (2017).

[40] T. Guo, Y. Lin, W. Zhang, J. Hong, R. Lin, X. Wu, J. Li, C. Lu, and H. Yang, *"High-efficiency x-ray luminescence in Eu^{3+}-activated tungstate nanoprobes for optical imaging through energy transfer sensitization",* Nanoscale **10**, 1607 (2018).

[41] M. Lun, W. Chen, G. Schatte, W. Wang, A.G. Joly, Y. Huang, R. Sammynaiken, and M. Hossu, *"A new Cu-cysteamine complex: structure and optical properties",* J. Mater. Chem. C **2**, 4239 (2014)

[42] M. Lun, X. Zou, and W. Chen, *"A new x-ray activated nanoparticle photosensitizer for cancer treatment",* J. of Biomed. Nanotech. **10**, 1501-8 (2014).

[43] X. Dai, K. Cheng, W.Zhao, and L. Xing, *"X-ray-induced shortwave infrared luminescence computed tomography",* Opt. Lett. **44** (19), 4769-4772 (2019).

[44] Y. Osakada, G. Pratx, C. Sun, M. Sakamoto, M. Ahmad, O. Volotskova, Q. Ong, T. Teranishi, Y. Harada, L. Xing, and B. Cui, *"Hard x-ray-induced optical luminescence via biomolecule-directed metal clusters",* Chem. Commun. **50**, 3549 (2014).

[45] S.G. Ryan, M.N. Butler, S.S. Adeyemi, T. Kalber, P.S. Patrick, M.Z. Thin, I.F. Harrison, D.J. Stuckey, M. Pule, and M.F. Lythgoe, *"Imaging of x-ray excited*

emissions from quantum dots and biological tissue in whole mouse," Sci. Rep. **9**, 19223 (2019).

[46] C. Li, A. Martinez-Davalos, and S.R. Cherry, *"Numerical simulation of x-ray luminescence optical tomography for small-animal imaging",* J. of Biomed. Opt. **19** (4) (2014).

[47] D. Zhu, Y. Zhao, R. Baikejiang, Z. Yuan, and C. Li, *"Comparison of regularization methods in fluorescence molecular tomography",* Photonics **1**, 96-109 (2014).

[48] D. Zhu and C. Li, *"Nonconvex regularizations in fluorescence molecular tomography for sparsity enhancement",* Phys. Med. Biol. **59**, 2901-2912 (2014).

[49] D. Zhu and C. Li, *"Nonuniform update for sparse target recovery in fluorescence molecular tomography accelerated by ordered subsets",* Biomed. Opt. Expr. **5**, 4249-4259 (2016).

[50] W. Zhang, D. Zhu, M. Lun, and C. Li, *"Collimated superfine x-ray beam based x-ray luminescence computed tomography",* J. of X-ray Sci. and Tech. **25** (6), 945-957 (2017). "The final publication is available at IOS Press through http://dx.doi.org/ 10.3233/XST-17265."

[51] W. Zhang, D. Zhu, M. Lun, and C. Li, *"Multiple pinhole collimator based x-ray luminescence computed tomography",* Biomed. Opt. Expr. **7** (7), 2506-2523 (2016).

[52] W. Zhang, M. Lun, and C. Li, *"Fiber based fast sparse sampling x-ray luminescence computed tomography",* Proc. of SPIE 10057, Multimodal Biomedical Imaging XI (2017).

[53] W. Zhang, M.C. Lun, A.A. Nguyen, C. Li, *"A focused x-ray beam based x-ray luminescence computed tomography",* J. of Biomed. Opt. **22** (11) 116004 (2018).

[54] M.C. Lun, W. Zhang, and C. Li, *"X-ray luminescence computed tomography: a sensitivity study",* Proc. of SPIE 10137, Medical Imaging 2017: Biomedical Applications in Molecular, Structural, and Functional Imaging (2017).

[55] M.C. Lun, W. Zhang, and C. Li, *"Sensitivity study of x-ray luminescence computed tomography",* Appl. Opt. **56** (11), 3010-3019 (2017).

[56] M. C. Lun and C. Li, *"X-ray luminescence imaging of air, water, and tissue phantoms",* Proc. of SPIE 10487, Multimodal Biomedical Imaging XIII (2018).

[57] M.C. Lun and C. Li, *"Background luminescence in x-ray luminescence computed tomography",* Appl. Opt. **58** (4), 1084-1092 (2019).

[58] Y. Zhang, M.C. Lun, C. Li, and Z. Zhou, *"Method for improving the spatial resolution of narrow x-ray beam-based x-ray luminescence computed tomography",* J. of Biomed. Opt. **24** (8), 086002 (2019).

[59] M.C. Lun and C. Li, *"High-resolution focused x-ray luminescence computed tomography",* Proc. of SPIE 11317, Medical Imaging 2020: Biomedical Applications in Molecular, Structural, and Functional Imaging; 11317D (2020).

[60] M.C. Lun, W. Zhang, and C. Li, *"Focused x-ray luminescence computed tomography: experimental studies",* Proc. of SPIE 10487, Multimodal Biomedical Imaging XIII; 108710G-1 (2018)

[61] M.C. Lun and C. Li, *"Focused x-ray luminescence computed tomography",* Proc. of SPIE 11113, Developments in X-ray Technology XII (2019).

[62] M.C. Lun, W. Cong, M. Arifuzzaman, M. Ranasinghe, S. Bhattacharya, J. Anker, G. Wang, and C. Li, *"X-ray luminescence imaging for small-animals",* Proc. of SPIE 11224, Optics and Ionizing Radiation; 112240F (2020).

[63] L.P. Colleti and G.J. Havrilla, *"Specimen preparation limitations in trace element analysis quantification using micro-x-ray fluorescence",* JCPDS-International Centre for Diffraction Data 2000, Advances in x-ray analysis **42**, 64-73 (2000).

[64] *"Standardized methods for measuring diagnostic x-ray exposures",* AAPM Diagnostic X-ray Imaging Committee Task Group #8, Report No. 31 (1991).

[65] M. Dehlinger, C. Fauquet, S. Lavandier, O. Aumporn, F. Jandard, V. Arkadiev, A. Bjeoumikhov, and D. Tonneau, *"Spatial resolution of confocal XRF technique using capillary optics",* Nano. Res. Lett. **8**, Article number: 271 (2013).

[66] W. Cong, Z. Pan, R. Filkins, A. Srivastava, N. Ishaque, P. Stefanov, and G. Wang, *"X-ray micromodulated luminescence tomography in dual-cone geometry",* J. of Biomed. Opt. **19** (7), 076002 (2014).

[67] N. Miyahara, T. Kokubo, Y. Hara, A. Yamada, T. Koike, and Y. Arai, *"Evaluation of x-ray doses and their corresponding biological effects on experimental animals in cone-beam micro-CT scans (R-mCT2)",* Radiol. Phys. Technol. **9**, 60-68 (2015).

[68] T.L. Phillips and G. Ross, *"Time-dose relationships in the mouse esophagus"*, Radiol. **113**, 435-440 (1974).

[69] C.M. Carpenter, C. Sun, and G. Pratx, *"Hybrid x-ray/optical luminescence imaging: characterization of experimental conditions",* Med. Phys. **37**, 4011-4018 (2010).

[70] M. J. Paulus, S. S. Gleason, S. J. Kennel, P. R. Hunsicker, and D. K. Johnson, *"High Resolution X-ray Computed Tomography: An Emerging Tool for Cancer Research",* Nat. Review, Neoplasia, Vol. **2**, Nos. 1-2, pp 62-70, Jan-Apr 2000.

[71] S. J. Schambach, S. Bag, L. Schilling, C. Groden, and M. A. Brockmann, *"Application of micro-CT in small animal imaging"*, El Sevier, Methods **50** (2010).

[72] K. Yang, A. L.C. Kwan, D. F. Miller, and J.M. Boone, *"A geometric calibration method for cone beam CT systems",* Med. Phys. **6** (33), 1695-1706 (2006).

[73] C. Li, G. S. Mitchell, J. Dutta, S. Ahn, R. M. Leahy, and S. R. Cherry, *"A three-dimensional multispectral fluorescence optical tomography imaging system for small animals based on a conical mirror design",* Opt. Expr. **17** (9), 7571-7585 (2009).

[74] S. Yamamoto, T. Toshito, S. Okumura, and M. Komori, *"Luminescence Imaging of water during proton-beam irradiation for range estimation",* Med. Phys. **42** (11) (2015).

[75] M. Komori, E. Sekihara, T. Yabe, R. Horita, T. Toshito, and S. Yamamoto, *"Luminescence imaging of water during uniform-field irradiation by spot scanning proton beams",* Phys. in Med. & Bio. **63** (2018).

[76] T. Yabe, M. Komori, R. Horita, T. Toshito, and S. Yamamoto, *"Estimation of the optical errors on the luminescence imaging of water for proton beam",* Nucl. Inst. and Meth. in Phys. Res., A, 888 (2018).

[77] T, Yabe, M. Sasano, Y. Hirano, T. Toshito, T. Akagi, T. Yamashita, M. Hayashi, T. Azuma, Y. Sakamoto, M. Komori, and S. Yamamoto, *"Addition of luminescence process in Monte Carlo simulation to precisely estimate the light emitted from water during proton and carbon-ion irradiation",* Phys. in Med. and Bio. **63** (2018).

[78] S. Yamamoto, M. Komori, T. Akagi, T. Yamashita, S. Koyama, Y. Morishita, E. Sekihara, and T. Toshito, *"Luminescence imaging of water during carbon-ion irradiation for range estimation",* Med. Phys. **43** (5), (2016).

[79] S. Yamamoto, T. Akagi, T. Yamashita, J. Toivonen, M. Yamaguchi, M. Komori, and N. Kawachi, *"Source of luminescence of water lower energy than the Cerenkov-light threshold during irradiation of carbon-ion",* Journ. of Phys. Commun. **2** (2018).

[80] S. Yamamoto, M. Komori, S. Koyama, and T. Toshito, *"Luminescence imaging of water during alpha particle irradiation",* Nucl. Inst. and Meth. in Phys. Res., A, 819 (2016).

[81] S. Yamamoto, *"Luminescence Imaging of Water During Irradiation of Beta Particles with Energy Lower than Cerenkov-Light threshold",* Trans. on Rad. and Plas. Med. Sci., Vol. 1, No. 4 (2017).

[82] T. Yabe, M. Komori, T. Toshito, M. Yamaguchi, N. Kawachi, and S. Yamamoto, *"Estimation and correction of produced light from prompt gamma photons on luminescence imaging of water for proton therapy dosimetry",* Phys. in Med. and Bio. **63** (2018).

[83] S. Yamamoto, S. Koyama, M. Komori, and T. Toshito, *"Luminescence imaging of water during irradiation of X-ray photons lower energy than Cerenkov-light threshold",* Nucl. Inst. and Meth. in Phys. Res., A, 832 (2016).

[84] S. Yamamoto, S. Koyama, T. Yabe, M. Komori, J. Tada, S. Ito, T. Toshito, T. Hirata, and K. Watanabe, *"Stability and linearity of luminescence imaging of water during irradiation of proton-beams and x-ray photons lower energy than the Cerenkov threshold",* Nucl. Inst. and Meth. in Phys. Res., A, 883 (2018).

[85] S. Yamamoto, S. Koyoma, M. Komori, and T. Toshito, *"Luminescence imaging of water during irradiation of X-ray photons lower than Cerenkov-light threshold",* Nucl. Inst. and Meth. in Phys. Res., A, 832 (2016).

[86] S. Yamamoto, T. Toshito, T. Akagi, T. Yamashita, M. Komori, *"Scintillation imaging of air during proton and carbon-ion beam irradiations",* Nucl. Inst. and Meth. in Phys. Res., A, 833 (2016).

[87] B. Fahimian, A. Ceballos, S. Turkan, DS Kapp, and G. Pratx, *"Seeing the invisible: direct visualization of therapeutic radiation beams using air scintillation",* Med. Phys. **41** (1), 010702 (2014).

[88] S. Yamamoto, *"Discovery of luminescence of water during radiation irradiation and application for medical physics",* Proc. of SPIE, Vol. 10049 (2017).

[89] M.D. Tarasov, S.L. El'yash, V.F. Goncharova, O.N. Petrushin, Y.A. Savel'ev, M.Y. Tarakanov, and Y.S. Shigaev, *"Efficiency of radioluminescence of water under the action of accelerated electrons",* Inst. and Exp. Techn. **50** (6), 761-763 (2007).

[90] G. Wang, *"A perspective on deep imaging",* IEEE Access Vol. 4, (2016).

[91] G. Wang, J.C. Ye, K. Mueller, and J.A. Fessler, *"Image reconstruction is a new frontier of machine learning",* IEEE Trans. on Med. Imag., **27** (6) (2018).

[92] H. Yi, X. Qu, Y. Sun, J. Peng, Y. Hou, and X. He, *"A permissible region extraction based on knowledge priori for x-ray luminescence computed tomography",* Multim. Syst. **25**, 147-154 (2019).

[93] A.A. Joshi, A.J. Chaudhari, C. Li, J. Dutta, S.R. Cherry, D.W. Shattuck, A.W. Toga, and R.M. Leahy, *"Digiwarp: a method for deformable mouse atlas warping to surface topographic data",* Phys. Med. Biol. **55** (20), (2010).

[94] W. Zhang, I.O. Romero, and C. Li, *"Time domain x-ray luminescence computed tomography: numerical simulations",* Biomed. Opt. Expr. **10** (1) (2019).